Dissertation

submitted to the
Combined Faculty of Mathematics, Engineering and Natural Sciences
of Heidelberg University, Germany
for the degree of
Doctor of Natural Sciences

Put forward by
Nikolas Daniel Liebster
born in Boston, USA

Oral examination on the 9th of July 2025

Pattern Formation and Supersolid Sound Modes in a Driven Superfluid

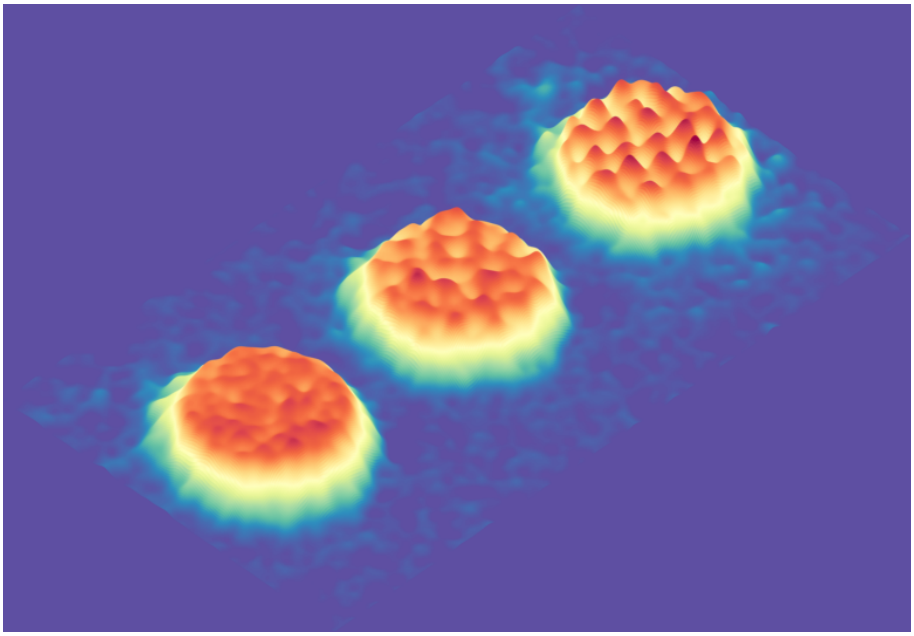

Referees: Prof. Dr. Markus K. Oberthaler
Prof. Dr. Lauriane Chomaz

Abstract

Systems driven far from equilibrium can show radically different properties from the same system at equilibrium. In some cases, new steady-states can emerge, enabling the application of theoretical frameworks typically developed in equilibrium. In this thesis, we discuss the emergence of self-stabilized, square lattice patterns in a Bose-Einstein condensate (BEC) with periodically modulated interactions. We show that despite the dynamical nature of the system, the patterned state displays Goldstone modes that are identical to those of supersolids, which are equilibrium superfluids with spontaneously arising periodic ordering.

We first provide a brief overview of the theoretical concepts underpinning the spontaneous emergence of the pattern, as well as its stabilization. We then present the experimental techniques used to observe the pattern, focusing mainly on tunable interactions and local control over the cloud using a digital micromirror device. Experimental results on the emergence of the structure are discussed, demonstrating that the pattern is truly a result of nonlinear phenomena far from equilibrium. We then turn towards explicit imprinting of lattices, which enables us to probe the phonon-phonon interactions that explain pattern stabilization. Beyond imprinting ideal lattices, we also explicitly instigate lattice and superfluid defects, observing their propagation. We identify two distinct speeds of sound for longitudinal excitations and a diffusive mode for transverse lattice deformations. We compare the extracted mode structure to a generic framework of superfluid smectics, extracting relevant hydrodynamic parameters of the system. Finally, we compare the dynamics of wavepackets to collective modes, finding good agreement.

Zusammenfassung

Systeme, die weit vom Gleichgewicht entfernt sind, können drastisch andere Eigenschaften aufweisen, als das gleiche System im Gleichgewicht. In einigen Fällen können neue stationäre Zustände entstehen, welche die Anwendung von theoretischen Modellen ermöglichen, die für Gleichgewichtssituationen entwickelt wurden. In dieser Arbeit beschreiben wir die Entstehung von selbststabilisierten, quadratischen Gittermustern in einem Bose-Einstein-Kondensat (BEC) mit periodisch modulierter Wechselwirkung. Wir zeigen, dass trotz der dynamischen Natur des Systems der gemusterte Zustand Goldstone-Moden aufweist, die mit denen von Supersoliden, d.h. Superfluiden mit spontan auftretender periodischer Ordnung im Gleichgewicht, identisch sind.

Wir geben zunächst einen kurzen Überblick über die theoretischen Konzepte, die der spontanen Entstehung des Musters und seiner Stabilisierung zugrunde liegen. Anschließend stellen wir die experimentellen Techniken vor, die zur Beobachtung des Musters verwendet werden, wobei wir uns hauptsächlich auf einstellbare Wechselwirkungen und die lokale Kontrolle über die Wolke mithilfe eines Mikrospiegelarray konzentrieren. Es werden experimentelle Ergebnisse über die Entstehung der Struktur diskutiert, die zeigen, dass das Muster tatsächlich das Ergebnis nichtlinearer Phänomene ist, die weit vom Gleichgewicht einsetzen. Anschließend wenden wir uns der expliziten Aufprägung von Gittern zu, die es uns ermöglicht, die Phonon-Phonon-Wechselwirkungen zu untersuchen, welche die Stabilisierung des Musters erklären. Wir prägen nicht nur ideale Gitter auf, sondern regen auch explizit Gitter- und Superfluiddefekte an und beobachten deren Ausbreitung. Wir identifizieren zwei unterschiedliche Schallgeschwindigkeiten für longitudinale Anregungen und eine diffusive Mode für transversale Gitterdeformationen. Wir vergleichen die extrahierte Modenstruktur mit einem generischen Modell von superfluiden smektischen Flüssigkristallen und extrahieren die relevanten hydrodynamischen Parameter des Systems. Schließlich vergleichen wir die Dynamik von Wellenpaketen mit kollektiven Moden und finden eine gute Übereinstimmung.

Contents

CHAPTER 1

Introduction

One of the most striking phenomena in science is the emergence of highly structured systems from simple natural laws. Rather than existing in a homogeneous, isotropic, and thermalized cloud of matter, we live in a universe filled with highly complex, patterned systems, ranging from the spiral shapes of galaxies to the stripes on a zebra to macroscopic, tessellated rock formations. Counter-intuitively, these structures exist because the universe is an out-of-equilibrium system, where dynamic physical systems can result in the emergence order rather than chaos.

The arrangement of nature into neat patterns is not only fascinating, it is also useful: complex, nonlinear dynamics can be described through remarkably simplified models that summarize the dynamics of many constituent particles into macroscopic structures. One of the first scientists to mathematically describe pattern formation was Alan Turing, who considered competing rates of reaction and diffusion between two substances, showing that domains of the two substances with specific length scales could emerge [1]. Since then, mathematical techniques for describing patterns have become increasingly sophisticated [2, 3] and have been discussed in a wide variety of disciplines, including nonlinear optics [4], biology [5], and chemistry [6].

In ultracold gases, the emergence of patterns has been a topic of interest ever since Bose-Einstein condensates (BECs) were realized in the lab. The first observation of structure formation in a BEC was a hexagonal vortex lattice, which emerged after rotating the system with external optical traps [7, 8]. Parallel experiments showed that one-dimensional condensates with attractive interactions result in periodically spaced bright solitons [9].

Several years later, it was demonstrated that periodically modulating the trapping potential of an effectively one-dimensional BEC results in the growth of density patterns known as Faraday waves [10], analogous to the formation of surface waves in shaken classical fluids [11–14]. Later experiments demonstrated the growth of Faraday patterns when modulating the interatomic interaction strength with a Feshbach

resonance [15]. The stability of these Faraday patterns as well as their sub-harmonic response was also demonstrated in one-dimensional systems [16, 17]. In two dimensions, driving the interaction strength with multiple frequencies was shown to selectively enhance scattering processes of specific geometries, resulting in patterns with square and hexagonal symmetry [18]. Further works have demonstrated structure formation due to modulational instability [9, 19, 20], Faraday patterns in strongly interacting superfluids [21], and the growth of incommensurate density patterns in a driven lattice [22].

In recent years, condensates made of dipolar atoms have become a dominant platform for studying the formation of patterned superfluids. These dipolar atoms, typically erbium and dysprosium, have large magnetic dipole moments, which leads to dipole-dipole interactions on the order of contact interactions [23]. In contrast to isotropic contact interactions, dipole interactions are anisotropic, and this additional structure (together with external traps and quantum fluctuations) can lead to spontaneously arising stationary states with periodically modulated densities.

A key feature of these patterned states is that they fulfill the definition of a supersolid, which is a quantum state of matter in which crystalline order and superfluidity exist simultaneously. Formally, such states are classified by the presence of two spontaneously broken symmetries–U(1) symmetry (corresponding to superfluidity), as well as translational symmetry (corresponding to crystalline ordering). The coexistence of solidity and superfluidity was first considered theoretically more than half a century ago [24], typically in the context of superfluid defects propagating through solid helium [25–27]. Definitive experimental observation of supersolids was only achieved recently [28–32], in systems that are superfluid but show the emergence of periodic patterns. Since then, a wealth of experimental and theoretical work has surrounded the characteristic features of supersolid systems, including [33–46].

In this thesis, we seek to unite the study of pattern formation in driven superfluids with that of supersolids. We first show the emergence of self-stabilized Faraday patterns in a two-dimensional superfluid with driven interactions. This state is stabilized through non-linear processes that had previously neither been discussed theoretically, nor observed experimentally. Secondly, while it has long been known that driven superfluids can show spontaneously arising density structures, neither the presence of Goldstone modes in the lattice nor the modification of the superfluid behavior has been studied. Using precise local control of the superfluid, we demonstrate that the patterned steady states indeed support novel sound modes not present in equilibrium by identifying distinct longitudinal sound excitations in the lattice and superfluid, as well as a diffusive transverse lattice mode. These modes are probed with both long wavelength collective excitations and localized wavepackets. Finally, we apply a hydrodynamic theory of superfluid smectics to extract compressibilities of the lattice and superfluid.

This thesis is organized as follows. The second chapter provides a brief overview of spontaneous symmetry breaking, while the third chapter discusses Bogoliubov quasiparticles, detailing not only the form of the dispersion relation but also some key properties of coherent states of Bogoliubov phonons.

The fourth chapter focuses on theoretical models describing driven superfluids, discussing both Floquet analyses that describe instabilities due to driving, as well as non-linear methods that capture pattern stabilization. A key result is the derivation of the amplitude equation, which describes angle-dependent processes that lead to the stabilization of square lattice patterns, observed experimentally in the course of this thesis [47].

The fifth chapter provides an overview of the experimental system, with an emphasis on the techniques relevant for this work, in particular the measurement of momentum distributions and the development of a novel trapping geometry, the slox potential.

The sixth chapter presents experimental results on the spontaneous emergence of square lattice patterns in the experiment. We quantify the emergence of square lattices, which arise in a large range of experimental parameters. We also compare the stability of patterns in different trapping geometries, finding that boundary conditions play a critical role in the observed dynamics.

The seventh chapter details our efforts to "synthetically" produce patterns, with the use of spatially modulated light fields. We explicitly demonstrate the role of angle-dependent effects between individual density waves, and also provide an overview of how pattern stability can be optimized.

Chapter eight provides experimental results on the supersolid sound modes, showing the dynamics of long-wavelength perturbations to the lattice and superfluid phases. We first investigate stripe patterns, finding that the presence of the stripe reduces the longitudinal superfluid response while leaving the transverse superfluid mode unaffected. We use a hydrodynamic model of superfluid smectics [48, 49] to extract relevant parameters of the system. We then probe transverse lattice excitations, showing that they are critically damped. The extracted dispersion relations are then compared to the dynamics of localized wavepackets, showing good agreement between two independent perturbing schemes.

CHAPTER 2

Spontaneous Symmetry Breaking

Spontaneous symmetry breaking (SSB) is a fundamental concept in physics, playing a defining role in physical phenomena such as superconductivity, the electroweak interaction, phase transitions, and pattern formation. In this section, we will briefly provide a formal definition of SSB and discuss a few of its physical consequences. We then point out the formal similarities between Ginzburg-Landau theory for describing phase transitions and pattern formation. This section largely follows the logic and structure of [52], as well as [53].

2.1 Broken Symmetries

The notion of SSB is based on a simple yet somewhat surprising fact: the symmetries of a Hamiltonian are not necessarily the same as those of its eigenstates. In order to piece apart the implications of this statement, we will first define what a symmetry is, and then explore some of the consequences of symmetry breaking.

2.1.1 Definition

States are defined to be symmetric under a unitary transformation U if they are unaltered by the transformation up to a phase factor,

$$U\left|\psi\right\rangle = e^{i\varphi}\left|\psi\right\rangle . \tag{2.1}$$

For example, such a transformation can represent the rotation of a sphere, a translation in space, or a shift in the phase of a wavefunction. Symmetries of a Hamiltonian, on the other hand, are defined in terms of invariance under a unitary operator, such that $[U, H] = 0$, or equivalently $U^{\dagger}HU = H$.

If a Hamiltonian H is invariant under such a symmetry transformation U but an eigenstate $|\psi\rangle$ is not, the state has spontaneously broken the symmetry of the Hamiltonian. This essentially means that the natural laws describing the dynamics of a system do not depend on the phase φ, and that therefore there are many degenerate eigenstates each with a different phase. The degeneracy is clearly shown in that while $|\psi\rangle$ and $U|\psi\rangle$ are different states, U commutes with the underlying Hamiltonian and these states must therefore have the same energy.

The transformation U is a global transformation, meaning that it is applied uniformly over the whole system, and thus the symmetries described by the transformation are also called global symmetries. This is in contrast to local transformations, such as a gauge transformation, which depend on space. Local symmetries cannot be spontaneously broken in the same way as global symmetries, in that the emerging Goldstone modes are not gauge invariant [54]. This is a crucial point in distinguishing U(1) symmetry from gauge symmetry, and the often repeated phrase "U(1) gauge symmetry breaking" is therefore misleading.

While these definitions are somewhat abstract, it turns out that considering the consequences of SSB results in remarkable predictive power in determining characteristics of a given physical system. In the following, we will focus on two such consequences, namely the Noether and Goldstone theorems.

2.1.2 Noether Theorem

As was defined earlier, a transformation U defines a symmetry of the Hamiltonian if it commutes with H. If U is a unitary transformation, it can be written as the exponential of an operator Q, i.e. $U = e^{iQ}$. Additionally, we know that for time-independent Hamiltonians, the time evolution of a state can be described through exponentiation of the Hamiltonian, where

$$|\psi(t)\rangle = e^{-iHt/\hbar}|\psi\rangle . \tag{2.2}$$

Because U is a symmetry of H, it commutes with the time evolution operator, which further implies that $[Q, e^{iHt}] = 0$, and that therefore the expectation value of Q is conserved in time:

$$\langle\psi(t)|Q|\psi(t)\rangle = \langle\psi|e^{iHt/\hbar}Qe^{-iHt/\hbar}|\psi\rangle = \langle\psi|Q|\psi\rangle . \tag{2.3}$$

This leads to the general statement that any unitary, continuous symmetry corresponds to an observable Q, where $U = e^{iQ}$ and Q is a conserved quantity.

Noether's theorem is based on the notion that globally conserved quantities can be expressed as integrals over a local density of the conserved quantity Q,

$$Q = \int d\mathbf{x}\rho(\mathbf{x}, t). \tag{2.4}$$

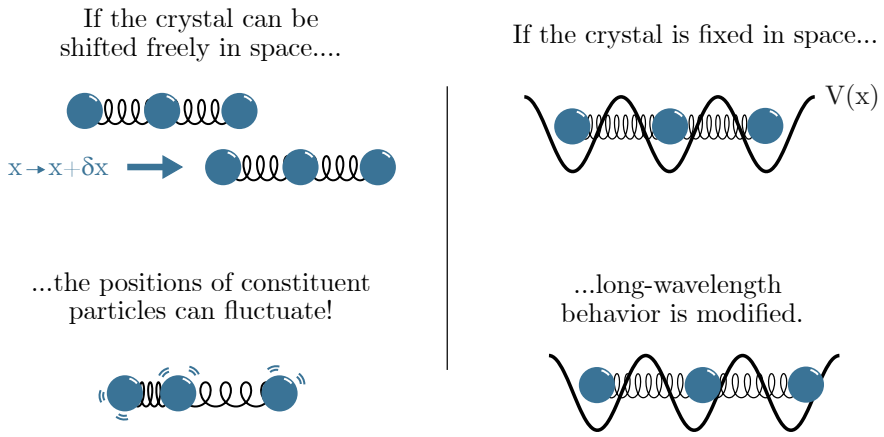

Figure 2.1: Visualization of Goldstone Theorem. Left, a toy model for spontaneous translational symmetry breaking into crystalline ordering, using balls on a spring. The spontaneous emergence of the crystal means that the global position of the lattice can be shifted freely, which in turn means that constituent atoms can fluctuate freely. Right, the contrasting case of explicit symmetry breaking. The periodic potential fixes the position of the crystal. Small perturbations come at an energy cost, as seen by the incommensurate spacing of balls and potential minima.

Because Q is stationary in time, a locally elevated density in one position x means that at some other point x', the density must be diminished. This leads to the continuity equation

$$\frac{\partial}{\partial t}\rho(\mathbf{x},t) + \boldsymbol{\nabla}\cdot\mathbf{j}(\mathbf{x},t) = 0, \tag{2.5}$$

where $\mathbf{j}(\mathbf{x},t)$ is the current associated with the density. The correspondence between a symmetry and a continuity equation constitutes Noether's theorem. For this work, three relevant examples are

- U(1) symmetry → conservation of particle number in a condensate
- Space translational symmetry → conservation of total momentum
- Time translational symmetry → conservation of total energy.

While U(1) and space translation symmetry are spontaneously broken in the driven superfluid, time translation symmetry is explicitly broken by the drive, leading to a lack of energy conservation.

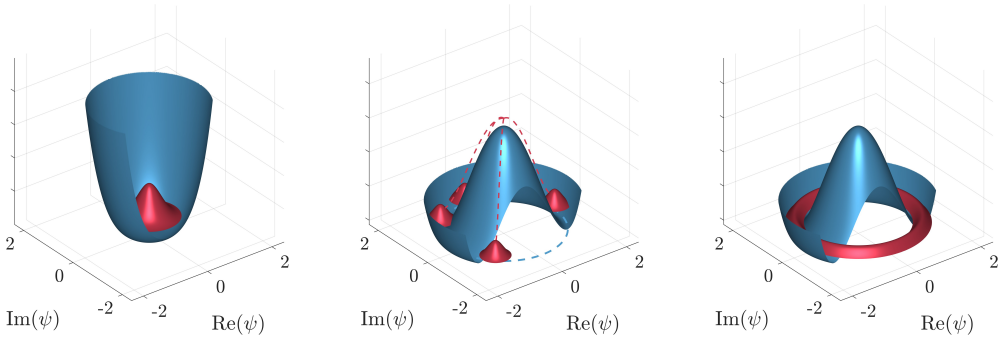

Figure 2.2: Champagne Bottle Potential. Left, an effective potential for $a < 0$ (blue) and its groundstate (red). The expectation value of the order parameter in this case is 0. Center, the effective potential after the control parameter has been quenched $a > 0$, where single realizations now have finite $|\langle\psi\rangle|$ and a random phase. Right, the average distribution with $a > 0$, showing that each phase is equally possible.

2.1.3 Goldstone Theorem

The most famous consequence of SSB is the emergence of Goldstone modes. The general idea is relatively straightforward; because a symmetry is broken spontaneously, nothing sets a given phase, and global changes to a phase should come at no energy cost. A concrete example is the spontaneous formation of crystalline order, where the phase of the order parameter is simply the spatial phase of the lattice. If the underlying Hamiltonian is still translationally invariant, then it should come at no energy cost to simply shift the crystal in space.

These global transformations can alternatively be viewed as a deformation of the phase with infinite wavelength, i.e. $k \to 0$. Deformations at a length scale that is very large but finite, however, begin to cost energy. In a crystal, this is like a slow variation of the position of constituent particles, which will compress and stretch the lattice. In the limit where this wavenumber of the variation is infinitesimally small, this should come at a vanishing energy cost. This indicates the presence of a "gapless" mode in the dispersion relation, where the word gapless simply implies that the energy cost goes to zero when the wavenumber goes to zero, i.e. $\omega(k \to 0) = 0$. Therefore, SSB indicates the emergence of a new effective (quasi-)particle with zero mass.

Though this generic case is often stated simply, the specifics of a given physical system can add complexity. For example, spontaneous breaking of translational symmetry can also simultaneously break rotational symmetry, and therefore no additional particle emerges despite two symmetries being broken [55, 56]. Another case of particular relevance for this work is the emergence of vortex lattices in rotating superfluids [7]. Though the vortex lattice spontaneously breaks translational symmetry,

the dynamics of the vortices are rigidly coupled to the superfluid phase (linked to the spontaneously breaking of the U(1) symmetry), and therefore no additional Goldstone modes emerge [49]. The counting of Goldstone modes and broken symmetries is an ongoing field of theoretical study, and it was only recently described why crystals have a reduced number of Goldstone bosons compared to the number of broken symmetries [56]. Finally, while one can assume that the dispersion relation will be linear for low momenta ($\omega \sim |c|k$) in relativistic theories, in non-relativistic theories this is not generically the case, and the dispersion can also be quadratic.

2.2 Ginzburg-Landau Equation

So far, we have discussed the consequences of symmetries and states that break them, but we have not discussed how such states can arise. A generic mechanism for describing SSB is known as Landau theory, which has relevance for describing both phase transitions and pattern formation. This section roughly follows the logic presented in [53].

2.2.1 Phase Transitions

We will first consider the case of phase transitions. To write a minimal description of phase transitions, one assumes that a spatially uniform, complex-valued order parameter ψ is analytic, and that at the critical point of the phase transition the expectation value $\langle\psi\rangle$ is small. Examples of such an order parameter are the magnetization m of a ferromagnet, or the order parameter of a superfluid. Under the assumption that the Hamiltonian describing the dynamics is symmetric under a phase rotation of the order parameter, $\psi \to e^{i\theta}\psi$, the free energy density can be written as

$$f = a|\psi|^2 + b|\psi|^4 + \text{h.o.t.} \tag{2.6}$$

where a and b are temperature-dependent quantities. In equilibrium, the free energy density is minimized with respect to the order parameter, resulting in

$$0 = a\psi + 2b|\psi|^2\psi. \tag{2.7}$$

If the temperature dependence of a has the form $a = a_0(T - T_c)/T_c$, where T_c is the critical temperature of a phase transition and $a_0 > 0$, it becomes apparent that the magnitude of the order parameter $|\bar{\psi}|$ can have the solutions:

$$|\bar{\psi}| = \begin{cases} 0 & T > T_c \\ \sqrt{\frac{a}{2b}} & T < T_c. \end{cases} \tag{2.8}$$

Therefore, when crossing the critical temperature, the order parameter ψ suddenly has a non-zero expectation value. Because the underlying Hamiltonian is independent of the phase or the order parameter, this is chosen spontaneously, indicating spontaneous symmetry breaking.

This process can be visualized graphically by the heuristic champagne-bottle bottom potential. Sketched in Fig. 2.2, it shows the effective energy landscape that describes the expectation value of the order parameter ψ. For high temperatures, the potential has a trivial shape, resulting in an expectation value of zero. Below the critical temperature, however, there are an infinite number of minima, each corresponding to a certain phase of the order parameter. As the phase transition occurs, the state "runs" down the hill at the center, spontaneously selecting a specific phase in each realization.

2.2.2 Pattern Formation

A different setting in which Ginzburg-Landau theory is applied is the field of pattern formation. Here, generic mathematical models are constructed to describe the formation of structure, without making specific assumptions of the microscopic processes. These generic frameworks are typically constructed by considering a system with an instability at a critical wavenumber k_c, and deriving the dynamics of the amplitudes of modulations of these waves.

A minimal model to describe pattern formation is a one-dimensional system defined by a differential equation

$$\partial_t u(x,t) = f(r, u, \nabla u, ...) \tag{2.9}$$

where $r = (r_0 - r_c)/r_c$ is a control parameter that leads to an instability at a non-zero wavenumber ($k_c \neq 0$) if a critical value r_c is reached. We assume that the function $u(x,t)$ has a uniform solution $\bar{u}$, and that near the threshold ($r \ll 1$) a perturbation $\delta u(x,t) = u(x,t) - \bar{u}$ has a growing solution of the form

$$\delta u(x,t) = A(x,t)e^{ik_c x} + A^*(x,t)e^{-ik_c x}. \tag{2.10}$$

We now make a number of further assumptions: (i) the system is translationally invariant, i.e. $A \to Ae^{i\Delta}$ is simply a translation in space, which does not change the dynamics. (ii) The system obeys parity symmetry, i.e. $A \to A^*$, $x \to -x$, which corresponds to an inversion of the coordinates of the model Eq. (2.9).

We can now construct an amplitude equation that describes the dynamics of only the slowly-varying amplitude A, using the above assumptions to limit the number of terms that can appear in such a description. This is known as the real Ginzburg-Landau equation, as it bears a resemblance to Eq. (2.7):

$$\tau_0 \frac{\partial A}{\partial t} = l_0^2 \frac{\partial^2 A}{\partial x^2} + rA - \lambda |A|^2 A. \tag{2.11}$$

Here, τ_0 and l_0 are length and time scales that originate from the nature of the instability, and λ is a non-linear prefactor that depends on system characteristics. In analogy to the description of phase transitions, we now look for stationary solutions (i.e. $\partial_t A = 0$), and assume that the amplitude of the pattern is uniform and infinitely extended ($\partial_x^2 A = 0$). For the case $r, \lambda > 0$, there are an infinite number of steady state solutions, because only the magnitude of the wave is determined

$$|A| = \sqrt{\frac{r}{\lambda}}. \tag{2.12}$$

The real Ginzburg-Landau equation only describes stationary states, and does not describe oscillatory solutions. If we use an *ansatz* that oscillates in time, i.e. $\delta u(x,t) = A(x,t)e^{ik_c x + i\omega t}$ + c.c., we break time translation symmetry, and the description is slightly more involved. While the intuition gained from the stationary situation is still useful, the comparison between pattern formation and dynamics in an effective potential is not direct.

2.2.3 Interpretation

It should be noted that at first glance, the similarities between phase transitions and pattern formation are mostly formal ones: phase transitions consider states that minimize an energy functional, while pattern formation formalism is used to describe out-of-equilibrium, highly non-linear steady states, often in cases with an external drive (i.e. no energy conservation is guaranteed). Because both models are constructed based on fundamental assumptions about symmetries without considering details of a specific system, it is also not so surprising that the dramatically simplified form of the equations describing these two situations have certain similarities.

However, a key feature of pattern formation is the spontaneous breaking of translational symmetry, as evidenced by Eq. (2.11), which does not depend on the spatial phase of the emergent standing wave. Thus, one can expect that patterns host Goldstone modes, and indeed these fluctuations are often discussed in terms of pattern disintegration [53, 57]. While one cannot necessarily make generic statements about excitations as one can in equilibrium, it is possible that certain out-of-equilibrium states demonstrate sufficient conserved quantities to apply hydrodynamic models that describe the linear response of such a system.

Chapter 3

Bogoliubov Theory

In this thesis, we will study the dynamics of patterns in an interacting superfluid. To do so, it is useful to consider the fundamental excitations of such a superfluid, which are described by Bogoliubov theory. Here, we give a brief overview of the derivation of the dispersion relation, and then investigate the characteristics of Bogoliubov quasiparticles in thermal and coherent states. This section is based on [58–60].

3.1 Static Hamiltonian in Second Quantization

The Hamiltonian of a non-relativistic gas of Bosons in position space is given by:

$$H = -\int d^3x \frac{\hbar^2}{2m}\psi^\dagger(\mathbf{x})\nabla^2\psi(\mathbf{x}) + \frac{g}{2}\int d^3x\, \psi^\dagger(\mathbf{x})\psi^\dagger(\mathbf{x})\psi(\mathbf{x})\psi(\mathbf{x}), \tag{3.1}$$

where m is the particle mass, $\hbar$ is the reduced Planck's constant, g is the two-particle contact interaction, and ψ ($\psi^\dagger$) is the bosonic field annihilation (creation) operator for atoms, which annihilates (creates) a particle at a point in space. Here we assume a uniform Bose gas in a box with side length L. A transformation to momentum space results in the form

$$\psi(\mathbf{x}) = \frac{1}{\sqrt{L^3}}\sum_{\mathbf{k}} a_{\mathbf{k}} e^{i\mathbf{k}\cdot\mathbf{x}}. \tag{3.2}$$

Inserting this into Eq. (3.1), one finds

$$H = \frac{\hbar^2 k^2}{2m} a^\dagger_{\mathbf{k}} a_{\mathbf{k}} + \frac{g}{2L^3}\sum_{\mathbf{k},\mathbf{p},\mathbf{q}} a^\dagger_{\mathbf{k}-\mathbf{q}} a^\dagger_{\mathbf{p}+\mathbf{q}} a_{\mathbf{p}} a_{\mathbf{k}}. \tag{3.3}$$

In a superfluid, the temperature is low enough that the $\mathbf{k} = 0$ state contains a macroscopically large number of particles, N_0, and we therefore approximate that operators

can be replaced with their expectation values,

$$a_{\mathbf{k}=0} \to \sqrt{N_0}, \;\; a^\dagger_{\mathbf{k}=0} \to \sqrt{N_0}. \tag{3.4}$$

Using this approximation, the interaction term in Eq. (3.3) can be simplified by replacing all $a^{(\dagger)}_{\mathbf{k}=0}$ operators with N_0 and truncating the sum above terms of order $a^2_{\mathbf{k}}$, leaving us with:

$$\begin{aligned}
\mathbf{k}=0,\, \mathbf{p}=0 \quad &\to N_0 a^\dagger_{-\mathbf{q}} a^\dagger_{\mathbf{q}} \\
\mathbf{k}=0,\, \mathbf{p}+\mathbf{q}=0 \quad &\to N_0 a^\dagger_{\mathbf{p}} a_{\mathbf{p}} \\
\mathbf{k}=0,\, \mathbf{k}-\mathbf{q}=0 \quad &\to N_0 a^\dagger_{\mathbf{p}} a_{\mathbf{p}} \\
\mathbf{p}=0,\, \mathbf{p}+\mathbf{q}=0 \quad &\to N_0 a^\dagger_{\mathbf{k}} a_{\mathbf{k}} \\
\mathbf{p}=0,\, \mathbf{k}-\mathbf{q}=0 \quad &\to N_0 a^\dagger_{\mathbf{q}} a_{\mathbf{q}} \\
\mathbf{p}+\mathbf{q}=0,\, \mathbf{k}-\mathbf{q}=0 \quad &\to N_0 a_{-\mathbf{q}} a_{\mathbf{q}} \quad .
\end{aligned} \tag{3.5}$$

With the additional term in which all momenta are 0, the Hamiltonian can be written as

$$H \simeq \frac{N_0 n_0 g}{2} + [\epsilon + 2n_0 g] \sum_{\mathbf{k}\neq 0} a^\dagger_{\mathbf{k}} a_{\mathbf{k}} + \frac{n_0 g}{2} \sum_{\mathbf{k}\neq 0} [a^\dagger_{\mathbf{k}} a^\dagger_{-\mathbf{k}} + a_{\mathbf{k}} a_{-\mathbf{k}}] \tag{3.6}$$

where n_0 is the density and $\epsilon = \frac{\hbar^2 k^2}{2m}$ is the kinetic energy.[1] As condensate atoms can typically not be distinguished from excited state atoms, it is useful to define the total atom number as

$$N = N_0 + \sum_{\mathbf{k}\neq 0} a^\dagger_{\mathbf{k}} a_{\mathbf{k}}. \tag{3.7}$$

Writing this in terms of N_0 and inserting it into Eq. (3.6), one can then neglect higher-order terms as well as remaining constant terms to find:

$$H \simeq [\epsilon + \mu] \sum_{\mathbf{k}\neq 0} a^\dagger_{\mathbf{k}} a_{\mathbf{k}} + \frac{\mu}{2} \sum_{\mathbf{k}\neq 0} [a^\dagger_{\mathbf{k}} a^\dagger_{-\mathbf{k}} + a_{\mathbf{k}} a_{-\mathbf{k}}], \tag{3.8}$$

where $\mu = ng$ is the chemical potential.

[1] Interestingly, the approximation of converting the operators for condensate momentum modes to real numbers has explicitly set the phase of the condensate, and the approximate Hamiltonian is no longer U(1) invariant. As is evident in the last two terms of Eq. (3.6), one can no longer transform creation operators with a free phase $a_{\mathbf{k}} \to e^{i\varphi} a_{\mathbf{k}}$). This corresponds to a lack of atom number conservation [60].

3.2 Bogoliubov Transformation

The Hamiltonian Eq. (3.8) is not diagonal, meaning that real particles are no longer a convenient basis for describing excitations of the superfluid. With a Bogoliubov transformation, we can define new operators that correspond to the eigenstates of the approximate Hamiltonian. These operators are defined as

$$\begin{pmatrix} a_{\mathbf{k}} \\ a^{\dagger}_{-\mathbf{k}} \end{pmatrix} = \begin{pmatrix} u_{\mathbf{k}} & v_{-\mathbf{k}} \\ v_{-\mathbf{k}} & u_{\mathbf{k}} \end{pmatrix} \begin{pmatrix} b_{\mathbf{k}} \\ b^{\dagger}_{-\mathbf{k}} \end{pmatrix}, \tag{3.9}$$

with the normalization condition $u^2_{\mathbf{k}} - v^2_{-\mathbf{k}} = 1$. To demonstrate that these new creation and annihilation operators $b^{(\dagger)}_{\mathbf{k}}$ are a good choice, we can write the Hamiltonian Eq. (3.8) in matrix form

$$H \simeq \sum_{\mathbf{k}\neq 0} \begin{pmatrix} a^{\dagger}_{\mathbf{k}} & a_{-\mathbf{k}} \end{pmatrix} \begin{pmatrix} \epsilon + \mu & \frac{\mu}{2} \\ \frac{\mu}{2} & 0 \end{pmatrix} \begin{pmatrix} a_{\mathbf{k}} \\ a^{\dagger}_{-\mathbf{k}} \end{pmatrix}, \tag{3.10}$$

and insert the transformation Eq. (3.9). The factors $u_{\mathbf{k}}$ and $v_{-\mathbf{k}}$ are determined by setting the off-diagonal terms $b^{\dagger}_{\mathbf{k}} b^{\dagger}_{-\mathbf{k}}$ and $b_{\mathbf{k}} b_{-\mathbf{k}}$ to zero, resulting in the condition

$$(\epsilon + \mu) u_{\mathbf{k}} v_{-\mathbf{k}} + \frac{\mu}{2}(u^2_{\mathbf{k}} + v^2_{-\mathbf{k}}) = 0. \tag{3.11}$$

Solving for these coefficients, and one finds that the Hamiltonian is indeed diagonalized by this transformation,

$$H = E(k)\, b^{\dagger}_{\mathbf{k}} b_{\mathbf{k}}, \tag{3.12}$$

where E is the Bogoliubov dispersion relation given by

$$E(k) = \sqrt{\epsilon(\epsilon + 2\mu)}, \tag{3.13}$$

and the transformation coefficients are given by

$$u_{\mathbf{k}}, v_{-\mathbf{k}} = \pm \sqrt{\frac{\epsilon + \mu}{2E(k)} \pm \frac{1}{2}}. \tag{3.14}$$

Here, a notable consequence of the Bogoliubov transformation becomes apparent: we have transformed from the frame of a gas of interacting particles to a gas of non-interacting quasiparticles. These quasiparticles are comprised of many individual free particles in positive and negative momentum modes, as well as positive and negative frequency branches:

$$b^{\dagger}_{\mathbf{k}} = u_{\mathbf{k}} a^{\dagger}_{\mathbf{k}} - v_{-\mathbf{k}} a_{-\mathbf{k}}. \tag{3.15}$$

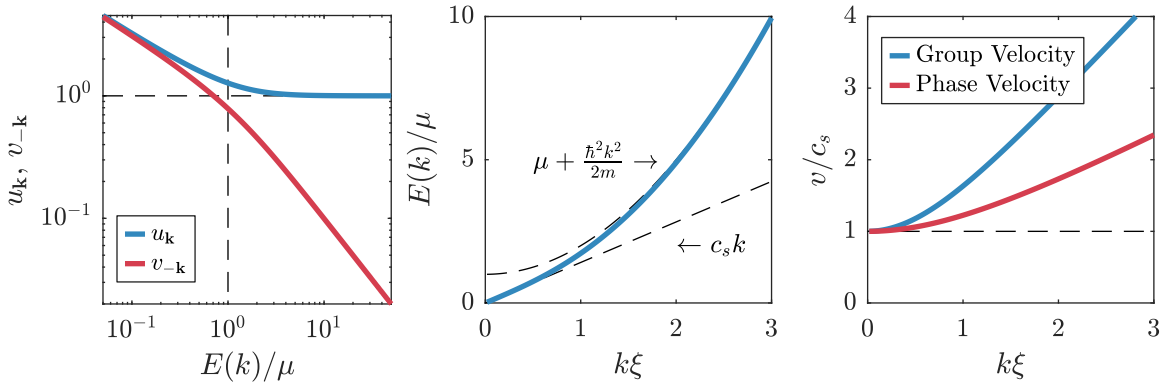

Figure 3.1: Characteristics of the Bogoliubov Dispersion Relation. Left, the prefactors $u_{\mathbf{k}}$ and $v_{-\mathbf{k}}$. Center, the dispersion relation, normalized to the chemical potential. Right, the group and phase velocities from the dispersion relation.

Considering the limiting cases of the prefactors $u_{\mathbf{k}}$ and $v_{-\mathbf{k}}$ (shown in the left panel of Fig. 3.1), one can see that in the low momentum limit $p \to 0$, the coefficients diverge and become roughly equal, indicating divergingly large occupations of constituent atoms. In the high momentum limit, $u_{\mathbf{k}} \to 1$ and $v_{-\mathbf{k}} \to 0$, indicating a more direct mapping between Bogoliubov quasiparticles and free particles.

3.3 Characteristics of the Dispersion Relation

The dispersion relation, given by Eq. (3.13), is roughly linear in the low momentum limit, indicating phononic behavior. The speed of sound of the gas is given by

$$c_s = \sqrt{\frac{\mu}{m}}. \tag{3.16}$$

As discussed in the previous section, the dispersion relation therefore results in gapless, phononic behavior in the limit of $k \to 0$, as predicted by the Goldstone theorem. The Bogoliubov phonons are therefore akin to the Goldstone bosons corresponding to the spontaneously broken U(1) symmetry.

In the high-momentum limit, the dispersion relation is quadratic, with an energy offset given by the chemical potential. A convenient length scale that describes the transition between these regimes is the healing length ξ, where the kinetic energy of

the quasiparticles is equal to the chemical potential, i.e.

$$\frac{\hbar^2}{2m}\left(\frac{1}{\xi}\right)^2 = \mu. \tag{3.17}$$

This length scale corresponds to the size of topological defects, as well as how the gas responds to external perturbations such as potentials or phase kinks.

Though it is often said that the Bogoliubov dispersion relation is linear for low momenta, this is only true as a limit. For realistic experimental parameters, it is therefore prudent to consider the group and phase velocity of the dispersion relation, as these are the rates with which the system will respond to dynamics. Performing a simple derivative, the group velocity is given by

$$v_g = \frac{\hbar k}{m}\frac{\epsilon + \mu}{E}. \tag{3.18}$$

These speeds are plotted relative to the speed of sound, c_s, in the right panel of Fig. 3.1. Even at the length scales well below the healing length, there are significant differences between the speed of sound and the group velocity, which must be considered in comparisons to theoretical models as well as in the extraction of experimental parameters.

3.4 Bogoliubov Quasiparticles

The Bogoliubov transformation is somewhat unintuitive at first glance, and it is therefore instructive to consider typical scenarios encountered in the experiment. In this section, we will show how occupations of Bogoliubov quasiparticles in thermal and coherent states manifest in experimentally observable quantities.

3.4.1 Thermal States

In the experiment, we measure real particles, making the accessible quantity the expectation value of $a^\dagger a$ rather than $b^\dagger b$. This can be calculated with the transformation as defined previously:

$$\begin{aligned} N_k = \langle a^\dagger_{\mathbf{k}} a_{\mathbf{k}}\rangle &= u^2_{\mathbf{k}}\langle b^\dagger_{\mathbf{k}} b_{\mathbf{k}}\rangle + v^2_{-\mathbf{k}}\langle b_{-\mathbf{k}} b^\dagger_{-\mathbf{k}}\rangle + u_{\mathbf{k}} v_{-\mathbf{k}}\left(\langle b^\dagger_{\mathbf{k}} b^\dagger_{-\mathbf{k}}\rangle + \langle b_{-\mathbf{k}} b_{\mathbf{k}}\rangle\right) \\ &= u^2_{\mathbf{k}}\langle b^\dagger_{\mathbf{k}} b_{\mathbf{k}}\rangle + v^2_{-\mathbf{k}}\left(1 + \langle b^\dagger_{-\mathbf{k}} b_{-\mathbf{k}}\rangle\right) + u_{\mathbf{k}} v_{-\mathbf{k}}\left(\langle b^\dagger_{\mathbf{k}} b^\dagger_{-\mathbf{k}}\rangle + \langle b_{-\mathbf{k}} b_{\mathbf{k}}\rangle\right), \end{aligned} \tag{3.19}$$

where the second line shows the commutation of $b^\dagger_{-\mathbf{k}}$ and $b_{-\mathbf{k}}$ in the second term.

In a thermal state, the effective description of the system as a gas of non-interacting quasiparticles indicates that the average occupation number of quasiparticles N_k must obey a Bose-Einstein distribution:

$$N_k = \langle b_{\mathbf{k}}^\dagger b_{\mathbf{k}} \rangle = \frac{1}{e^{\beta E(k)} - 1}, \tag{3.20}$$

where $\beta = 1/k_B T$, with k_B the Boltzmann constant and T the temperature. Because we have assumed a thermal state, the coherences are zero, $\langle b_{\mathbf{k}}^\dagger b_{-\mathbf{k}}^\dagger \rangle = \langle b_{-\mathbf{k}} b_{\mathbf{k}} \rangle = 0$, and we find that the occupation number of real particles is

$$N_{k,T} = v_{-\mathbf{k}}^2 + \frac{u_{\mathbf{k}}^2 + v_{-\mathbf{k}}^2}{e^{\beta E(k)} - 1}. \tag{3.21}$$

A key feature of the thermal state is that even at vanishingly low temperatures, there are still occupations of free particles, known as quantum depletion.

3.4.2 Coherent States

To gain some intuition about the dynamics of Bogoliubov phonons, we will consider coherent states, which can be defined as

$$|\alpha\rangle = e^{\sum_{\mathbf{k}} \phi_{\mathbf{k}} b_{\mathbf{k}}^\dagger} |\mathrm{BEC}\rangle \tag{3.22}$$

where $\phi_{\mathbf{k}}$ is a complex valued amplitude, the sum runs over all single particle momentum states, and $|\mathrm{BEC}\rangle$ is defined as the quasi-particle vacuum state, such that

$$b_{\mathbf{k}} |\mathrm{BEC}\rangle = 0, \quad \forall\, \mathbf{k} \neq 0, \quad a_0 |\mathrm{BEC}\rangle = \sqrt{N_0} |\mathrm{BEC}\rangle . \tag{3.23}$$

Now, we consider standing waves, in which modes with momenta $\mathbf{k}$ and $-\mathbf{k}$ are coherently occupied. The coherent state can be written as

$$|\alpha_k(t)\rangle = e^{\phi_{\mathbf{k}}(t) b_{\mathbf{k}}^\dagger + \phi_{-\mathbf{k}}(t) b_{-\mathbf{k}}^\dagger} |\mathrm{BEC}\rangle , \tag{3.24}$$

where the time-dependent amplitudes are described in the Schrödinger picture as rotating with their eigenfrequency $\omega_{\mathbf{k}}$ given by the dispersion relation, $\phi_{\mathbf{k}}(t) = \phi_{\mathbf{k}}(t = 0) e^{-i\omega_{\mathbf{k}} t}$. Again considering that the experimentally accessible quantity is the momentum distribution of single particles, we calculate the expectation value for such a standing wave

$$\langle N_k \rangle = \langle \alpha_k(t)| \, a_{\mathbf{k}}^\dagger a_{\mathbf{k}} \, |\alpha_k(t)\rangle . \tag{3.25}$$

If we consider only cases where occupations in the $\pm\mathbf{k}$ modes are symmetric and the system is at rest, i.e. $\phi_{\mathbf{k}}(t) = \phi_{-\mathbf{k}}(t)$, the average density of atoms is given by

$$\langle N_k \rangle = v_{-\mathbf{k}}^2 + \left[u_{\mathbf{k}}^2 + v_{-\mathbf{k}}^2 + 2u_{\mathbf{k}}v_{-\mathbf{k}}\cos\left(2\omega_{\mathbf{k}}t + 2\varphi\right)\right]|\phi|^2, \tag{3.26}$$

where $\phi = |\phi(t=0)|e^{i\varphi}$. The procedure is identical to Eq. (3.19), but here $\langle b_{\mathbf{k}}^\dagger b_{\mathbf{k}}\rangle = |\phi|^2$ and the coherent terms result in oscillatory behavior, and are calculated using the identity

$$\langle\alpha|\, b_{\mathbf{k}}^{(\dagger)}\,|\alpha\rangle = \phi_{\mathbf{k}}^{(*)} \tag{3.27}$$

up to a normalization factor. The form of Eq. (3.26) can be dramatically simplified, using the identity $\cos\theta = 1 - 2\sin^2\frac{\theta}{2}$, to find

$$\langle N_k \rangle = v_{-\mathbf{k}}^2 + (u_{\mathbf{k}}^2 + v_{-\mathbf{k}}^2 + 2u_{\mathbf{k}}v_{-\mathbf{k}})\left[1 - \frac{4u_{\mathbf{k}}v_{-\mathbf{k}}}{u_{\mathbf{k}}^2 + v_{-\mathbf{k}}^2 + 2u_{\mathbf{k}}v_{-\mathbf{k}}}\sin^2(\omega_{\mathbf{k}}t + \varphi)\right]|\phi|^2, \tag{3.28}$$

which can be shown to be equivalent to

$$\langle N_k \rangle = v_{-\mathbf{k}}^2 + \frac{\epsilon}{E}\left[1 - \frac{2\mu}{\epsilon}\sin^2(\omega_{\mathbf{k}}t + \varphi)\right]|\phi|^2. \tag{3.29}$$

This equation displays a remarkable feature of Bogoliubov quasi-particles. In the low momentum-limit, the occupations of real particles with momentum $\mathbf{k}$ oscillate in time, even if the occupations of the quasiparticles are static. This is due to the mixing of both positive and negative momentum *as well as* positive and negative frequency modes in the Bogoliubov transformation.

In the current *ansatz*, the phase factor φ is irrelevant and can be set to zero. However, if time-translation symmetry is explicitly broken (as is the case in the driven system), this phase not only provides insights, it plays a crucial role in the description of dynamics in systems far from equilibrium.

Chapter 4

Driven Systems

In this chapter, we will discuss theoretical dynamics described by the driven Gross-Pitaevskii equation (GPE). We will first discuss how instabilities at certain length scales emerge, showing that driving the interaction strength leads to certain bands of momenta that grow exponentially. This establishes the mechanism through which the translational symmetry of the driven superfluid is spontaneously broken. We will then discuss the nonlinear effects that limit the growth of unstable modes and lead to the stabilization of patterns, using a framework that was developed by our collaborators [47].

4.1 Floquet Instability

In this section, we will give a brief derivation of why periodically modulating the scattering length results in the exponential growth of momentum modes at certain wavelengths. The derivation of the instability is based largely on the calculations in [61, 62].

The equation describing the mean-field dynamics of a Bose gas is given by the GPE,

$$i\hbar\frac{d\psi(\mathbf{r},t)}{dt} = \left[-\frac{\hbar^2\nabla^2}{2m} + V(\mathbf{r}) + g(t)|\psi(\mathbf{r},t)|^2\right]\psi(\mathbf{r},t), \tag{4.1}$$

where $V(\mathbf{r})$ is an external potential and $g(t)$ is the time-dependent interaction. While the potential plays a crucial role in the experiment, here we will assume $V(\mathbf{r}) = 0$ to simplify the theoretical description. The driven interaction is of the form

$$g(t) = g_0(1 - r\sin\omega_d t) \tag{4.2}$$

where g_0 is the mean interaction, and ω_d is the drive frequency.

In order to gain insight into the nature of the instability at a finite wavelength, we first consider a single spatial dimension and insert the following *ansatz* of a standing wave with a time-dependent amplitude into Eq. (4.1),

$$\psi(x,t) = \psi_0(t)[1 + w(t)\cos kx], \tag{4.3}$$

where $w(t)$ is a complex amplitude. The prefactor ψ_0 captures the time dependence of the homogeneous "background" field. For the case without driving, this is trivially given by $\psi_0(t) = \psi_0 e^{-i\mu t}$, where $\mu = |\psi_0|^2 g_0$ is the chemical potential. If $r > 0$, it takes the form

$$\psi_0(t) = \psi_0 e^{-i(\mu/\hbar)t - i(\mu/\omega_d\hbar)r\cos\omega_d t} \tag{4.4}$$

as this is a spatially homogeneous solution to Eq. (4.1).

Now turning to the amplitude $w(t)$, we insert the *ansatz* Eq. (4.3) into the time-dependent GPE, finding that

$$\begin{aligned}
\text{LHS} &= \psi_0\mu(1 - r\sin\omega_d t) + i\hbar\psi_0(t)\frac{\partial w(t)}{\partial t}\cos kx \\
\text{RHS} &= \epsilon\psi_0(t)w(t)\cos kx \\
&\quad + \mu\psi_0(1 - r\sin\omega_d t)\Big[1 + 2\,\text{Re}[w(t)]\cos kx + |w(t)|^2\cos^2 kx\Big],
\end{aligned} \tag{4.5}$$

with $\epsilon = \frac{\hbar^2 k^2}{2m}$. Dropping higher order terms in w, one finds

$$i\hbar\frac{\partial}{\partial t}w(t) = \epsilon w(t) + 2\mu(1 - r\sin\omega_d t)\,\text{Re}[w(t)]. \tag{4.6}$$

Gathering real and imaginary parts yields

$$\begin{aligned}
-\hbar\frac{\partial}{\partial t}\,\text{Im}[w(t)] &= [\epsilon + 2\mu(1 - r\sin\omega_d t)]\,\text{Re}[w(t)] \\
\hbar\frac{\partial}{\partial t}\,\text{Re}[w(t)] &= \epsilon\,\text{Im}[w(t)],
\end{aligned} \tag{4.7}$$

which, after a further derivative of the lower equation, results in the closed form

$$\hbar^2\frac{\partial^2}{\partial t^2}\,\text{Re}[w(t)] + [E(k)^2 - 2\mu\epsilon r\sin\omega_d t]\,\text{Re}[w(t)] = 0, \tag{4.8}$$

where $E(k)$ is the Bogoliubov dispersion relation. This is the Mathieu equation, which is a standard differential equation that has applications in a huge variety of fields, ranging from engineering to biology [63, 64]. The solutions to this equation are well known, and, according to Floquet's theorem, can be written as

$$\text{Re}[w(t)] = \text{Re}[f(t)]e^{vt}, \tag{4.9}$$

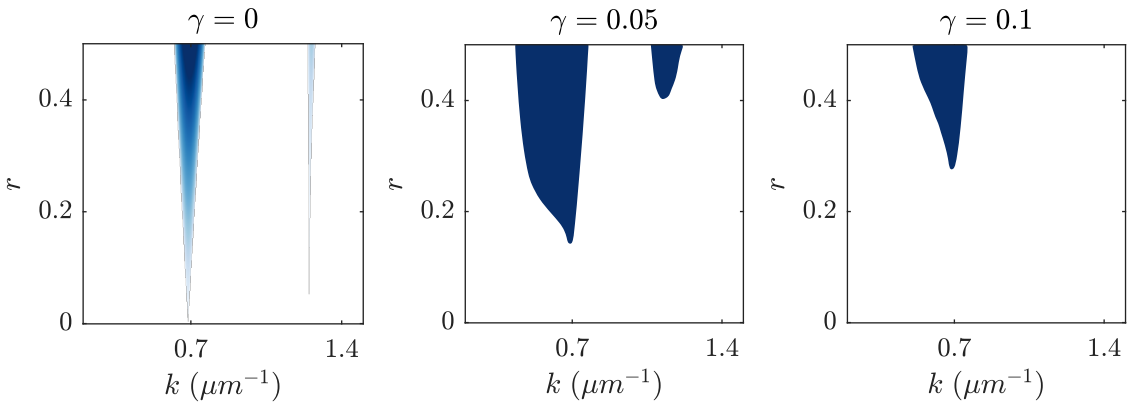

Figure 4.1: Floquet Instabilities. Plots of unstable momentum bands for three different damping coefficients. The horizontal axis is the wavenumber, and the vertical axis is the drive strength. In the left plot, the color map indicates the analytically determined growth rate of the mode, while the right two plots simply show regions where numerical solutions of the Mathieu equation demonstrate growth. In each case, the band gets wider with larger drive amplitude r and bands are localized around specific momenta that correspond to energy and momentum conservation. The plots are produced for $\mu = 2\pi\hbar \times 300\,\text{Hz}$ and $\omega_d = 2\pi \times 400\,\text{Hz}$.

where $f(t)$ is a periodic function that is periodic in $2\pi/\omega_d$ and ν is the Floquet exponent (alternatively, ν/i is known as the Mathieu characteristic exponent). The homogeneous groundstate of the BEC will be unstable to perturbations at a wavenumber k_c if $\text{Re}(\nu) > 0$; a typical feature of these equations is that such instabilities occur in a series of resonance "tongues" for specific frequencies and wavenumbers [2]. Calculating such instabilities is a standard problem in the study of differential equations [63], and a variety of techniques exist to derive them [2, 61, 62]. In this work, a Mathematica package that takes unitless prefactors of Eq. (4.8) as inputs and returns growth rates is used [65].

The left panel of Fig. 4.1 shows the characteristic exponent for chemical potential $\mu = 2\pi\hbar \times 300\text{Hz}$ and drive frequency $\omega_d = 2\pi \times 400\text{Hz}$, without damping. The horizontal axis shows the wavenumber of the perturbation, whereas the vertical axis is the drive amplitude r. The color map shows the magnitude of $\text{Re}(\nu) > 0$, meaning darker blue indicates a faster growth rate of the instability. Multiple bands of unstable momenta are visible, one where $E(k_c) \sim \omega_d/2$, and the next where $E(k_+) \sim \omega_d$. For the lowest-energy mode, this equivalence indicates pair creation of Bogoliubov modes–the driving injects energy into the system, and due to conservation of momentum, pairs of quasiparticles in $\pm k_c$ are created, each with half a quantum of

drive energy. Higher wavelengths are also excited, but here two (or more) quanta of drive energy are absorbed, leading to the growth of higher harmonics.

In the experiment, these dynamics will be modified by damping, due to finite temperature, boundary conditions, redistribution effects, and more (see Chapter 6 for experimental results). In order to heuristically capture these effects, one can introduce a damping term γ:

$$i\hbar\frac{d\psi(\mathbf{r},t)}{dt} = \left[(1-i\gamma)\left(-\frac{\hbar^2\nabla^2}{2m} + g_0|\psi(\mathbf{r},t)|^2\right) - rg_0\sin\omega_d t|\psi(\mathbf{r},t)|^2\right]\psi(\mathbf{r},t). \tag{4.10}$$

This phenomenological damping factor modifies the stability criterion slightly, and broadens the resonance peaks. The full derivation of the instability with damping is similar to the conservative case shown above, but results in a first-order derivative in the Mathieu equation [62].

The left two panels of Fig. 4.1 show the same parameters as the left panel, but now with finite damping. The areas marked in blue are the regions where perturbations grow exponentially, determined by numerically solving the damped Mathieu equation. With increased damping, the instability band broadens and does not reach $r = 0$, as one needs a growth rate large enough to overcome the damping γ. The effect on the second-harmonic band is more significant, such that with experimentally realistic parameters one would not expect the higher order to be unstable.

Thus, we have shown that driving the interaction strength of the superfluid leads to an instability at a given wavelength, which results in the spontaneous breaking of translational symmetry. The instability leads to the exponential growth of occupations at certain length scales. However, this treatment is only valid in the regime of low occupations. In the following, we will discuss how nonlinear effects that have previously been neglected play a role in limiting growth and selecting specific pattern geometries.

4.2 Multiple Scale Analysis

In the 19th century, astronomers such as Anders Lindstedt and Henri Poincaré worked to describe the effect of weak, nonlinear perturbations to periodic orbits [66, 67]. Mathematical descriptions relying on standard perturbation theory lead to unphysical results for long time scales, and problematic terms were deemed "secular" from the Latin *saeculum*, meaning century. Their efforts to remove secular terms formed the basis for what is now known as multiple scale analysis (MSA), which accounts for nonlinear effects that perturb a fast oscillatory solution over a period much longer than one oscillation. As we will see, this method is particularly useful for describing pat-

terns in the driven superfluid, and is widely used in the pattern formation community [2, 53].

This section provides a brief overview of the limits of standard perturbation theory and introduces the technique of MSA using a standard example. The derivation given here is based on [53, 67, 68].

4.2.1 Limitations of Standard Perturbation Theory

In order to move beyond simple linear treatments of differential equations, one often uses perturbation theory, where the nonlinearity of a given differential equation is assumed to be proportional to a small parameter, ϵ. A toy model is the Duffing equation, which is formally very similar to the Ginzburg-Landau equations described above in the context of pattern formation and phase transitions:

$$y'' + y + \varepsilon y^3 = 0. \tag{4.11}$$

Typically, one takes a perturbative *ansatz*, assuming that to first order, $\varepsilon \to 0$ and $\varepsilon > 0$ will modify a solution to the linear problem in the expansion parameter:

$$y(t, \varepsilon) = y_0(t) + \varepsilon y_1(t) + O(\varepsilon^2). \tag{4.12}$$

One then inserts this *ansatz* into the original equation, and solves for the powers of ε separately. This approach, however, can lead to unphysical results to first order, as can directly be seen in this example. Solving for the orders of ε, we find

$$\begin{aligned} \varepsilon^0 &: y_0(t)'' + y_0(t) = 0 \\ \varepsilon^1 &: y_1(t)'' + y_1(t) + y_0(t)^3 = 0, \end{aligned} \tag{4.13}$$

where, without loss of generality, we can assume that $y_0(0) = 1$, and $y_0'(0) = y_1(0) = y_1'(0) = 0$. The solutions to this problem are well known:

$$\begin{aligned} y_0(t) &= \cos t \\ y_1(t) &= \frac{3}{8} t \sin t + \frac{1}{32} (\cos t - \cos 3t) . \end{aligned} \tag{4.14}$$

The first term of the solution for y_1 is clearly unphysical, as it grows linearly in time and will result in unbounded solutions.

The unphysical term hints at the presence of a second time scale, that is much slower than the frequency of the oscillation itself. This is made more apparent by Taylor expanding a cosine with a modulated frequency,

$$y(t) = \cos[(1 + \varepsilon)t] = \cos t - \varepsilon t \sin t + O(\varepsilon^2), \tag{4.15}$$

indicating that the truncation we performed earlier has failed to capture a slowly varying frequency of the oscillation, which is a common feature of solutions to nonlinear differential equations.

An alternative way to describe the problem with the *ansatz* is that it fails when $t \sim 1/\varepsilon$. In the dynamics we wish to study, however, we want to explore dynamics over a large range of timescales, and therefore simple perturbation theory is insufficient.

4.2.2 Strained Coordinates

A key insight from Lindstedt that led to the removal of secular terms was that a primary effect of nonlinearities is the modification of oscillation frequencies [67]. He therefore introduced a new variable, $\tau = \omega(\varepsilon)t$, such that now not only the solution $y(t, \varepsilon)$ is expanded in the small parameter, but also the frequency of the oscillation

$$\begin{aligned} y(t, \varepsilon) &= y_0(\tau) + \varepsilon y_1(\tau) + O(\varepsilon^2) \\ \omega(\varepsilon) &= \omega_0 + \varepsilon\omega_1 + O(\varepsilon^2). \end{aligned} \tag{4.16}$$

This modifies the time derivative

$$\frac{d}{dt} = \omega \frac{d}{d\tau}, \tag{4.17}$$

such that we can write the Duffing equation in the coordinate τ,

$$\omega(\varepsilon)^2 y'' + y + \varepsilon y^3 = 0, \tag{4.18}$$

where the prime now denotes a derivative in τ. One arrives at the conditions

$$\begin{aligned} \varepsilon^0 &: \omega_0^2 y_0'' + y_0 = 0 \\ \varepsilon^1 &: \omega_0^2 y_1'' + y_1 + 2\omega_0\omega_1 y_0'' + y_0^3 = 0, \end{aligned} \tag{4.19}$$

Setting $\omega_0 = 1$ and using the same boundary conditions as above, we straightforwardly find $y_0 = \cos\tau$. The first order equation is therefore reduced to

$$y_1'' + y_1 = \left(2\omega_1 - \frac{3}{4}\right)\cos\tau - \frac{1}{4}\cos 3\tau. \tag{4.20}$$

The term in brackets is still "secular" and must be zero, because it can be shown that the solution for y_1 can only be periodic if there is a single frequency on the RHS [68]. This results in both a condition for ω_1 and a solution to y_1:

$$\omega_1 = \frac{3}{8}, \;\; y_1(\tau) = \frac{1}{32}[\cos 3\tau - \cos\tau] \tag{4.21}$$

The solution

$$y = \cos\omega t + \frac{1}{32}\varepsilon[\cos 3\omega t - \cos\omega t] + O(\varepsilon^2) \tag{4.22}$$

with $\omega = 1 + \frac{3}{8}\varepsilon + O(\varepsilon^2)$ is now valid for all times, in contrast to the solution found using standard perturbation theory, which broke down after short times.

This example demonstrates a key feature of MSA: by making some physically-based assumption about the dynamics of the system (in this case that the solution must be periodic), the conditions that remove secular terms result in new insights, like determining the correction to the oscillation frequency ω. The conditions that remove secular terms are known as the solvability criteria, and are how amplitude equations describing pattern formation will be derived.

4.3 The Amplitude Equation

The dynamics of a pattern in the driven superfluid are precisely the regime in which MSA is useful: we are investigating the dynamics of patterns at a given length scale, where the amplitudes of individual stripes (i.e. standing waves) serve as a proxy for describing structure formation. These stripes have two frequency scales, a fast scale (set by their energy and therefore the drive frequency, according to the resonance condition described in Section 4.1), and a slow scale, set by system parameters such as drive strength and the chemical potential. The fundamental assumption is that these two length scales can be treated separately, as this assumption is what results in the solvability criterion that yields the amplitude equation (AE).

4.3.1 Derivation

The full derivation of the AE is very involved, and will not be discussed in detail here. Instead, the main assumptions and results are presented, and a full derivation can be found in the work of our collaborators, [47], which is based on the one-dimensional calculation presented in [62].

We consider the GPE as written in Eq. (4.1), and now use a typical MSA *ansatz*,

$$\psi(t,\mathbf{r}) = \psi_0(t)[1 + \varepsilon w_1(t,\mathbf{r}) + \varepsilon^2 w_2(t,\mathbf{r}) + \varepsilon^3 w_3(t,\mathbf{r}) + O(\varepsilon^4)] \tag{4.23}$$

with

$$w_1(t,\mathbf{r}) = w_1^k(t,\mathbf{r})\cos\mathbf{k}\cdot\mathbf{r} + w_1^p(t,\mathbf{r})\cos\mathbf{p}\cdot\mathbf{r}, \tag{4.24}$$

and $\psi_0(t) = \psi_0 e^{-i(\mu/\hbar)t - i(\mu/\omega_d\hbar)r\cos\omega_d t}$, identical to the form when deriving the instability. Because we will later only be interested in solvability criteria rather

than full solutions to $w_2(t, \mathbf{r})$ and $w_3(t, \mathbf{r})$, these functions are assumed to be some general superposition of plane waves. Terms up to the third order in ε are necessary to capture the behavior of $w_1(t, \mathbf{r})$. The momentum modes $\mathbf{k}$ and $\mathbf{p}$ are in general entirely independent in both magnitude and direction.

To deal with small amplitudes of stripe patterns (on the order of ε), we assume the driving amplitude is small, $r = O(\varepsilon^2)$, and want to be near the regime of the Floquet instability derived above, $\omega_d - E(k)/\hbar = O(\varepsilon^2)$. The drive amplitude as well as the detuning between the eigenfrequency of the stripe and the drive frequency are therefore scaled with the expansion parameter, and a slow timescale is introduced

$$\tau = \varepsilon^2 t. \tag{4.25}$$

After a lengthy calculation, one finds the following results. The original *ansatz* can be written as

$$\psi(t, \mathbf{r}) = \psi_0(t)[1 + \phi_k(t) \cos \mathbf{k} \cdot \mathbf{r} + \phi_p(t) \cos \mathbf{p} \cdot \mathbf{r}] \tag{4.26}$$

with

$$\phi_{k/p}(t) = \left(1 - \frac{\epsilon + 2\mu}{E}\right) R_{k/p}(t) e^{i\frac{\omega_d}{2}t} + \left(1 + \frac{\epsilon + 2\mu}{E}\right) R^*_{k/p}(t) e^{-i\frac{\omega_d}{2}t}. \tag{4.27}$$

The amplitudes R_k and R_p are complex and vary slowly in time. The magnitude of $R_{k/p}$ is proportional to the contrast of the stripe, while the phase $\arg R_{k/p}$ describes the phase of its oscillation relative to the phase of the drive. The exponential indicates that the contrast of the stripes oscillates with half the drive frequency, which is the fast scale.

The slow variation of the amplitudes on long timescales is given by the solvability criterion for the third order in ε, and is called the amplitude equation:

$$\begin{aligned} i\hbar \frac{d}{dt} R_k(t) = &-i\alpha R^*_k(t) - i\Gamma R_k(t) + \Delta R_k(t) \\ &+ \lambda \left|R_k(t)\right|^2 R_k(t) \\ &+ \lambda \Big[c_1(\theta) \left|R_p(t)\right|^2 R_k(t) + c_2(\theta) R_p(t)^2 R^*_k(t) \Big]. \end{aligned} \tag{4.28}$$

Here, $\alpha = r\frac{\mu\epsilon}{2E}$ is the exponential growth rate from the instability, and $\Delta = \omega_d/2 - E(k)/\hbar$ is a detuning term, which is assumed to be zero, unless stated otherwise. The parameter Γ is a phenomenological damping term that does not come from the amplitude equation, but is instead put into the AE by hand, in order to capture experimental reality. This damping can capture effects like decay and redistribution to other modes. The nonlinearity of the underlying GPE is captured by the prefactor $\lambda = \mu\frac{5\epsilon+3\mu}{E}$.

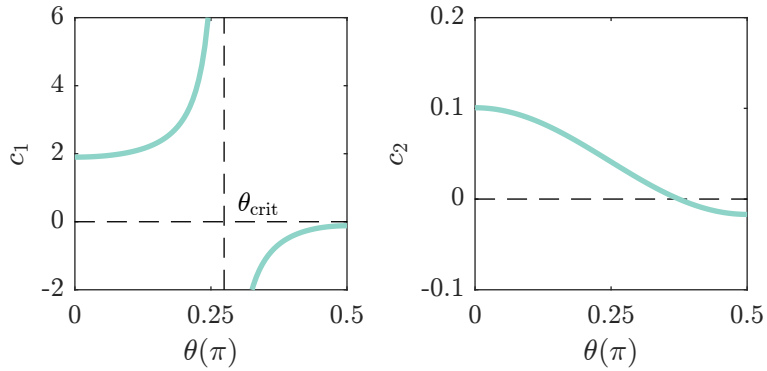

Figure 4.2: Angle-Dependence of Amplitude Equation. Angle-dependence of various factors of the AE. The left shows c_1 the right c_2. The divergence in c_1 is a mathematical artifact and is discussed in detail below. Here, $\hbar\omega_d/\mu = \frac{4}{3}$.

Notably, angle-dependent terms couple the dynamics in R_k and R_p, where the angle $\theta\angle(\mathbf{k}, \mathbf{p})$ is the angle between the wavevectors. The prefactors $c_1(\theta)$ and $c_2(\theta)$ are given by

$$\begin{aligned} c_1(\theta) = \frac{\mu}{5\epsilon + 3\mu}\Bigg[& 4\frac{\epsilon^2 - \mu^2}{\mu\epsilon} + \frac{2\epsilon+\mu}{\epsilon}\frac{2\epsilon+\mu}{2\epsilon\cos^2\frac{\theta}{2} + \mu} \\ & - \frac{(2\epsilon-\mu)(\epsilon+2\mu) + 2\left(2\epsilon^2+\mu^2\right)\cos^2\frac{\theta}{2}}{E^2 - E_+^2/4} \\ & + \left(\cos\frac{\theta}{2} \to \sin\frac{\theta}{2}\right)\Bigg] \end{aligned} \tag{4.29}$$

and

$$c_2(\theta) = \frac{\mu}{5\epsilon+3\mu}\left[-2\frac{\epsilon^2+3\mu\epsilon+\mu^2}{\mu\epsilon} + \frac{2\epsilon+\mu}{\epsilon}\left(\frac{2\epsilon+\mu}{2\epsilon\cos^2\frac{\theta}{2}+\mu} + \left(\cos\frac{\theta}{2} \to \sin\frac{\theta}{2}\right)\right)\right], \tag{4.30}$$

where $E_\pm = \sqrt{\epsilon_{\mathbf{k}\pm\mathbf{p}}(\epsilon_{\mathbf{k}\pm\mathbf{p}} + 2\mu)}$ with $\epsilon_{\mathbf{k}+\mathbf{p}} = 4\epsilon\cos^2\frac{\theta}{2}$ and $\epsilon_{\mathbf{k}-\mathbf{p}} = 4\epsilon\sin^2\frac{\theta}{2}$. Looking at these prefactors, plotted in Fig. 4.2, it becomes clear that $c(1)$ contains a divergence at a specific energy, namely $E_+ = 2E$. These divergences are a result of scattering between the $\mathbf{k}$ and $\mathbf{p}$ mode into the higher harmonic of the drive, and will be discussed in greater detail below.

Finally, we note that the angle between the stripes θ does not change in time in this treatment, and the selection of different pattern geometries is instead captured by the growth and depletion of single amplitudes.

4.3.2 Physical Interpretation

Before discussing the characteristics of the AE in greater detail, we first provide a physical interpretation of the processes being described.

The complex amplitudes $R_k = |R_k|e^{i\varphi}$ describe the contrast of the standing wave, as well as the phase of its oscillation relative to the drive. This phase is a useful quantity in the driven system, because the drive explicitly breaks time-translation invariance, meaning that the drive serves as a clock relative to which we can track the phonon oscillations. This is seen more clearly when expressing the *ansatz* Eq. (4.27) in the density distribution (in one dimension):

$$n(x,t) = \bar{n}\left[1+4|R|\cos\left[\frac{\omega_d}{2}t+\varphi\right]\cos kx+4|R|^2\left(1+2\frac{\mu}{\epsilon}\sin^2\left[\frac{\omega_d}{2}t+\varphi\right]\right)\cos^2 kx\right], \tag{4.31}$$

where $\bar{n}$ is the mean density. Alternatively, the occupations in momentum space for one stripe can be found performing a simple Fourier transform of the *ansatz*, leading to

$$\begin{aligned} n(k,t) &= N_0|R(t)|^2\left[1+2\frac{\mu}{\epsilon}\sin^2\left(\frac{\omega_d}{2}t+\varphi\right)\right] \\ &= N_0|R(t)|^2\left[1+\frac{\mu}{\epsilon}\left[1-\cos\left(\omega_d t+2\varphi\right)\right]\right], \end{aligned} \tag{4.32}$$

where N_0 is the number of atoms in the condensate. In both cases, densities are dynamic: the contrast of the lattice oscillates with $\omega_d/2$, while occupations in momentum space oscillate with ω_d, each with a phase lag φ. The contrast and occupations in momentum space oscillate out of phase, meaning that maximal contrast in real space occurs at the point of minimal occupations in momentum space. We note that Eq. (4.32) has the same form as the mapping of a coherent state of Bogoliubov quasiparticles onto free particles, given by Eq. (3.29), up to prefactors.

It is interesting to consider the amplitude equation in polar representation, where the interplay between the phase and magnitude of the amplitudes becomes apparent:

$$\begin{aligned} \frac{d}{dt}|R_k(t)| =& \Big[-\alpha\cos\left(2\varphi_k(t)\right)-\Gamma \\ &+\lambda c_2(\theta)\left|R_p(t)\right|^2\sin\left(2\varphi_p(t)-2\varphi_k(t)\right)\Big]|R_k(t)| \\ \frac{d}{dt}\varphi_k(t) =& \alpha\sin\left(2\varphi_k(t)\right)-\lambda\Big[|R_k(t)|^2 \\ &+\Big(c_1(\theta)+c_2(\theta)\cos\left(2\varphi_p(t)-2\varphi_k(t)\right)\Big)\left|R_p(t)\right|^2\Big]. \end{aligned} \tag{4.33}$$

Notably, this respresentation shows that the stripe contrast does not simply grow exponentially, but rather depends on the phase φ. Additionally, the dominant coupling

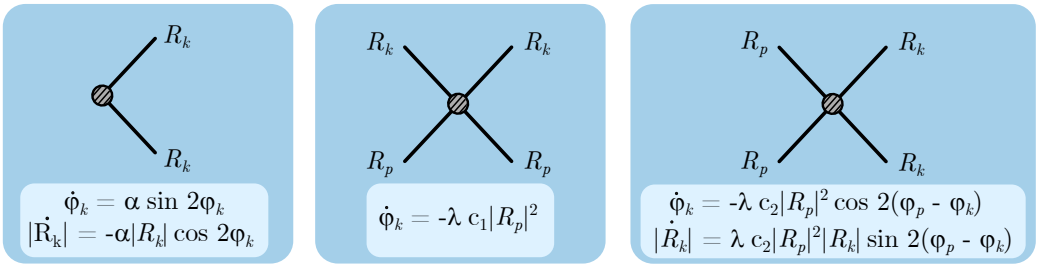

Figure 4.3: Visualization of Processes in Amplitude Equation. Three processes captured by the amplitude equation. Incoming modes (from the left) are annihilated, outgoing modes are created. The dashed circle indicates a condensate-mediated interaction between phonons. The left panel shows the pair-production process, leading to exponential growth of occupations. The central process describes the "contact" interaction between R_k and R_p. The right panel shows the term proportional to c_2. The equations shown beneath each scattering process indicate the change in R_k from the interaction, assuming no change in R_p.

factor between R_k and R_p, $c_1(\theta)$, appears only in the lower equation, indicating the importance of the phase in selecting pattern geometries. Finally, not only the global phase but also the relative phase between the stripes influences dynamics, as is seen in terms proportional to $c_2(\theta)$.

The individual terms of the AE can also be pieced apart, to investigate the processes that they describe. Though the AE was derived classically, we will now use the conceptual framework of phonon-phonon scattering processes to gain an intuition for the mechanism. Fig. 4.3 shows a schematic interpretation of three terms of the AE. To construct these diagrams, we treat $R^{(*)}$ as an annihilation (creation) operator. Using Euler-Lagrange formalism, the time derivative $\frac{d}{dt}R(t)$ is equal to a variation of some effective energy density with respect to R^*. We then use annihilation operators for incoming processes, and creation operators for outgoing processes. The dashed circles at the vertices represent interactions mediated by the condensate. These terms describe changes in R_k depending on the amplitudes $R_{k/p}$.

The left diagram shows the pair creation that originates from the drive. This term effectively costs no energy, as the amplitude equation is in the rotating frame of the drive. The central panel represents the contact interaction between R_k and R_p. Its effect is merely an induced phase of R_k, depending on the occupation in R_p (this is identical to the self-interaction of R_k but without the prefactor c_1).

The term on the right is proportional to c_2, and represents a process in which a pair in R_p is annihilated and scatters into R_k. This process depends on the phase between the phonons, showing that not only the global phase but also the relative

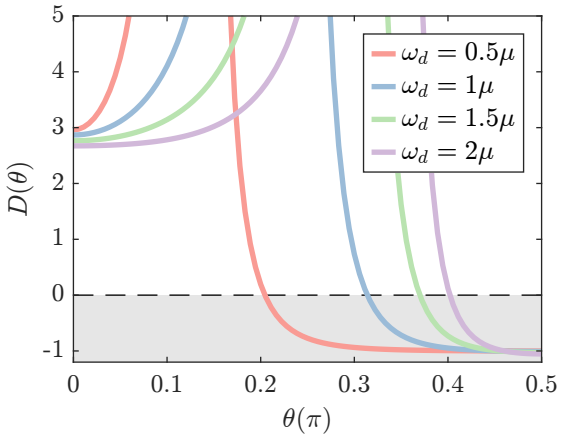

Figure 4.4: Instability Factor. The functional form of the instability factor $D(\theta)$, where regions below zero (shaded) indicate stable lattice solutions. The divergences are an artifact of scattering processes resonant to the shaking frequency and are discussed in detail in Section 4.3.5.

phase between the phonons will play a role in the stabilization process.

4.3.3 Stable Solutions

We will now consider steady-state solutions to these equations, what we will call fixed point solutions. These are straightforwardly found by setting $\frac{d}{dt}R_k = 0$, resulting in three unique points:

$$\begin{aligned} &R_k = R_p = 0, && \text{(Uniform solution)} \\ &R_{k/p} = |R_\mathrm{f}|e^{i\varphi_\mathrm{f}}, R_{p/k} = 0, && \text{(Stripe solution)} \\ &R_{k/p} = R_{p/k} = |R_\mathrm{f}|/\sqrt{1 + c_1(\theta) + c_2(\theta)}e^{i\varphi_\mathrm{f}}, && \text{(Lattice solution)} \end{aligned} \tag{4.34}$$

where $|R_\mathrm{f}|^2 = \frac{\alpha}{\lambda}\sqrt{1 - \frac{\Gamma^2}{\alpha^2}}$, and $\cos\varphi_\mathrm{f} = \frac{\sqrt{1-\Gamma/\alpha}}{\sqrt{2}}$. The first case is a trivial uniform solution, where no pattern emerges. Because this is a mean-field calculation, it does not consider fluctuations, and a small seed is necessary to instigate growth. The second class of solutions is a stripe pattern, where, for the same reason as in the uniform case, the amplitude of the second stripe is exactly zero, and therefore cannot show dynamics. The third and most interesting point is a lattice solution, indicating that for all angles, there should be one solution with non-zero occupation in two momentum modes that is stationary, despite the continued drive.

The presence of a fixed point solution, however, says nothing of its stability. In order to investigate the stability of these solutions, one can perform a linear analysis around the fixed points. By analyzing the behavior of perturbations around the fixed

point solutions, one can determine growth rates of these perturbations, to define a stability condition [47]. The stability condition for the case where $\Gamma = 0$ is given by

$$D = -1 + c_1(\theta)^2 + 2c_2(\theta) - c_2(\theta)^2, \tag{4.35}$$

where if $D < 0$ the lattice fixed point solution is stable, and $D > 0$ indicates it is unstable.

The stability criterion is plotted in Fig. 4.4 for a variety of drive frequencies. It shows that fixed points for angles that are $\sim 90^{\text{o}}$ are all stable, whereas small angles between stripes are unstable. Divergences occur at the angle where the energy of outgoing quasi-particles after a collision are resonant to the drive energy, i.e. $E(\mathbf{k} + \mathbf{p}) = \omega_d$, and are a mathematical artifact that will be discussed in more detail below. We will now turn to the mechanism behind the stability of certain fixed points, by looking at the dynamics of amplitudes.

4.3.4 Phase Space

The AE describes a four-dimensional phase space, as each amplitude has a magnitude and phase that each play an important role in the dynamics. This makes it difficult to visualize the evolution of amplitudes, but a number of reduced "cuts" give insight into the mechanism behind pattern formation.

In Fig. 4.5, two sets of three-dimensional cuts are shown, one for $\theta = 90^{\text{o}}$ and one for 30^{o}. In each case, the magnitude of the two stripes $|R_{k/p}|$ is varied independently, while the phases are coupled: once by simply setting them equal $\varphi_k = \varphi_p$, and once by varying their difference, $\Delta\varphi = \varphi_k - \varphi_p$, such that their average value is set to that of the fixed point, $(\varphi_k + \varphi_p)/2 = \varphi_{\text{fp}}$.

The plots show flow lines from the projection of the first derivative $\frac{d}{dt}R_{k/p}$ onto this cut, while the colors show the flow speed of trajectories in this space. These lines therefore do not show "real" trajectories, as the full four-dimensional flows can exit and enter the shown spaces.

In the case where the phases are equal, one sees in-spirals towards two points, marked in blue and green. These points are the fixed point solutions, with the green marking the lattice point, and the blue marking the stripe solution. The in-spirals reveal a key mechanism of the AE: when the magnitude of the stripes becomes large, it induces a phase shift in the amplitudes. Through the linear term (proportional to α), this phase shift leads to a reduction in the magnitude of the stripe, which eventually leads to more phase dynamics, and the cycle continues. Indeed, without damping, the underlying GPE is conservative, and therefore these trajectories would be periodic without ever reaching the fixed point. Thus, damping plays a crucial role in the emergence of patterns in the experiment.

In the space where the phases are equal, one cannot see why one fixed point is stable while the other is unstable. Moving instead to the space where the difference

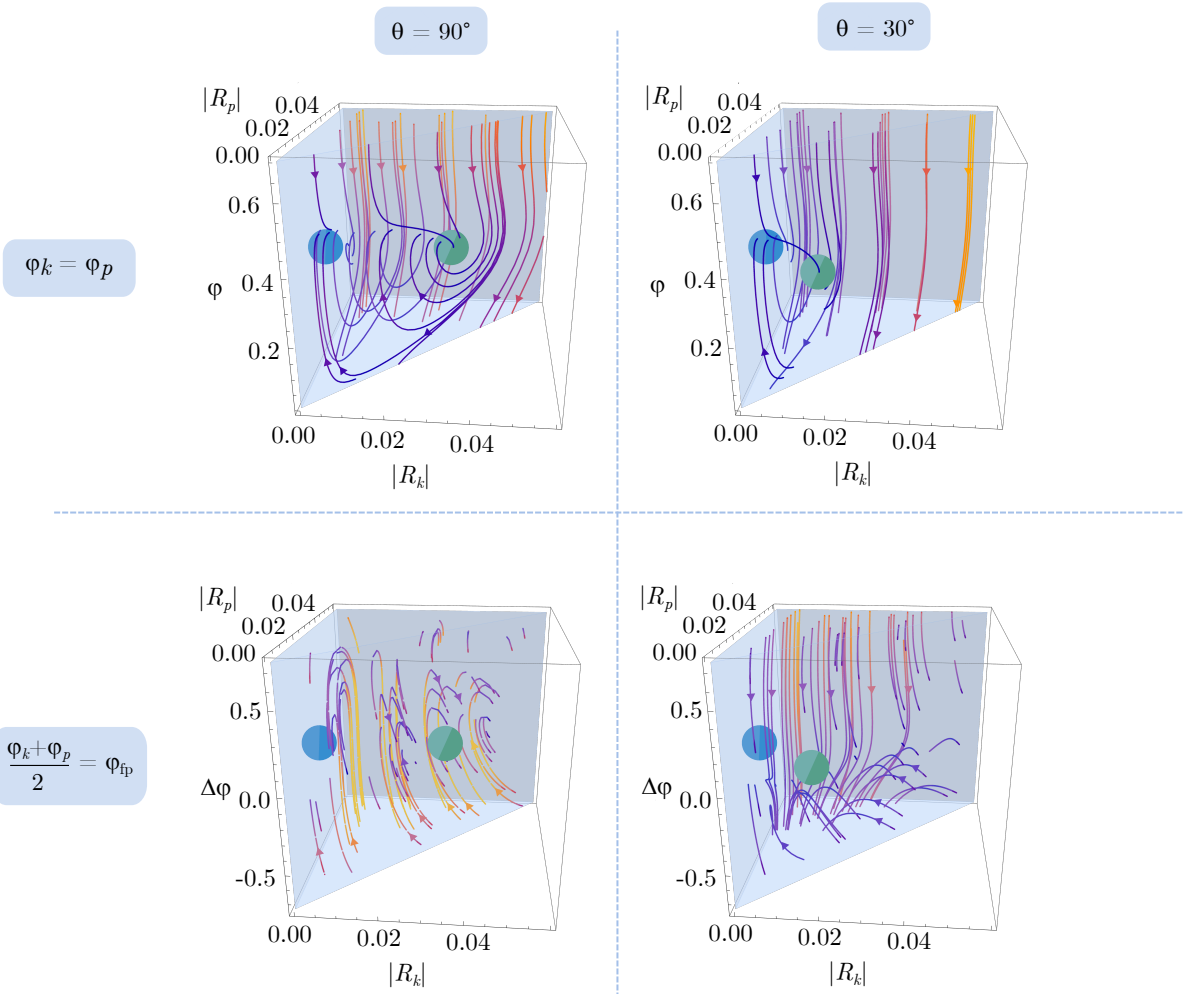

Figure 4.5: Flow of the Amplitude Equation. Flow diagrams in a three-dimensional cut of the full four dimensional space. The lines show trajectories along projections of the first derivative into this cut, with colors showing flow speed. The top row shows the cut where the phases of the two stripes are set to be equal, but magnitudes of stripes are varied independently. The bottom row shows cuts of the space where the phases are varied such that the mean value is always that of the fixed point solution. The left column shows flows for $\theta = 90^o$, the right for $\theta = 30^o$.

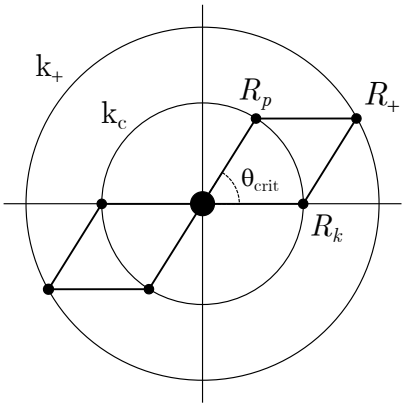

Figure 4.6: Scattering in Higher-Energy Mode. A diagram sketched in momentum space, showing an allowed scattering process into a higher-energy shell. Standing waves R_k and R_p at an angle θ_{crit} can resonantly scatter into the higher shell in the case where $E(k_+) = \omega_d$. The magnitude of k_c and k_+ is therefore determined by the dispersion relation. The ratio k_+/k_c ranges from 2 for low momenta to $\sqrt{2}$ for large momenta.

in phases is varied, the angle dependence becomes pronounced. Here, one sees that a difference in contrast of the stripes can induce a phase difference between the stripes. Looking at the flow patterns, one can again see in-spirals for 90°, but that for 30° the trajectories simply pass by the fixed point, flowing instead towards the stripe solution. Therefore, while for 90° these dynamics stabilize a phase difference of zero and equal contrasts, for 30° a slight phase difference induces a reduction in the contrast of one stripe.

4.3.5 Including Higher Order Modes

So far, we have only discussed the dynamics of stripes at the critical wavenumber k_c, which have energy $E(k_c) = \omega_d/2$. However, modes in this energy shell can scatter into the first harmonic of the drive, where $E(k_+) = 2E(k_c) = \omega_d$. This process occurs at a specific angle, which is determined by the dispersion relation and the geometry of the scattering process (see Fig. 4.6), such that

$$\theta_{\text{crit}} = 2\cos^{-1}\frac{k_+}{2k}. \tag{4.36}$$

For low momenta, the dispersion relation is linear, meaning that $k_+ = 2k_c$, and for high momenta it is quadratic, resulting in $k_+ = \sqrt{2}k_c$. Scattering between resonant energy shells is often discussed in pattern formation and can in general lead to selection of pattern geometries [13, 18]. Indeed, a numerical study of driven superfluids postulates

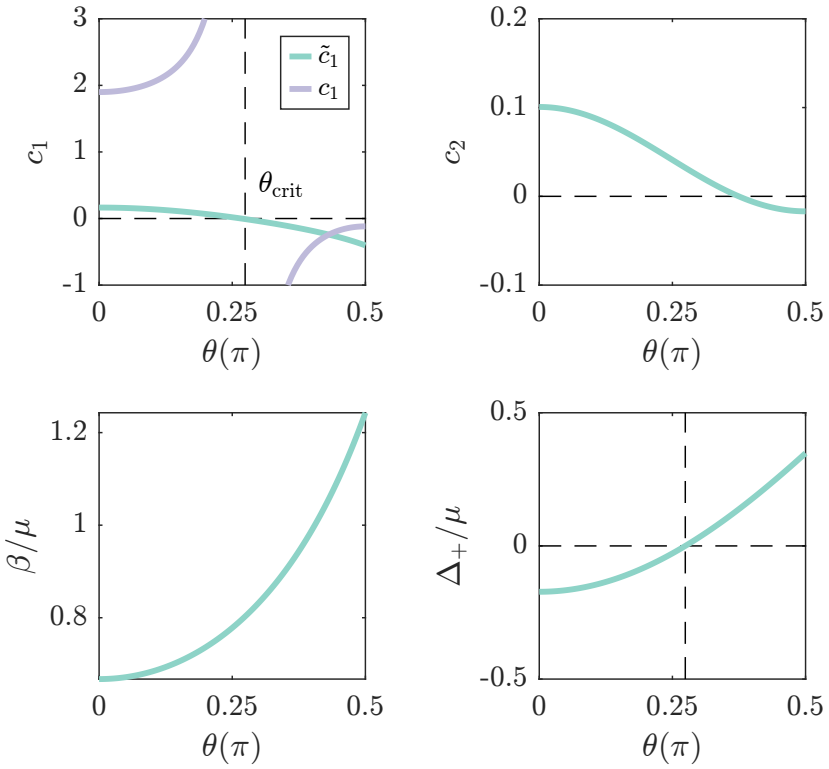

Figure 4.7: Angle Dependence of Amplitude Equation. The top left shows both c_1 and $\tilde{c}_1$, the rop right c_2. The bottom row shows factors in the extended AE, namely β (left), which describes the coupling between the first and second harmonic modes, as well as the detuning of R_+ to the drive frequency (right). Here, $\hbar\omega_d/\mu = \frac{4}{3}$.

that coupling to higher harmonics of the drive is the dominant, geometry selecting process, even with weak driving at a single frequency [61] . We will therefore now explicitly include the higher-energy mode R_+ in the amplitude equation, to investigate if such processes indeed play a role in pattern selection.

In order to extend the AE, a second time scale is introduced, $\tau_1 = \varepsilon t$, together with the original $\tau_2 = \varepsilon^2 t$. With this second time scale, we can incorporate dynamics at yet another energy scale, namely at $E(\mathbf{k}+\mathbf{p})$, extending the *ansatz* to

$$\psi(t,\mathbf{r}) = \psi_0(t)[1+\phi_k(t)\cos\mathbf{k}\cdot\mathbf{r}+\phi_p(t)\cos\mathbf{p}\cdot\mathbf{r}+\phi_+(t)\cos((\mathbf{k}+\mathbf{p})\cdot\mathbf{r})]. \quad (4.37)$$

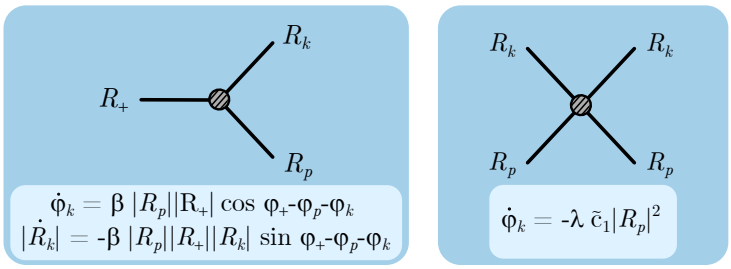

Figure 4.8: Modified Processes in Extended Amplitude Equation. The inclusion of the higher-energy mode R_+ means a new scattering process is included, shown on the left. It shows the process that couples modes at the resonant momentum with those at the first harmonic of the drive. The right process is the modified "contact" interaction between R_k and R_p.

As is shown fully in [47], this results in the coupled equations

$$\begin{aligned} i\hbar\frac{d}{dt}R_k(t) = &-i\alpha R_k^*(t) - i\Gamma R_k(t) + \Delta R_k(t) - \beta(\theta)R_+(t)R_p^*(t) \\ &+ \lambda\,|R_k(t)|^2\,R_k(t) \\ &+ \lambda\Big[\tilde{c}_1(\theta)\,\big|R_p(t)\big|^2\,R_k(t) + c_2(\theta)R_p(t)^2R_k^*(t)\Big] \end{aligned} \tag{4.38}$$

and

$$\begin{aligned} i\hbar\frac{d}{dt}R_+(t) = &-i\Gamma_+R_+(t) + \Delta_+R_+(t) - \beta_+(\theta)R_k(t)R_p(t) \\ &+ \lambda_+\,|R_+(t)|^2\,R_+(t). \end{aligned} \tag{4.39}$$

Here, the subscript "+" indicates that the momentum is now $\mathbf{k}+\mathbf{p}$, i.e. $\epsilon_+ = \frac{\hbar^2|\mathbf{k}+\mathbf{p}|^2}{2m}$, $E_+ = E(\mathbf{k}+\mathbf{p})$, and $\lambda_+ = \mu\frac{5\epsilon_+ + 3\mu}{E_+}$. The detuning term Δ_+ is now relative to the full driving frequency, $\Delta_+ = \omega_d - E_+$ (rather than $\omega_d/2$, as is the case for Δ). There are now factors that account for scattering between the energy shells, defined as

$$\beta = \mu\left(\frac{\epsilon-\mu}{E} + \frac{\epsilon_+ + 2\mu}{E_+}\right), \quad \beta_+ = \mu\left(\frac{\epsilon_+}{\epsilon}\frac{\epsilon-\mu}{E_+} + \frac{\epsilon+2\mu}{E}\right). \tag{4.40}$$

Finally, the prefactor $c_1(\theta)$ is now modified and no longer diverges for $\theta \in [0, \pi/2]$:

$$\begin{aligned} \tilde{c}_1(\theta) = \frac{\mu}{5\epsilon+3\mu}\Bigg[4\frac{\epsilon^2-\mu^2}{\mu\epsilon} - \frac{(2\epsilon-\mu)(\epsilon+2\mu) + \left(2\epsilon^2+\mu^2\right)\epsilon_-/(2\epsilon)}{E^2 - E_-^2/4} \\ + \frac{2\epsilon+\mu}{\epsilon}\left(\frac{2\epsilon+\mu}{\epsilon_+/2+\mu} + (\epsilon_+ \to \epsilon_-)\right)\Bigg]. \end{aligned} \tag{4.41}$$

The magnitude of some these coefficients is plotted in Fig. 4.7. The factor $\tilde{c}_1$ is dramatically reduced in magnitude compared to c_1, because processes that were previously implicitly included in c_1 are now explicitly included via mediated processes through R_+. These mediated terms are captured by β, which is of order μ. For this reason, c_1 and $\tilde{c}_1$ cannot be directly compared. Scattering diagrams for the new and modified processes are shown in Fig. 4.8.

The prefactor $\tilde{c}_1$ still diverges for the angles $\theta \in (\pi/2, \pi]$, due to neglecting the R_- mode. However, the extension to include R_+ has already made the new phase space six-dimensional, and its theoretical description is significantly more involved. Even a stability analysis like in Section 4.3.3 is not straightforward. The extension of the AE should therefore not be viewed as a "more complete" model, but rather is used to address the stability of patterns at the critical angle. To do so, we will now consider numerical solutions of the extended AE.

4.3.6 Numerical Solutions of the Amplitude Equation

Having removed the divergences for the angles $\theta \in [0, \pi/2]$, we will now use numerical simulations to show that indeed only square lattices are expected to be stable, even in the extended amplitude equation.

In the experiment, it is rarely the case that only two stripes are present in the condensate at once. Indeed, considering the dynamics of only two stripes could be misleading, as in certain parameter regimes it is possible that the interactions of three stripes add new dynamics that are not captured by the simplest *ansatz*. In order to account for many interacting modes, we can construct an amplitude equation of arbitrarily many stripes, all with a certain wavenumber but with varying angles [47]:

$$
\begin{aligned}
&i\frac{\mathrm{d}}{\mathrm{d}t}R\left(t,\theta_m\right) = -i\Gamma R\left(t,\theta_m\right) - i\alpha R^*\left(t,\theta_m\right) \\
&- \sum_{n(\neq m)} \beta\left(\left|\theta_m - \theta_n\right|\right) R_+\left(t,\theta_m,\theta_n\right) R^*\left(t,\theta_n\right) \\
&+ \lambda\Big[\left|R\left(t,\theta_m\right)\right|^2 R\left(t,\theta_m\right) + \sum_{n(\neq m)} \tilde{c}_1\left(\left|\theta_m - \theta_n\right|\right) \left|R\left(t,\theta_n\right)\right|^2 R\left(t,\theta_m\right) \\
&+ \sum_{n(\neq m)} c_2\left(\left|\theta_m - \theta_n\right|\right) R\left(t,\theta_n\right)^2 R^*\left(t,\theta_m\right) \Big], \\
&i\frac{\mathrm{d}}{\mathrm{d}t}R_+\left(t,\theta_m,\theta_n\right) = -i\Gamma_+ R_+\left(t,\theta_m,\theta_n\right) + \Delta\left(\left|\theta_m - \theta_n\right|\right) R_+\left(t,\theta_m,\theta_n\right) \\
&- \beta_+\left(\left|\theta_m - \theta_n\right|\right) R\left(t,\theta_m\right) R\left(t,\theta_n\right) + \lambda_+\left(\left|\theta_m - \theta_n\right|\right) \left|R_+\left(t,\theta_m,\theta_n\right)\right|^2 R_+\left(t,\theta_m,\theta_n\right).
\end{aligned}
\tag{4.42}
$$

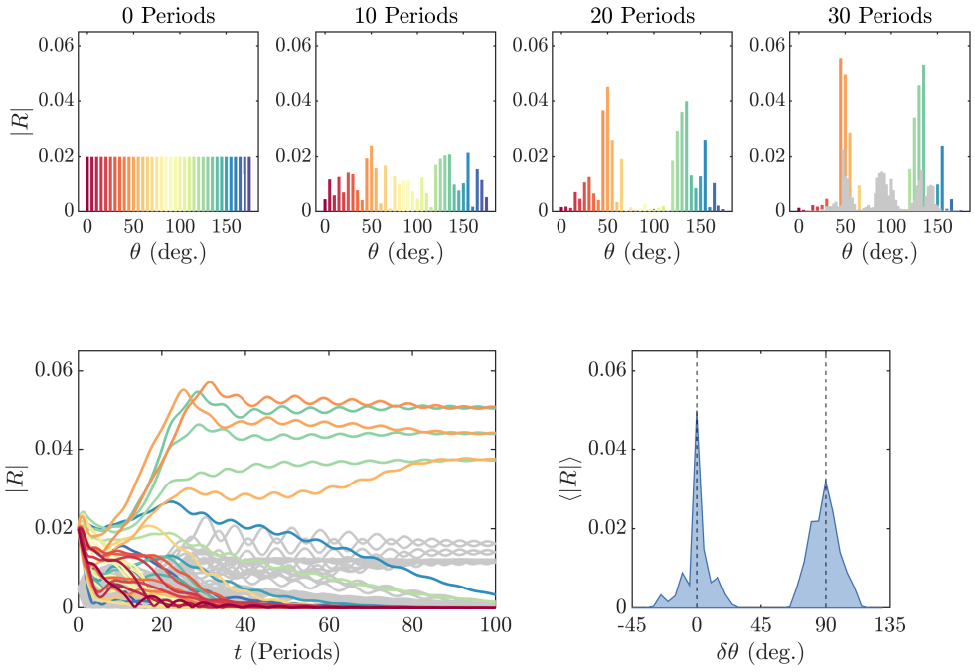

Figure 4.9: Numerical Solution of Many-Mode Model. The top row shows individual modes, with colorful lines showing $|R(\theta_m)|$, and gray lines in the rightmost panel $|R_+(\theta_m, \theta_n)|$. Simulations are run with $r = 0.4$, $\hbar\omega_d/\mu = 4/3$, $\Gamma = \Gamma_+ = 0.5\alpha$, $\lambda = 9\lambda_0$, where λ_0 is the theory value. Initial states have a random phase but equal magnitude, $|R(\theta_m)| = 0.02$ and $|R_+(\theta_m, \theta_n)| = 0.005$. The bottom left shows the same information as the top row, but plotted as traces for all times. The bottom right shows the average distribution after 50 runs, with the mode of maximum occupation defining $\delta\theta = 0$.

While the angle between two stripes can range from $\delta\theta_{n,m} \in [0, \pi]$, the standing-wave nature of the modes makes the coefficients for the R_+ mode symmetric around $\pi/2$. All coefficients for angles $\theta \in (\pi/2, \pi]$ are therefore defined to be $c(\delta\theta_{n,m} > \pi/2) \rightarrow c(\pi - \delta\theta_{n,m})$ to avoid divergences, but are otherwise identical to those used previously.

This set of coupled equations can be solved numerically, with results summarized in Fig. 4.9. Using experimentally realistic parameters, we initially seed many modes from $\theta_m = 0$ to 180^o with magnitudes $|R(\theta_m)| = 0.02$, $|R_+(\theta_m, \theta_n)| = 0.005$, and random phases. The top row shows the distributions at four different times, with the $|R(\theta_m)|$ plotted as solid lines and $|R_+(\theta_m, \theta_n)|$ plotted as gray lines in the rightmost panel. Some modes grow larger than others due to the randomly chosen initial

phase, and at roughly $\pi/2$ separation, another set of modes grows, while others are suppressed. At the latest time, it is apparent that only the $|R_+(\theta_m, \theta_n)|$ modes corresponding to the dominant $|R(\theta_m)|$ modes remain. The same information is plotted as traces in the lower left panel. Here, it is apparent that as the two sets of modes at roughly $\pi/2$ grow, all other modes are diminished.

The lower right panel shows the average phonon occupations after 50 runs as a function of relative angle, where the mode with maximum magnitude is shifted to $\delta\theta = 0$. Here, one sees that the region of stable patterns is not significantly modified to the instability criterion plotted earlier, and no patterns are stable at the critical angle where c_1 diverges (for these parameters, $\theta_{\text{crit}} = 50^{\text{o}}$).

Having addressed the divergence at the critical angle and showing that the region of stable square lattices is relatively unchanged to the two-mode model, further analyses of the AE and comparisons with experimental results will only consider the two-mode model, unless stated otherwise.

4.4 Application to Experiment

The AE represents a highly involved calculation that incorporates nonlinear dynamics and coupling between density waves. It describes processes that have not previously been described theoretically, in particular the angle-dependent interactions between phonon modes of the same energy. Its form motivates that square lattice patterns can be expected to emerge in the driven superfluid over a broad parameter range. However, a number of features limit a quantitative comparison between the AE and experimental results.

For one, the AE includes only a linear, phenomenological damping term, Γ. As will become apparent in later chapters, there are certainly higher-order damping effects that play a role in the experiment. This will modify not only the maximal contrast of the lattice, but also its stabilization.

Additionally, while the incorporation of the R_+ mode in the extended AE removed the divergence at the critical angle, it also shows the importance of higher-order modes in mediating interactions between R_k and R_p. Because essentially every mode has finite occupations in the experiment due to effects like finite temperature, it is unlikely that the AE will deterministically predict dynamics of the experiment.

Furthermore, we have neglected to include the R_- mode, i.e. the mode at $\mathbf{k}-\mathbf{p}$. The inclusion of these processes will likely modify the theoretical description for various reasons. For small angles, the R_- mode will be close to the condensate mode, where occupations are large because of experimental factors like finite temperature and finite size effects, and this could also modify couplings for small angles. Additionally, at $\theta = 90^{\text{o}}$, the modes R_- and R_+ are identical, and this symmetry could result in additional processes that are neglected here.

CHAPTER 5

Experimental Techniques

In this chapter, we review the general features of the experimental system used in this work. We will first give a brief overview of the properties of postassium-39, including its optical transitions and tunable interactions. We then discuss dipole traps, and how a digital micromirror device can be used to tailor lightfields in the atomic plane. The readout of the momentum space distributions using a harmonic trap is described theoretically, and its implementation in the experiment is presented. The cooling stages of the experiment are described, as well as the novel trapping potential used to implement effectively open boundary conditions.

We will focus on the technologies that are either highly relevant for the driven system, or those that have not been described in detail in previous work, such as the momentum space measurement. Further details on the experimental system can be found in Refs. [69, 70]. For details on the digital micromirror device, see Refs. [69, 71]. For systematic measurements on the trapping geometry, see Ref. [72].

5.1 Optical Transitions of Potassium-39

Our experiment utilizes potassium-39, a bosonic isotope that features a number of experimentally useful characteristics. The electronic groundstate is the $^2S_{1/2}$ state, and there are two excited states $^2P_{1/2}$ and $^2P_{3/2}$ that are addressable with near-infrared light. The transition to the $^2P_{1/2}$ state is known as the D1 line, and has wavelength of 770.108 nm, while the transition to $^2P_{3/2}$ is called the D2 line, with a wavelength of 776.701 nm.

The $^2S_{1/2}$ state is further split into two hyperfine states, $F = 1$ and 2, with a splitting of $\sim$ 450 MHz. The D1 excited manifold is similarly split into two states (with a splitting of ~55 MHz), while the D2 excited state has four hyperfine substates ($F = 0$ to 3), which are so tightly spaced in energy relative to their natural linewidth

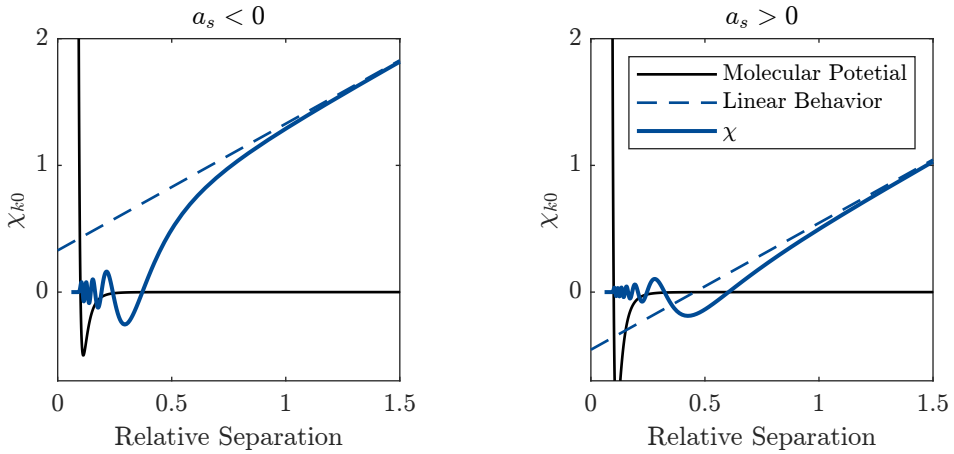

Figure 5.1: Solutions for $\chi_{\mathbf{k0}}$. The numerical solutions of Eq. (5.4) are shown for two potentials, both of the form $V(r) = V_0\left[\left(\frac{\sigma}{r}\right)^{12} - \left(\frac{\sigma}{r}\right)^{6}\right]$ (solid black line), with two different values of V_0. Far from the potential, one recovers linear behavior, where the slope and intercept can be uniquely determined using a delta peak potential. Figure inspired by [59].

that they are not individually addressable by laser light. As is typically the case with alkali atoms, two laser frequencies are needed for laser cooling, a "cooler" for addressing the $F = 2$ and a "repumper" addressing the $F = 1$ states in the $^2S_{1/2}$ manifold. A consequence of this tight spacing of the D2 line is that equal amounts of cooler and repumper are needed to cool potassium. While the D2 line is used for magneto-optical traps (MOT), the D1 line is used for sub-doppler cooling in a gray molasses.

5.2 Feshbach Resonances

Tunability of the interactions between atoms in the condensate is the key mechanism of implementing the driven nonlinearity as discussed in the previous chapter. The phenomenon behind this mechanism is known as a Feshbach resonance. We will first briefly discuss the theoretical mechanism behind Feshbach resonances and then present the specific case of ^{39}K.

5.2.1 Description of Scattering Process

To give some intuition on how Feshbach resonances work, we will consider a simplified model of a scattering process between two neutral atoms, with derivations following the references [58, 59]. Scattering can be described using the relative

wavefunction of two atoms in a scattering process, ψ. For particles with isotropic interactions, the wavefunction at large distances will have the form

$$\psi = e^{ikz} + f(\theta)\frac{e^{ikr}}{r}, \tag{5.1}$$

where spatial coordinates are the relative distance between the atoms, the plane wave e^{ikz} describes the two incoming particles, and $f(\theta)$ is the scattering amplitude. At low momenta, the scattering amplitude converges to a constant, $-a$, known as the scattering length. For low momenta and large distances, the wavefunction therefore reduces to an approximate form

$$\psi \sim 1 - \frac{a}{r}. \tag{5.2}$$

The value of the scattering length a is a function of the atomic interaction potential, which can be seen when considering a simplified model of a scattering process.

Scattering between two particles can be fully described by expanding the wavefunction in terms of radial functions and Legendre polynomials P_l,

$$\psi = \sum_{l=0}^{\infty} P_l(\cos\theta)\frac{\chi_{kl}}{kr}, \tag{5.3}$$

where the radial functions χ_{kl} satisfy the Schrödinger equation

$$\frac{d^2}{dr^2}\chi_{kl} - \frac{l(l+1)}{r^2}\chi_{kl} + \frac{2m^*}{\hbar^2}[E - V(r)]\chi_{kl} = 0. \tag{5.4}$$

Here, m^* is the reduced mass of the two atoms, E is their effective kinetic energy, and $V(r)$ is the interparticle scattering potential. At low momenta, we can consider only s-wave scattering, indicating that $l = E = 0$. In this regime, we can investigte the dynamics of χ_{k0} for a toy interaction potential by numerically integrating Eq. (5.4). One such toy potential is the Lennard-Jones potential,

$$V(r) = V_0\left[\left(\frac{\sigma}{r}\right)^{12} - \left(\frac{\sigma}{r}\right)^{6}\right], \tag{5.5}$$

where the parameter σ sets the point where the potential crosses the zero and V_0 is proportional to the potential depth. Numerical solutions of Eq. (5.4) are shown in Fig. 5.1, for two different values of V_0. While the dynamics for small r are complicated, at large separation the function becomes linear, and we recover the expected form $\psi = \frac{\chi_{k0}}{r} \propto 1 - \frac{a}{r}$. Here, one can see that complicated dynamics from the interaction potential $V(r)$ can be summarized by simple parameters in the far field where $V(r)$ 0.

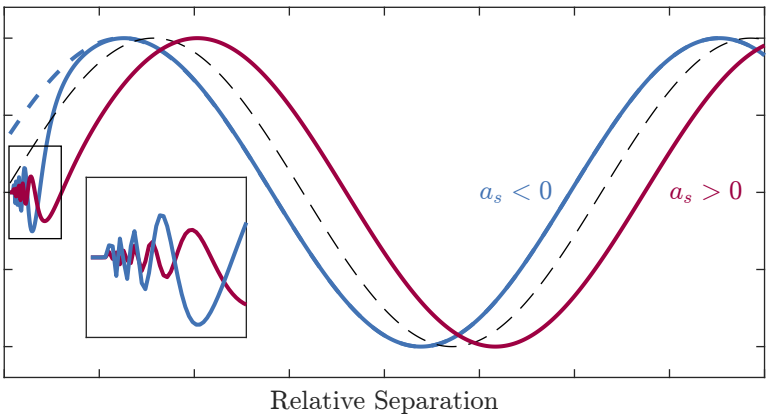

Figure 5.2: Physical Interpretation of Feshbach Resonances. Red and blue curves show χ_{k0} for two different molecular potentials. While at close ranges they show highly oscillatory behavior, at larger distances the difference can be summarized by a phase shift.

In a cloud of many interacting atoms, the specifics of the atomic interaction are irrelevant, as the atomic spacing is typically orders of magnitude larger than the scale of the interaction potential. Therefore, only the behavior at large separations (the linear wavefunction) is needed to sufficiently describe the dynamics. It can be shown that the delta peak pseudopotential

$$V_{\text{ps}} = \frac{4\pi\hbar^2 a_s}{m}\delta(r) \tag{5.6}$$

imposes boundary conditions that result in the correct far-field behavior, namely a discontinuity in the first derivative at $r = 0$, parameterized by the scattering length a_s [59]. Using this pseudopotential instead of the full interaction potential results in the GPE as discussed in Chapter 3.

5.2.2 Physical Interpretation

In the above framework, we have assumed $E = 0$, as well as a wavenumber that is approximately zero. In practice, this is obviously not the case, and a more detailed study reveals that the dynamics described above are independent of the precise wavenumber k, given that the energies are low enough [59]. At large separations and finite E, the centrifugal term and $V(r)$ of Eq. (5.4) are zero, and the solutions to χ_{k0} are simply sine waves. Alternatively, the approximate linear form of χ_{k0} can be viewed as the first terms of the Taylor expansion of a sine wave.

As is plotted in Fig. 5.2, the physical interpretation of the scattering length a_s becomes clearer: while the dynamics at small distances $r \sim 0$ are complicated, in

the far field, the effects can be summarized by a phase shift of the outgoing wave. The complex details of the interaction potential can be summarized using the simple pseudopotential, as the delta peak sets the boundary conditions for the sine wave at $r = 0$, which fully determines the phase of the wave at large distances. The fact that these phase shifts result in effective repulsion and attraction between atoms is less straightforward, and is best understood by considering the effect of the delta-peak pseudo potential in the GPE.

5.2.3 Interaction Potential and Magnetic Field

We will now discuss how molecular potentials (and with that the scattering length a_s) are tuned in practice. The interaction between neutral atoms consists of an attractive van der Waals interaction and repulsion of the atomic nuclei. These two competing effects give rise to a combined potential, schematically shown in Fig. 5.3. This potential has a number of bound states, which are the ro-vibrational states of a so called Feshbach molecule. The spontaneous formation of a molecule from two incoming atoms is energetically not allowed due to energy conservation of the atoms' initial kinetic energy, but, as was described before, the interaction results in a phase shift of the de Broglie wave after the scattering process. These dynamics cannot be tuned through external control knobs, as the interaction potential is set by the physical characteristics of the interacting atoms, and the phase shift accrued due to this interaction sets the background scattering length, a_{bg}.

The interaction between atoms can be tuned due to a second molecular state, one with a different hyperfine configuration of constituent atoms (e.g. a triplet vs. singlet molecular state). If the second molecular configuration has a different magnetic moment compared to that of the incoming atoms, one can shift the interaction potentials relative to one another using an external magnetic field, B. It is now possible to tune the effective interaction potential, such that quasibound molecular states can be shifted in and out of resonance with the scattering state of the colliding atoms, shown in red and blue in the left panel of Fig. 5.3. Here, a "resonance" indicates that the phase shift of the outgoing wave is π.

Near such a resonance, the scattering length a is given by the equation

$$a(B) = a_{\mathrm{bg}} \left(1 - \frac{\Delta}{B - B_0}\right), \tag{5.7}$$

where Δ is the width of the Feshbach resonance and B_0 is the magnetic field where the molecular state is resonant to the incoming particles. Though in theory these parameters can be determined by solving the Schrödinger equation for the molecular potentials (as done for the toy model above), in practice this is extremely challenging, and precise values are determined experimentally.

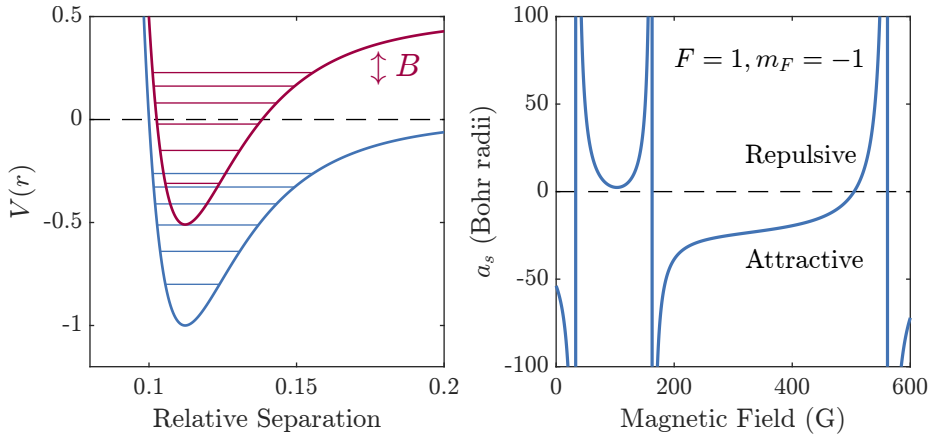

Figure 5.3: Feshbach Resonances in Potassium. The left plot shows the shifting of a bound molecular potential (red) with a different magnetic moment than the molecular potential for two free particles (blue) using an external magnetic field. Shifting a bound state on resonance with the incoming scattering state modifies the effective interaction potential. Right, the scattering length of ^{39}K in the state that corresponds to $|F = 1, m_F = -1\rangle$ at low fields [73].

5.2.4 Feshbach Resonances in Potassium

In the experiment, we work with atoms in the state $|F = 1, m_F = -1\rangle$. This substate has three Feshbach resonances at intermediate fields, shown in Fig. 5.3, which are typically very broad, making the interaction highly tunable with experimentally achievable magnetic field control. In particular, the Feshbach resonance at 561.1 G has the key feature that interactions can be tuned from highly repulsive to moderately attractive, with a zero-crossing. This allows for a huge range of dynamics, as well as the sudden switching off of interactions, which is necessary for momentum space imaging. We will therefore always work in the vicinity of this resonance.

5.3 External Potentials with Light Fields

While tuning the interactions is an extremely useful and versatile experimental tool, these interactions are typically constant throughout the cloud, as magnetic fields vary slowly in space. Local control over the cloud is more easily achieved with light field potentials, and this section will discuss relevant concepts and experimental techniques to do so.

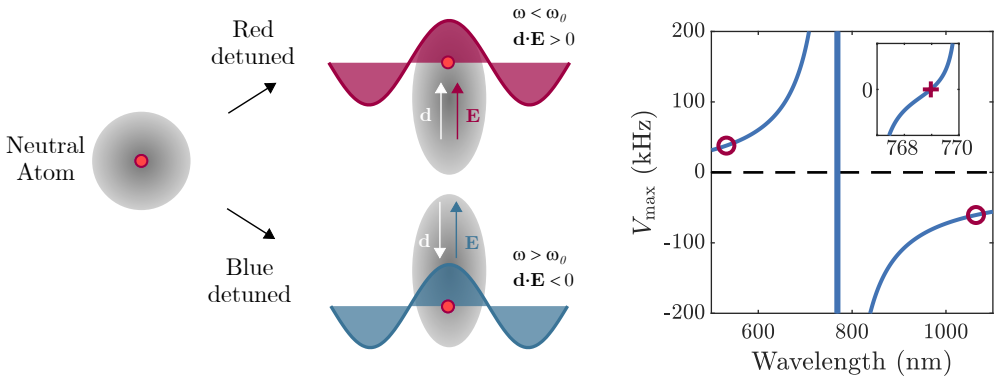

Figure 5.4: Dipole Potentials. Left and center, schematics showing an intuitive picture for the mechanism of a dipole trap. Below (above) the resonance frequency, the atom is polarized in (out) of phase with the light, generating an attractive (repulsive) potential. Right, the maximal potential generated by a dipole beam with 100 mW of power and a waist of 100 μm. In the experiment, red-detuned dipole beams are at 1064 nm, and blue-detuned beams are at 532 nm, marked with red circles. The tune-out wavelength is 768.97 nm, marked in the inset.

5.3.1 Dipole Potentials

An important tool for manipulating ultracold gases of neutral atoms is light that is far detuned from a natural transition of the atom. This detuning means that rather than addressing the atoms through resonant scattering processes (like in a magneto-optical trap), the interaction is better described in terms of the polarization of atoms in an oscillating electric field. The trapping potential that results from the interaction between the dipole of the polarized atom and the electric field is known as a dipole potential.

The mechanism behind dipole potentials can be illustrated using a toy model of an electron elastically bound to the atom core [74]. The light represents an oscillating electric field $\tilde{E}$ with frequency ω that drives the electron-atom system, which is treated as a damped harmonic oscillator with a resonance frequency of ω_0 and damping Γ_ω. The polarizability can then be found to be

$$\alpha = \frac{e^2}{m_e}\frac{1}{\omega_0^2 - \omega^2 - i\omega\Gamma_\omega}, \tag{5.8}$$

where e is the elementary charge and m_e is the mass of the electron. As with any oscillator, the polarizability is therefore in phase with the drive if $\omega \ll \omega_0$, and π out of phase if $\omega \gg \omega_0$.

The polarized atom has a non-zero, oscillating dipole moment,

$$\tilde{d} = \alpha \tilde{E} \tag{5.9}$$

and the interaction potential of the induced dipole moment in the driving field is

$$V_{\text{dip}} = -\frac{1}{2}\langle \mathbf{d} \cdot \mathbf{E} \rangle \propto -\,\text{Re}(\alpha) I, \tag{5.10}$$

where the factor of $1/2$ results from the fact that the dipole is induced, and I is the intensity of the light. Thus, by tuning the spatial shape of the intensity distribution, we can create arbitrary potential landscapes for the atoms.

5.3.2 Digital Micromirror Device

Digital micromirror devices (DMD) have become a standard experimental tool in the cold atom community [75–78]. DMDs are arrays of millions of micromirrors, which can be individually switched between two positions, such that light can be either dumped (the "off" configuration) or directed towards the experiment ("on" configuration). Originally developed for standard projectors, they can be used to tailor light fields to have arbitrary shapes, beyond purely gaussian beams. In cold atom experiments, one typically shines a laser of a far-detuned wavelength onto the mirror array, and uses high-resolution optics to re-image the chip in the atomic plane. Though mirrors can only be switched on and off, grayscales can be produced by re-imaging the mirror array with an optical resolution that cannot resolve individual mirrors. The specifics of the implementation of the DMD in the experiment are given in Refs. [69, 71], and only a summary is given here.

The DMD is implemented in the direct imaging configuration. The full chip has 2560×1600 individual mirrors that are each 7.6μm wide, and typically a square region of 1600×1600 mirrors is used. A laser field with wavelength of 523 nm is used to illuminate the chip, making the potential blue-detuned and therefore repulsive for the atoms. The chip is demagnified by a factor of 86.7, with a resolution in the atom plane of $< 1.0\mu$m, resulting in around 100 grayscales.

To use the DMD, we prepare grayscale images of intensities, that are then binarized using a Floyd-Steinburg dithering algorithm. These binarized images are then uploaded onto the DMD, which displays a new image from a sequence with an external trigger. The fastest switching rate between images is 10kHz.

5.3.3 Thomas-Fermi Approximation

The DMD enables us to experimentally implement tunable external potentials in the atom plane. In the presence of such an external potential, the ground state of the GPE

is modulated, as is described by the Thomas-Fermi approximation. Specifically, in the regime of high densities (or high interactions), the nonlinear term dominates over the kinetic term, resulting in the form

$$i\hbar\frac{\partial}{\partial t}\psi(\mathbf{r},t) \approx \left[V(\mathbf{r}) + gn(\mathbf{r})\right]\psi(\mathbf{r},t), \tag{5.11}$$

which has the solution

$$\psi(\mathbf{r},t) = \sqrt{n(\mathbf{r})}e^{-i\mu t}, \tag{5.12}$$

where μ is the chemical potential and the density $n(\mathbf{r})$ is given by

$$n(\mathbf{r}) = \frac{\mu - V(\mathbf{r})}{g}. \tag{5.13}$$

Intuitively, the density is larger where the potential is lower, and the interaction energy and potential always compensate each other such that the local energy density is given by the chemical potential.

Experimentally, this means that we can shape the density by projecting arbitrary light fields onto the condensate, using the DMD. Because the approximation fails when the kinetic term is large (i.e. ψ has high curvature), sharp jumps in the potential are smoothed in the density on the scale of the healing length. Spatially tuned potentials will be used to shape the boundary conditions as well as to seed phonons of specific orientations.

5.4 Momentum Space Imaging

A key experimental technique for studying the emergence of momentum modes is the extraction of the momentum distribution. Experiments use a variety of methods to extract information about momentum distributions, ranging from Fourier transforms of densities to measuring distributions after a long time of flight (i.e. free expansion).

A different method for measuring momenta is a so-called "focused time of flight" scheme in a harmonic trap. Here, one takes advantage of the elliptical nature of phase space trajectories in a harmonic trap to map information about the momentum distribution onto a real space distribution that can be directly imaged. In order to perform such a measurement, interactions and all external traps are rapidly switched off, and the cloud evolves freely in a harmonic trap for a quarter trap period; then, the cloud is imaged using standard imaging techniques.

This method offers a number of benefits: it provides an instantaneous measure of the momenta, reveals information about back-to-back correlations ($\pm k$), and can be used in the same imaging configuration as real-space imaging, making it convenient to

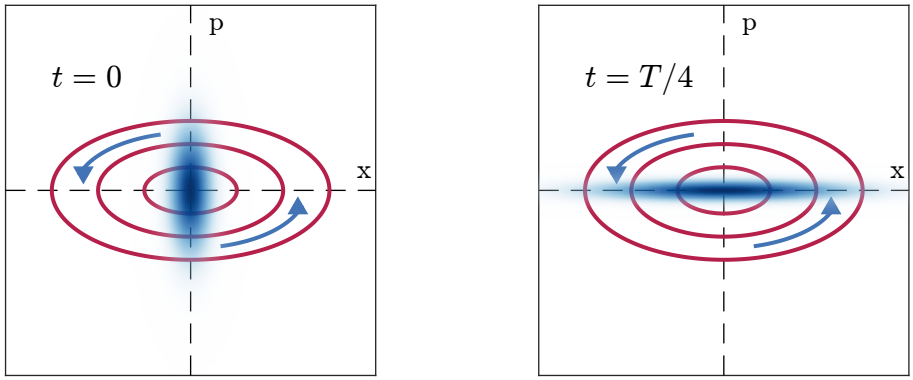

Figure 5.5: Phase Space Rotation in a Harmonic Trap. The red lines show closed trajectories in a phase space defined by a harmonic trap. The blue distribution is initially elongated in p (left), and a quarter period later in x. Because of the closed trajectories, the projection of the distribution onto the x axis at $t = T/4$ is equivalent (up to scaling factors) to the projection onto the p axis at $t = 0$.

rapidly switch between real and momentum space. First experimentally demonstrated in 2010 [79], it has since been adapted and expanded in a huge variety of settings [80–82].

The theoretical description of the technique relies on the symmetry of space and momentum in a harmonic trap. The phase space of a harmonic trap is characterized by closed ellipses, as shown schematically in Fig. 5.5. This means that particles with a given position and momentum will return to exactly the same position and momentum one period later. Another consequence is that projections onto either the momentum or position axis are interchangeable (up to a scaling factor) after a quarter period. Indeed, it can be shown that [80]

$$\begin{aligned} n(x, t = T/4) &= \langle \psi^\dagger(x, T/4)\psi(x, T/4)\rangle \\ &= \langle \psi^\dagger(p, 0)\psi(p, 0)\rangle \\ &= n(p, t = 0), \end{aligned} \tag{5.14}$$

where $p = m\omega_h x$ and T is the period, $T = 2\pi/\omega_h$. In general, measuring the distribution after a quarter period rotation reveals different information than the Fourier transform of the density, because $\langle \mathcal{F}[\psi^\dagger(x)]\mathcal{F}[\psi(x)]\rangle \neq \mathcal{F}[\langle \psi^\dagger(x)\psi(x)\rangle]$.

5.5 Preparation of the BEC

The main cooling and preparation stages are shown in Fig. 5.6. The experiment starts with a 2D MOT, which is loaded from the background vapor of potassium in

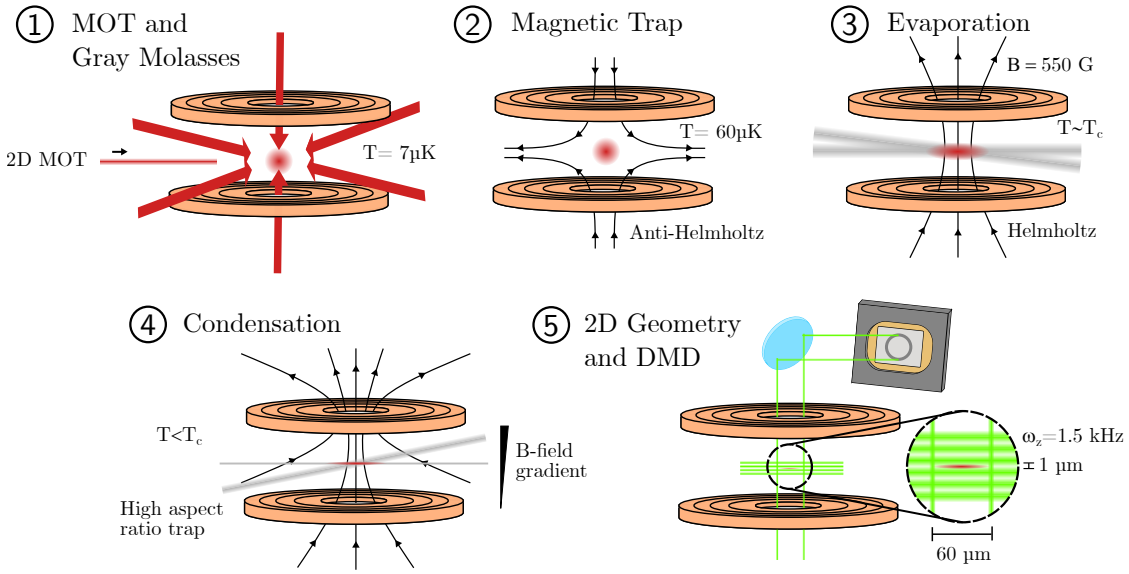

Figure 5.6: Preparation of the BEC. (1) An atom beam from a higher-pressure chamber loads a 3D MOT, which is followed by a gray molasses. The temperature after these stages is roughly 7μK. (2) Atoms are held in a magnetic trap with an anti-Helmholtz configuration and compressed, leading to a slightly higher temperature of 60μK. At this stage, only atoms in the $|F = 1, m_F = -1\rangle$ state are trapped. (3) Evaporative cooling in large dipole traps, to just above the critical temperature. (4) More tightly-confined dipole traps complete the evaporative cooling and lead to condensation. A magnetic field gradient in the vertical direction is ramped up to levitate the atoms against gravity. (5) The atoms are loaded into the minimum of a blue-detuned standing wave in the vertical direction for compression into a 2D geometry. Radially, atoms are confined using the DMD.

a higher-pressure chamber ($< 10^{-8}$ mbar). This 2D MOT generates a beam of cold atoms that is transferred through a differential pumping stage to a 3D MOT in the science chamber, a glass cell that is at a lower pressure ($< 10^{-11}$ mbar). After loading the MOT for $\sim$ 3 s, we use a gray molasses for sub-doppler cooling [83], achieving temperatures of 6 μK. Atoms are optically pumped into the $F = 1$ state by switching off the repumping light at the end of the gray molasses.

After the gray molasses, the magnetic field is switched on in an anti-Helmholtz configuration, resulting in a magnetic trap. A key feature of the magnetic substate $|F = 1, m_F = -1\rangle$ is that it is a low-field seeker at low fields, and a high-field seeker at intermediate to high fields (transition around 100 G). Because the other two substates, $|F = 1, m_F = 0, 1\rangle$, are high field seekers, the magnetic trap only confines the desired

$|F = 1, m_F = -1\rangle$ state. The trap also compresses the cloud, leading to an elevated temperature of $\sim 60\mu$K.

While atoms are trapped in the magnetic trap, two high-power infrared beams (1064 nm) with large beam waists are ramped up, optically trapping the atoms. These beams cross at a small angle, creating a large trapping region. Once many atoms are trapped and the beams are at their maximal power, the magnetic field is rapidly switched to a Helmholtz configuration, and ramped up to the vicinity of Feshbach resonance at 561 G. A scattering length of 160 a_0 is used for evaporation. The intensity of the large dipole traps is then ramped down over around 2.5 s, evaporatively cooling the atoms.

In order to further cool and vertically confine the atoms, two weaker, more tightly focused infrared dipole traps are ramped up while the large beams are ramped down. The atoms are cooled below the critical temperature in these weaker traps with a cooling ramp over 1.7 s, forming a BEC with a high aspect-ratio geometry, like a surfboard. Finally, we ramp up a vertical gradient in the magnetic field while keeping the offset value at the atoms constant; this levitates the atoms against gravity [69, 70].

Having cooling the atoms to degeneracy, we begin the process of shaping the cloud to the desired 2D geometry. The BEC is transferred from the surfboard infrared dipole traps into a trapping potential generated by the DMD, using an initial shape that neatly matches the elliptical geometry of the dipole traps.[1] A one-dimensional lattice in the vertical direction is then ramped up. The lattice is generated by two 532 nm beams that interfere at a shallow angle, generating a standing wave with a spacing of 5 μm, and a trap frequency of $\omega_z = 2\pi \times 1.5$ kHz. Due to the high trap frequency, the BEC has a Gaussian density distribution in the vertical axis with width $\sigma_z \sim 0.5$ µm. In order to ensure that only one lattice minimum is loaded, we regularly tune the spatial phase of the lattice using a piezoelectric element behind the last mirror of one of the lattice beams. Finally, the potential generated by the DMD is slowly reshaped into the desired form, and the scattering length is ramped to the value for experiments.

The cloud is imaged at high fields with absorption imaging, using a scheme described in detail in Refs. [69, 84]. A 10 μs pulse of collimated imaging light hits the atoms from above, and a high-resolution objective with NA$\sim$0.5 collects the photons not scattered by the atoms. After passing through a secondary lens, the light is re-imaged onto a CCD camera. A short time after the first imaging pulse, a second pulse of light is imaged without atoms, and the atomic density is calculated using standard techniques for absorption imaging [85]. The imaging light targets the D2 transition but contains two frequencies, as the state that corresponds

[1] It was experimentally determined that loading the BEC from the infrared dipole traps into a circularly symmetric potential results in the proliferation of vortices in the cloud. This is likely due to the rapid expansion of the tightly-confined axis after ramping down the infrared dipole trap. Using a DMD potential that matches the geometry of the infrared dipole potentials dramatically reduced the number of vortices observed in the cloud.

to $|F = 1, m_F = -1\rangle$ at low fields has slight admixtures of a second $|m_J, m_I\rangle$ state at the magnetic fields used for experiments. Using two frequencies of light results in a nearly closed four-level system.

The entire experimental cycle takes around 16 s, and the experiment is equipped with a variety of safety features such that it can run continuously, including over night and over weekends. Under good conditions, the final BEC contains approximately 40,000 atoms, with shot-to-shot fluctuations in atom number of $\sigma_N = 2.5\%$.

5.6 Slox Potential

Finite size is an unfortunate experimental reality. While theoretical descriptions of quantum systems are often calculated in infinitely extended, homogeneous settings (see Chapters 1-3), experiments must always contend with additional affects from the confinement of the finite system.

When DMDs first became widely integrated into cold atom experiments in the late 2010s, they were billed as the solution to the problem of having to account for harmonic traps in theoretical models [86]. Due to the ability to arbitrarily shape light fields, experimentalists could now produce essentially infinitely steep walls, leading to flat density distributions. However, steep walls come with their own set of challenges: boundary effects of these systems can provide unwanted excitations, such as collective box modes or reflections, limiting applications to studying long-time dynamics or infinitely extended systems. In the course of this thesis, we therefore developed a new trapping geometry that has the benefits of a flat bulk density, while minimizing boundary effects.

5.6.1 Potential Shape

In order to mitigate the effects of boundary conditions in a finite size system, it is beneficial to minimize reflections of excitations at the boundary of the condensate. In principle, this can be done by smoothly decreasing the speed of sound at the system's edge, by decreasing the density with a precise functional form [78, 87]. In practice, a combination of a decreasing density as well as finite roughness of the potential scrambles the reflected wavefronts, leading to dramatically reduced reflections of quasiparticles. Experimentally, it is sufficient to implement a potential of the form

$$V(r) = \begin{cases} 0 & r < R_{\text{trap}} \\ \beta(r - R_{\text{trap}}) & r \geq R_{\text{trap}}, \end{cases} \tag{5.15}$$

where R_{trap} is the radius of the central region where the potential is zero, and β is the linear slope of the potential, which is typically on the order of $\beta \sim 2\pi \times 30\,\text{Hz}/\mu\text{m}$.

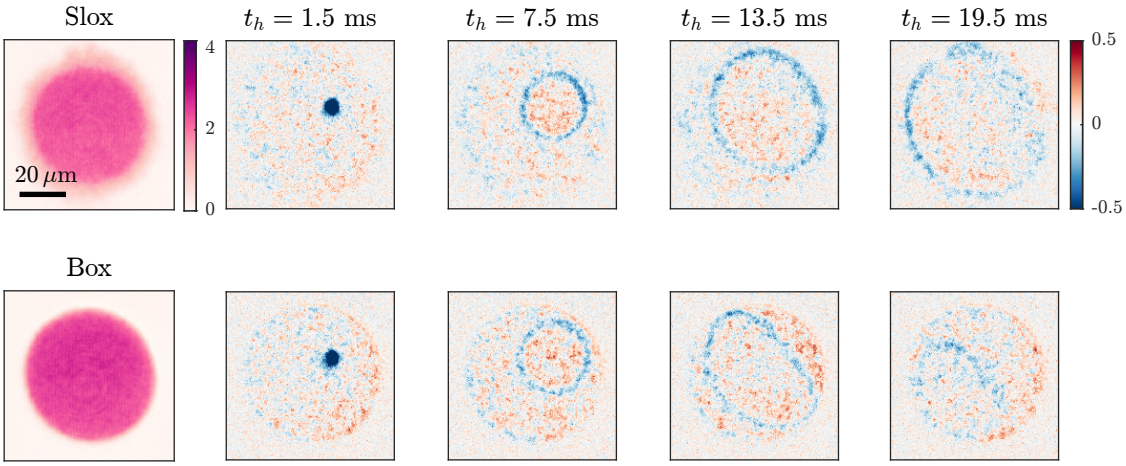

Figure 5.7: Wavepacket Propagation in the Slox Potential. The left column shows density distributions of the atoms loaded into the slox potential (top) and the box potential (bottom). The color bar shows atoms per pixel. The tapered edges are visible as gradually decreasing density in the top case. The red and blue plots show density differences of perturbed densities to the unperturbed case. An initial density dip is prepared by locally switching on a blue-detuned potential. While the wavepacket is slowed and absorbed in the slox potential, the box potential shows clean reflections.

Because the potential is similar to that of a box trap but with slanted walls, we will now call this trapping potential the "slox" trap.

5.6.2 Reflections of Wavepackets

One direct demonstration of the mechanism behind the slox potential is wavepacket propagation. Using the DMD, we load atoms into a potential of a given shape, and then slowly ramp up a peak in the potential in a central part of the condensate, creating a local depletion of the density there. We then rapidly switch off this potential peak, leading to the propagation of the underdensity, much like throwing a rock into a lake. Taking images after successive hold times t_h reveals the dynamics of the wavepackets in average density distributions.

Figure 5.7 shows the propagation of such wavepackets in two trapping configurations, a box trap (steep walls) and a slox trap (slanted walls). The density distributions are shown in the left most column, while density difference plots between perturbed and unperturbed clouds are shown in remaining columns. The circular propagation of the wavepackets is identical for the first 7.5 ms, until the wavepacket reaches the boundary. While the edges of the slox slow and absorb the wavefront, the box reflects the wave, and its reflection is seen propagating over the density even at late times.

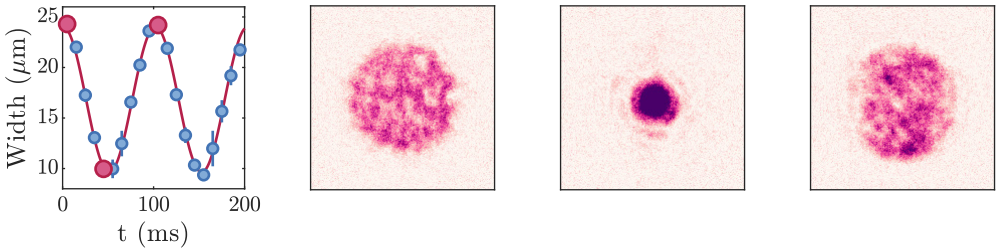

Figure 5.8: Calibration of trap frequency. The left plot shows the width of the cloud after a quench of the scattering length. The breathing mode has double the frequency of the trap, and a value of $\omega_h = 2\pi \times 4.92(4)$Hz is extracted. The three images to the right show the cloud immediately after the quench, at its smallest size, and after a half trap period.

While the measurements shown here are suggestive of reduced reflections at the boundaries, more systematic measurements are discussed in detail in the Master's thesis of Jelte Duchêne [72]. There, it is shown that a combination of slowly decreasing density and roughness of the potential minimizes coherent reflections of wavefronts. Unless stated otherwise, all measurements shown in this thesis are performed in a slox trap.

5.7 Implementation of Momentum Space Measurements

The magnetic field that tunes the interactions using a Feshbach resonance is designed to be homogeneous, but still has a slight curvature due to the Helmholtz coil configuration, on the order of $30\text{nG}/\mu\text{m}^2$. This slight curvature is enough to generate a harmonic trap with a frequency of approximately 5 Hz. Because magnetic fields have the benefit of being very smooth, momentum space measurements are conducted using the finite curvature of the field.

Measurements are performed in the following manner. After a period of some desired dynamics, the interaction strength is ramped down to $0\,a_0$ within 0.5 ms, which is the fastest ramp that the coils and control electronics can cleanly do without an overshoot. Simultaneously, the intensity of the DMD is switched off, and the power of the vertical lattice is decreased by a factor of ~7, leading to a reduction of the trapping frequency ω_z by a factor 2.6. This trap is not switched off entirely in order to confine the atoms in the focal plane of the imaging objective, and the field

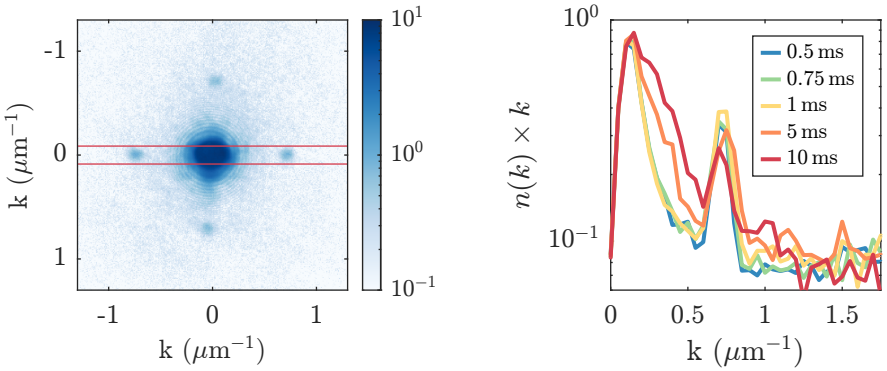

Figure 5.9: Calibration of Momentum Space Ramp. Left, a momentum space distribution after a square lattice density was prepared using the DMD, imaged in momentum space. The colormap shows atoms per pixel on a log scale. The red lines show the region of summation to extract the cuts shown on the right. Right, cuts for different ramp durations of the scattering length from $100a_0$ to $0a_0$ at the beginning of the momentum space measurement. Significant variations in the momentum distribution are apparent only for very slow ramps.

gradient in the z axis is calibrated such that atoms are levitated against gravity; we therefore expect that there are no significant dynamics in the vertical direction. After waiting a quarter period of the harmonic trap, an absorption image of the cloud is taken.

To calibrate the frequency of the magnetic trap, we prepare a condensate, and quench the scattering length from $100\,a_0$ to $0\,a_0$, and observe a breathing mode of the cloud in the harmonic trap. We then fit the width of the cloud throughout the breathing motion, which has the double periodicity of the trap. The results are shown in Fig. 5.8, revealing a trap frequency of $\omega_h = 2\pi \times 4.92(4)$Hz, i.e. $T/4 = 50.8(4)$ms. This number is in good agreement with simulations of the residual curvature of the field due to the coil geometry [88].

Another parameter of concern is the adiabaticity of the ramp of the scattering length, as interactions during the evolution in the harmonic trap will lead to mixing of momentum modes. In order to test the interaction quench, we use the DMD to write a density modulation into the condensate, by projecting a periodic potential onto the otherwise homogeneous condensate (for details, see Chapter 7). This density modulation populates momentum modes at $k \neq 0$, which are then observed as peaks in momentum space. We then perform momentum space measurements, but ramp the scattering length from $100\,a_0$ to $0\,a_0$ over progressively longer periods. The results are shown in Fig. 5.9. No significant effect is visible until a very slow ramp of 10 ms, indicating that for our intents and purposes, the ramp of 0.5 ms is sufficiently fast.

CHAPTER 6

Spontaneous Emergence of Patterns

In this chapter, we describe how patterns emerge in the experiment. First, we discuss the behavior in single shots. Then, the occupations in momentum space are analyzed, showing how structures emerge and decay over time. We then investigate how square lattice patterns form, using statistical observables to capture the geometry of patterns in single realizations. In order to probe the robustness of the pattern formation process, we investigate the effect of different drive frequencies and trapping geometries.

6.1 Single Realizations

To build an intuition about the dynamics of the driven superfluid, it is instructive to first look at single realizations in real and momentum space. Fig 6.1 shows randomly selected single realizations for parameters $r = 0.4$, $\omega_d = 2\pi \times 400\,\mathrm{Hz}$, and $\mu = 2\pi\hbar \times 300\,\mathrm{Hz}$. Real space images are shown in the pink color map, and momentum space images are shown in the blue map on a log scale. Each row shows multiple realizations for a given number of shake periods. [1]

For early times (first row, 7 periods), the real space density is mostly homogeneous with slight ripples appearing, while the momentum space distribution is dominated by the macroscopic occupations in the $k = 0$ mode. Later, density waves at a given length scale become more pronounced, and in momentum space a ring of occupations at the

[1] Distributions in real and momentum space are measured at slightly different times within one period, due to the oscillating contrast and momentum distribution (see Eq. (4.31) and Eq. (4.32)). Thus, measurements in real space are always measured after $n + 0.25$ periods, and after $n + 0.75$ periods in momentum space. The period numbers shown are rounded to the nearest integer for clarity. We note that the pattern formation dynamics typically occur on timescales much longer than one period, and therefore the different times of measurement between real and momentum space are negligible.

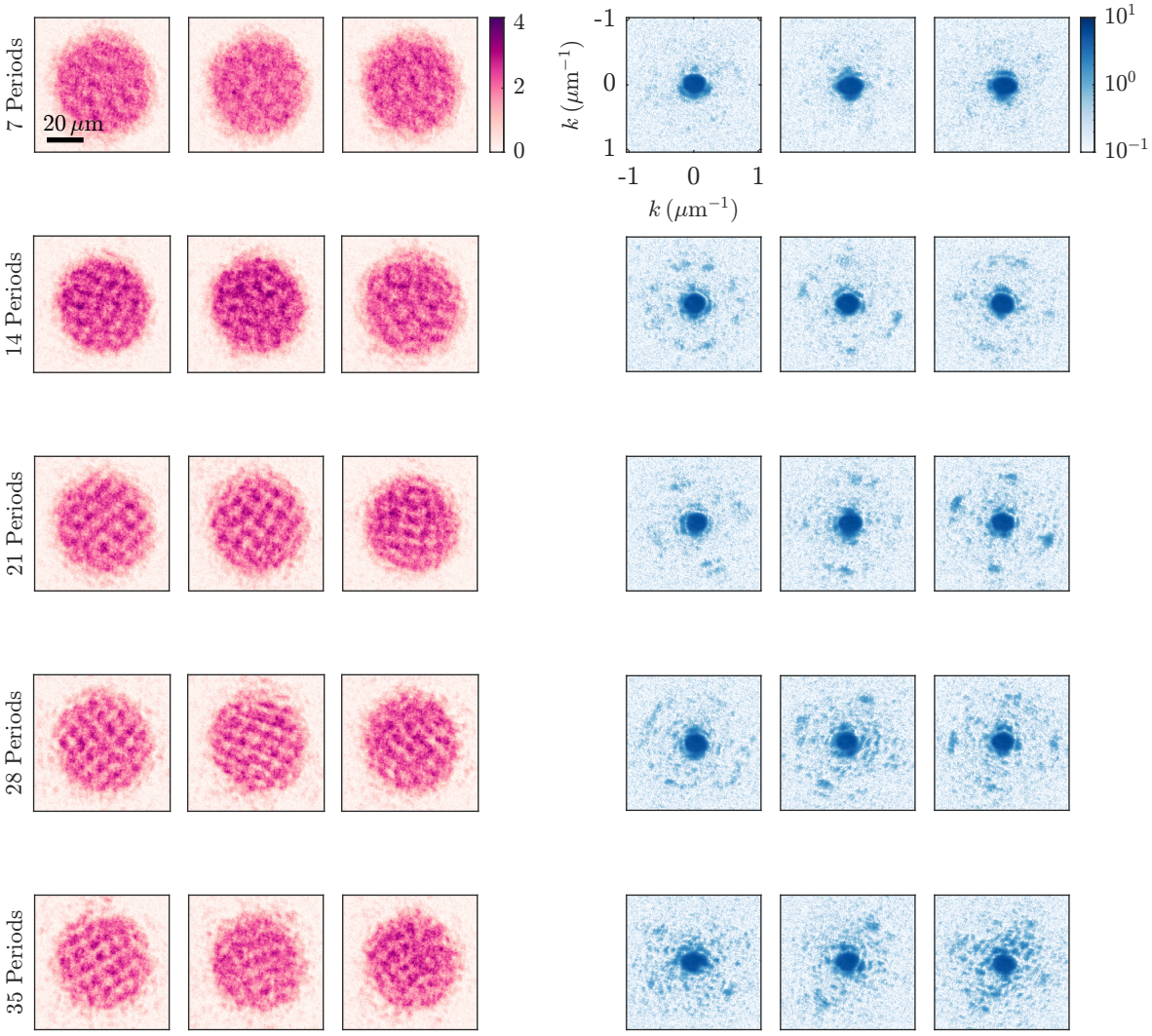

Figure 6.1: Single realizations. Single realizations after various drive periods. Driving with $r = 0.4$, $\omega_d = 2\pi \times 400\,\mathrm{Hz}$, at a chemical potential of $\mu = 2\pi\hbar \times 300\,\mathrm{Hz}$, we take images in real and momentum space. Each row shows three randomly selected realizations in real space (pink) and momentum space (blue). After density waves have grown, one sees square lattice patterns emerging often. These appear as square patterns in real space, and two sets of back-to-back peaks at 90° separation in momentum space. The central, dark peak in the momentum distribution indicates macroscopic occupations of the $k = 0$ mode. Color bars shown are in atoms per pixel, and momentum distributions are shown on a log scale.

resonant momentum becomes clearly elevated. Crucially, each shot shows a different orientation and spatial phase of the pattern, meaning that the structures spontaneously break the translational symmetry of the system, as opposed to being pinned by the boundaries. After roughly 20 periods, the contrast of the density waves no longer grows, and many realizations show the emergence of square patterns, which appear in real space as square lattice density modulations. In momentum space, one sees four peaks along the resonant ring, each separated by roughly 90°. For later times, the contrast in real space is slightly reduced, and structures become more erratic and less ordered. In momentum space, it is apparent that many other modes have become occupied.

These single realizations are indicative of two key features that emerged from the amplitude equation discussed in Chapter 4: saturation of occupations, and the selection of specific lattice geometries. To consider this behavior more quantitatively, we will look at a series of statistical observables to piece apart the pattern formation process.

6.2 Occupations Over Time

We first consider the occupations of momentum modes while driving the scattering length. These dynamics yield insight into the Floquet instability due to the drive, the stabilization in the regime of large occupations, and the eventual decay into disordered structures.

6.2.1 Birth, Life, and Death of Density Waves

To investigate how structures emerge, we look at mean momentum distributions, as shown in Fig. 6.2 for 5, 19, and 39 drive periods. In these plots, the behavior expected from single shots is confirmed: after the drive is switched on, a ring of isotropically occupied momentum modes grows and saturates, until eventually many other modes become occupied. The isotropic nature of the ring indicates that the structure formation process is spontaneous, in that each realization has a random orientation.

Radial distributions of the occupations for many times are plotted in the lower right panel of the figure, with the region around the resonant momentum marked by the vertical gray lines. In the pattern formation framework discussed in Chapter 4, we have assumed that there are occupations only at the critical wavenumber and neglected redistribution effects. In the radial distributions, it becomes evident that at late times, other momentum modes are occupied on the same scale as the critical momentum. The increase in occupations of other momentum modes means that

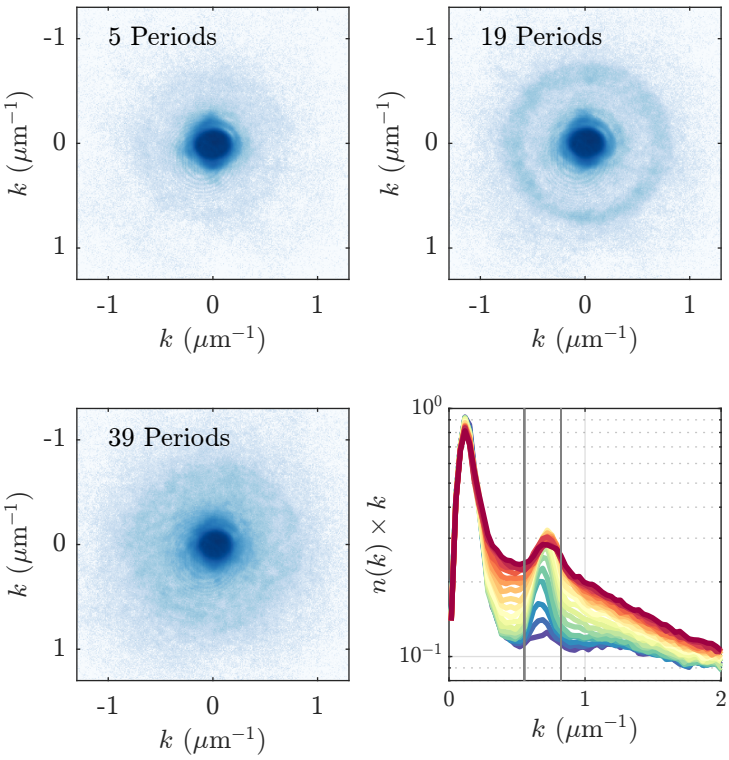

Figure 6.2: Birth, Life, and Death of Patterns. Momentum distributions at three times, showing the emergence of a single, isotropic ring of atoms at the resonant wavenumber k_c. For later times, many other modes have been occupied. The bottom right shows radial distributions for many times. The vertical lines, centered around $k_c = 0.68\mu\text{m}^{-1}$, show the region used to extract mode occupations in later analyses.

at late times the theoretical description breaks down, as modes with $|\mathbf{k}|$ no longer dominate the dynamics.

6.2.2 Growth Rates

We will now focus our attention on the region around k_c, performing quantitative analyses on the occupations in the region shown in the bottom right panel of Fig. 6.2.

At early times, dynamics are well described by the linear instability analysis performed in Section 4.1. In this analysis, we found that a finite drive amplitude $r > 0$ leads to the exponential growth of occupations at a critical length scale. In the presence of damping, the drive amplitude must be above some finite value for growth to occur, and above the threshold, occupations in momentum space grow as [18, 47]

$$N(k_c, t) = N_0(k_c) e^{2(\alpha - \Gamma)t}, \tag{6.1}$$

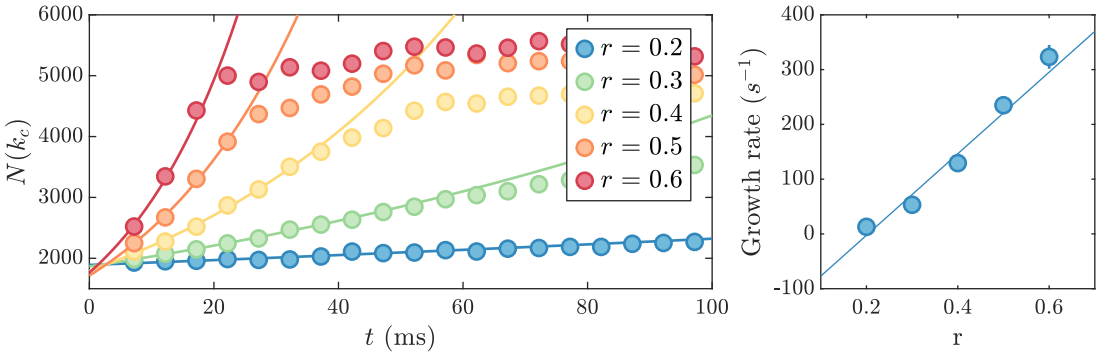

Figure 6.3: Amplitude Dependence of Growth Rate. Left panel, occupations over time for various drive amplitudes, $r = 0.2, 0.3, 0.4, 0.5$, and 0.6, from blue to red. The initial growth rate is extracted before occupations saturate using an exponential fit (solid line). Right panel, the extracted growth rates with a linear fit.

where $\alpha = r\frac{\mu\epsilon}{2E}$, and Γ is a phenomenological damping term, which must be determined experimentally. By measuring the growth of occupations at the critical length scale for different drive amplitudes r, we can extract growth rates and therefore determine Γ.

Experimental results for various drive amplitudes but otherwise identical parameters as in the previous section are shown in Fig. 6.3. We vary the drive amplitude from $r = 0.1$ (blue points) to 0.6 (red points), and extract the occupations on the resonant momentum ring, in a bin of width $\Delta k = 0.27\mu\text{m}^{-1}$. We then fit an exponential to the times in which the occupations are rising, before showing signs of saturating. The extracted growth rates are shown in the right panel of the figure. One neatly recovers the linear behavior of the growth rate, and, using a linear fit, we extract the critical driving amplitude r_c. With this, we can extract the damping rate $\Gamma = 65 \pm 10s^{-1}$, and can compare the growth rate α for a given r to the theory value. At $r = 0.4$, we find $\alpha_{\text{exp}} = 130 \pm 15s^{-1}$, in good agreement with the theory value of $113s^{-1}$.

6.2.3 Saturation of Occupations

As can be seen clearly in Fig. 6.3, occupations at the critical length scale saturate after a number of drive periods, with the saturation occupation n_{sat} dependent on the drive amplitude. This behavior is nontrivial, as even for small drive amplitudes nonlinearities must play a role in dynamics and lead to saturation. The saturation

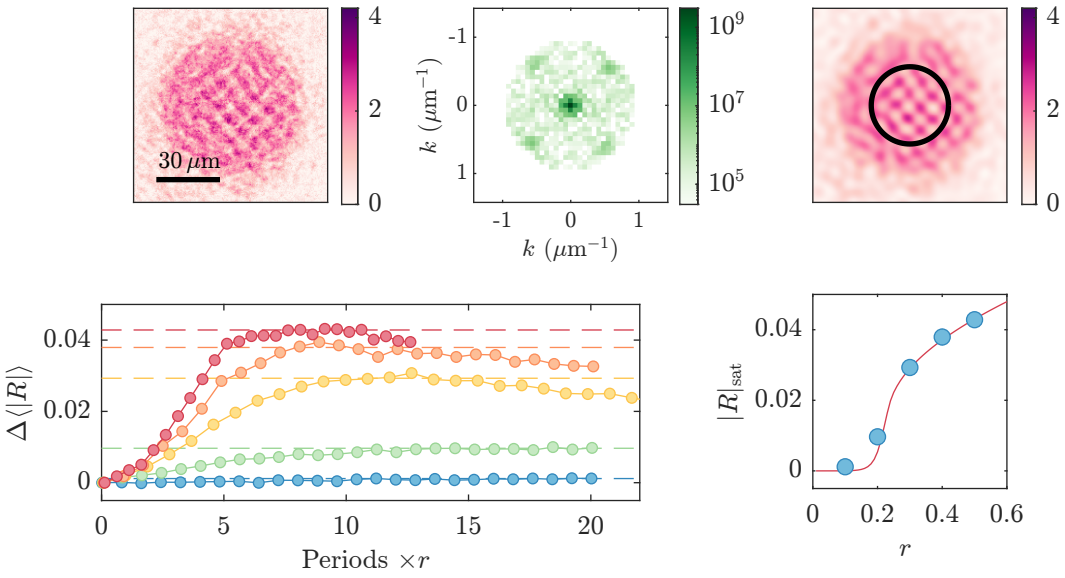

Figure 6.4: Saturation of Contrast. The top row shows the three steps in the analysis used to extract the mean contrast. Single shots (left) are Fourier transformed and filtered with a step function up to just above the critical wavenumber (center). These images are then transformed back into real space (right), and the RMS of a central region is analyzed. The bottom left panel shows the change in the mean values $\langle|R|\rangle$ over time for five drive amplitudes. The time axis is scaled with the drive amplitude to better compare the five cases. The bottom right shows the extracted values for $|R|_{\mathrm{sat}}$, compared to numerical solutions of the extended AE.

of occupations is given by the amplitude equation, which predicts that the square contrast of the standing wave scales roughly linearly with the drive amplitude (see Section 4.3.3),

$$|R_{\mathrm{sat}}|^2 \propto \frac{\alpha}{\lambda}\sqrt{1-\frac{\Gamma^2}{\alpha^2}}. \tag{6.2}$$

As the damping and growth rates have already been extracted, we can therefore use the saturated contrast to extract the value for λ.

To see how the saturated pattern contrast $|R_{\mathrm{sat}}|$ scales with the drive amplitude, we will perform measurements in real space, because the value of $|R|$ can be directly extracted using the contrast of the standing wave,

$$n(x) = \bar{n}\left(1 + 4|R|\cos\left[\frac{\omega_d}{2}t + \varphi\right]\cos kx + \text{h.o.t.}\right). \tag{6.3}$$

While a similar measurement can also be performed in momentum space [50], for late times coherent and incoherent occupations cannot be clearly separated in stroboscopic

measurements. We therefore extract the evolution of the pattern contrast in real space to determine λ.

An overview of the experimental results is shown in Fig. 6.4. We measure density distributions after various drive periods for five drive amplitudes, using longer times for low r and shorter times for high r, to account for differing timescales. The contrast is quantified in the following manner: first, the density distributions are filtered in momentum space, by Fourier transforming them, and setting a cutoff wavenumber above which every pixel of the Fourier transform is set to zero. As can be seen in the central panel of the top row in Fig. 6.4, $k_c = 0.8\mu\mathrm{m}^{-1}$, and $k_{\mathrm{cut}} = 0.94\mu\mathrm{m}^{-1}$. The image is then transformed back into real space (upper right panel), and a central region is analyzed, shown as the black ring in the figure. In this region, the mean magnitude of R is determined as

$$\langle |R| \rangle = \frac{\sqrt{2}}{4} \sqrt{\left\langle \left[\frac{n(\mathbf{r})}{\bar{n}} - 1 \right]^2 \right\rangle_{\mathbf{r}}}, \tag{6.4}$$

where $\bar{n}$ is the mean density, and the subscript $\mathbf{r}$ indicates the average over all positions in the cloud. This is the root mean square of the density, with the factor $\sqrt{2}$ to properly calculate the amplitude of a sine wave, and the factor 4 to account for the definition of $|R|$ in Eq. (6.3).

The change in contrast over time is shown in the lower left panel of Fig. 6.4 for different drive amplitudes, and the saturated value is extracted by taking the mean of the five maximal points. In the lower right subplot, these extracted amplitudes are compared to numerical solutions of the extended amplitude equation. For the numerical solution, identical parameters to the experiment are used, with $\Gamma = 65s^{-1}$. An effective value for λ is fitted by eye, $\lambda_{\mathrm{eff}} \sim 9\lambda$, where λ is the theory value.

The functional form of $\langle |R| \rangle$ over the drive amplitudes shows excellent agreement to the numerical simulations, and the large value of λ_{eff} compared to the theory value simply scales the function to lower contrasts. There are a variety of possible reasons for the discrepancy between the effective and theoretical values. The theoretical model contains only a phenomenological damping parameter, and does not account for amplitude-dependent effects or heating. Additionally, the model assumes an infinitely extended system, which is certainly not true for the standing waves observed here. Finally, this analysis may underestimate the saturated amplitude, as it uses the mean contrast over the whole cloud as opposed to the amplitude of single stripes. The precise value of λ does not affect the conclusions drawn in this work, and is merely used to scale theoretical predictions to experimental observations.

6.3 Emergence of Spatial Correlations

So far, we have discussed characteristics of the mean occupations but have neglected the spatial structure or orientations of the density waves. As was already observed in the single shots shown in Fig. 6.1, square lattices seem to emerge astonishingly often. This is indicative of some coupling of density waves, as was theoretically motivated in Chapter 4. Because the patterns emerge spontaneously and have random orientations in each realization, we cannot perform analyses on mean densities. We will therefore now use a series of statistical observables that quantify the geometry of patterns in single shots, to gain information on the emergence of square lattices.

6.3.1 Quantification of Spatial Structure

In order to show that the square lattices emerge systematically, we define a $g^{(2)}$ correlation function in momentum space:

$$g^{(2)}_{k_c}(\delta\theta) = \left\langle \frac{\langle n(k_c,\theta)\, n(k_c,\theta+\delta\theta)\rangle_\theta}{\langle n(k_c,\theta)\rangle^2_\theta} - 1 \right\rangle . \tag{6.5}$$

Here, $n(k_c,\theta)$ is the momentum space density in the resonant ring as a function of the azimuthal angle θ, and $\delta\theta$ is the difference in angle between two points along the ring. The subscript θ means that all values on the ring are averaged, and the brackets of the whole equation indicates averaging over many single realizations.

By calculating the correlator for each realization and then averaging, we can recover information about the structure of single shots that is otherwise lost in mean densities. In other words, this function quantifies fluctuations on the resonant ring, where positive values indicate a higher signal relative to the squared mean, and negative values mean lower signal relative to the squared mean.

The procedure for calculating the correlation is as follows. Many measurements of the momentum distribution are averaged, and the resonant wavenumber is determined. A region around this wavenumber with width $\Delta k = 0.27\mu\mathrm{m}^{-1}$ is then binned azimuthally, with bin widths of $\pi/16$. The correlator is calculated for single shots and then averaged over all realizations.

The resulting $g^{(2)}_{k_c}(\delta\theta)$ at various drive periods is shown in Fig. 6.5. Though initially the correlator is flat except for the auto-correlation at $\delta\theta = 0$, after a few periods a peak at $\delta\theta = \pi$ emerges, which is of similar magnitude to the auto-correlation peak. This indicates that occupations in momentum space are back-to-back correlated, a result of the momentum-conserving pair-production process. At later times, positive correlations at $\delta\theta = \pi/2$ and anti-correlations at $\pi/4$ emerge, showing that the signal is enhanced relative to the mean at $\pi/2$ and suppressed at $\pi/4$. The suppression of correlations at $\delta\theta = \pi/4$ and $3\pi/4$ is indicative that the presence of square lattices

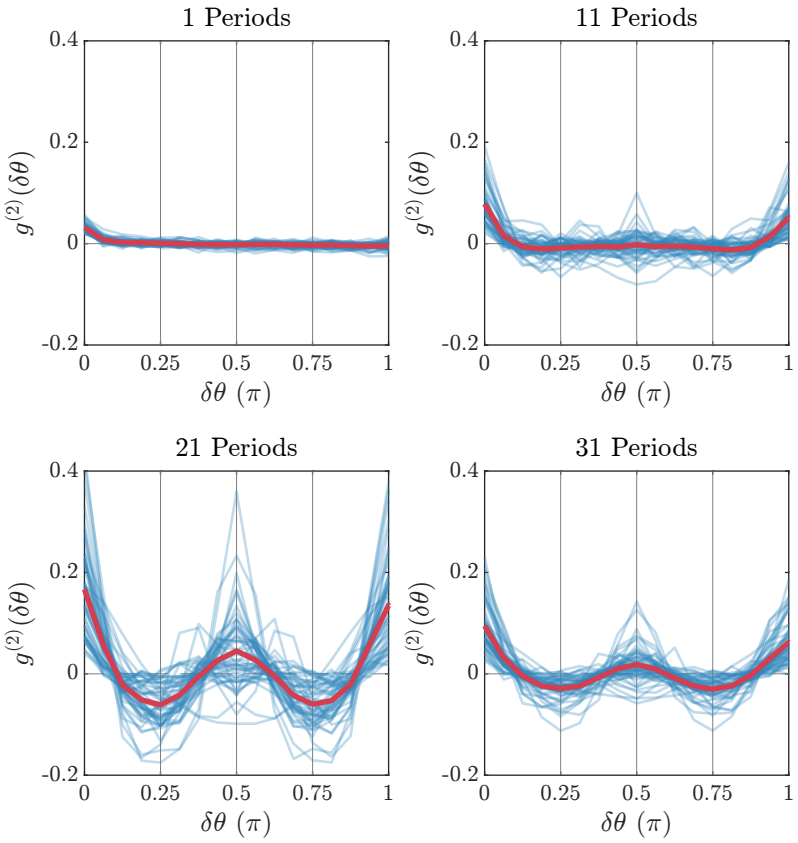

Figure 6.5: Angle Correlations. Correlations of occupations at k_c as a function of the angle between them, $\delta\theta$. The blue lines are the correlations for single shots, whereas the red line is the average. At 11 periods, enhanced correlations at $\delta\theta = \pi$ indicate the emergence of stripes. At all other angles, single shots fluctuate symmetrically around zero, showing no orientation of the stripes. At later times, a cowboy-hat shape emerges, indicative of square lattices. Even after many drive periods, the shape is still apparent, but correlations at all angles are diminished due to a rising background of incoherent occupations.

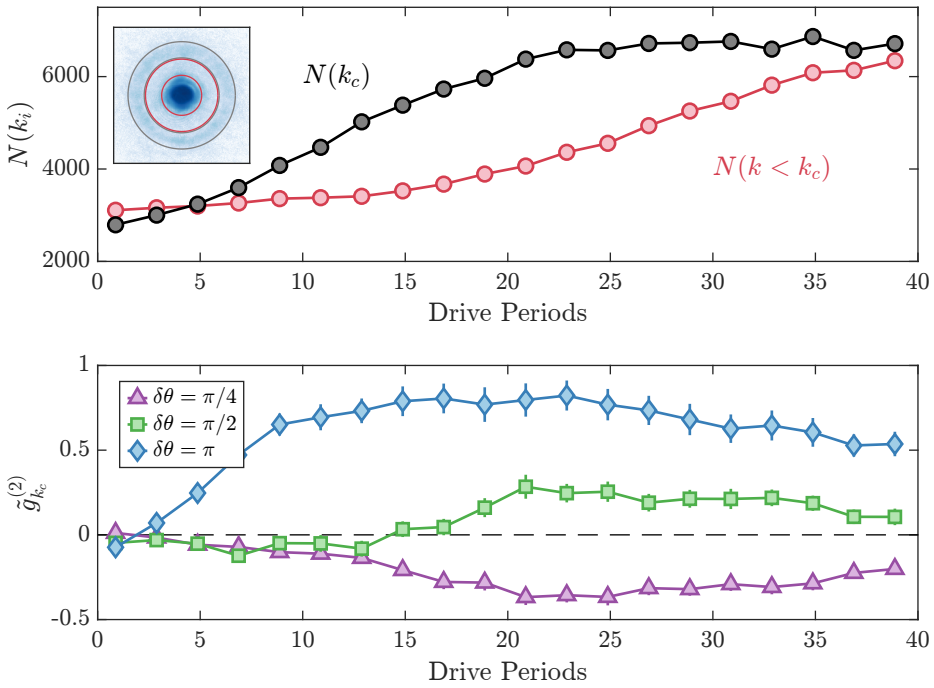

Figure 6.6: Comparing Occupation and Correlation Growth. Top row, the occupations in momentum space at k_c (black), and in an adjacent region of lower momentum (red). The inset shows an average momentum distribution, with the regions used to extract occupations shown in red and gray. Below, the normalized correlation values $\tilde{g}^{(2)}_{k_c}(\delta\theta)$ for the same data. Around the point when occupations begin to saturate, the correlations at $\delta\theta = \pi/2$ and $\pi/4$ split around zero, indicating the emergence of square lattices. For late times, all correlation values decrease symmetrically. Correlations are calculated in the gray region.

inhibits occupations at other momenta; if many square lattices at different orientations were superimposed, it would result in elevated correlations at $\pi/2$ without adjacent minima. For late times, the cowboy-hat shape of the correlations remains but has a decreased contrast at all angles.

6.3.2 Time Dependence of Correlations

In order to track the emergence of the patterns more quantitatively, we define a normalized correlation value

$$\tilde{g}^{(2)}_{k_c}(\delta\theta) = g^{(2)}_{k_c}(\delta\theta)/g^{(2)}_{k_c}(0). \tag{6.6}$$

Although in principle the auto-correlation $g^{(2)}_{k_c}(\delta\theta)$ should be independent of the absolute occupations on the ring and such a normalization is trivial, in the presence of a finite noise background, the absolute value of $g^{(2)}_{k_c}(\delta\theta)$ depends on both the distribution of momentum modes, as well as their amplitude relative to this noise background. In the experiment, the presence of incoherent thermal atoms makes such a normalization useful for discerning trends of only structure formation. This normalized correlation value is equal to 1 if the occupations are equal in all bins if rotated by $\delta\theta$.

Figure 6.6 shows the time dependence of both occupations in momentum space (top row) and normalized correlation values for $\delta\theta = 45^{\text{o}}$, 90^{o}, and 180^{o} (bottom row). Occupations in momentum space are calculated by summing over a region of width $\delta k = 0.27\mu\text{m}^{-1}$ around k_c (black, region as shown in Fig. 6.2), as well as an adjacent region at lower momentum, centered around $k = 0.44\mu\text{m}^{-1}$. One again sees the exponential growth at early times followed by the saturation of occupations, as discussed previously. The red points show that redistribution to lower momenta begins to increase significantly when occupations at the resonant momentum become saturated.

The values of $\tilde{g}^{(2)}_{k_c}(\delta\theta)$ show that correlations at $\delta\theta = 180^{\text{o}}$ (blue diamonds) quickly rise at early times, and then stay roughly constant at just under 1. This increase is likely an artifact due to the emergence of the momentum peaks relative to the noise, as we expect that quasiparticle pairs are back-to-back correlated as soon as they are produced. The correlations corresponding to the emergence of square lattices ($\delta\theta = 90^{\text{o}}$ and 45^{o}) are initially 0, and split symmetrically around 0 at the time where occupations become saturated. This supports that patterns are indeed a nonlinear phenomenon; at early times random stripes are dominant, and only in the regime of large occupations do the square lattices develop. At late times when occupations in the off-resonant modes are comparable to those at k_c, the correlations at all angles decrease symmetrically.

6.4 Scaling of Parameters

In order to get a sense for how the emergence of patterns scales with experimental parameters, we perform a similar analysis on patterns for different drive amplitudes. The results are summarized in Fig. 6.7. Values for $\tilde{g}^{(2)}_{k_c}(\delta\theta)$ are plotted against drive periods in the left column, where the top panel shows back-to-back correlations and the bottom the square-lattice correlations. The back-to-back correlations grow almost identically in each case, with a significant delay for the smallest driving amplitude $r = 0.3$. Interestingly, the decay of back-to-back correlations scales with the drive amplitude, indicating that there are amplitude-dependent effects that limit the lifetime

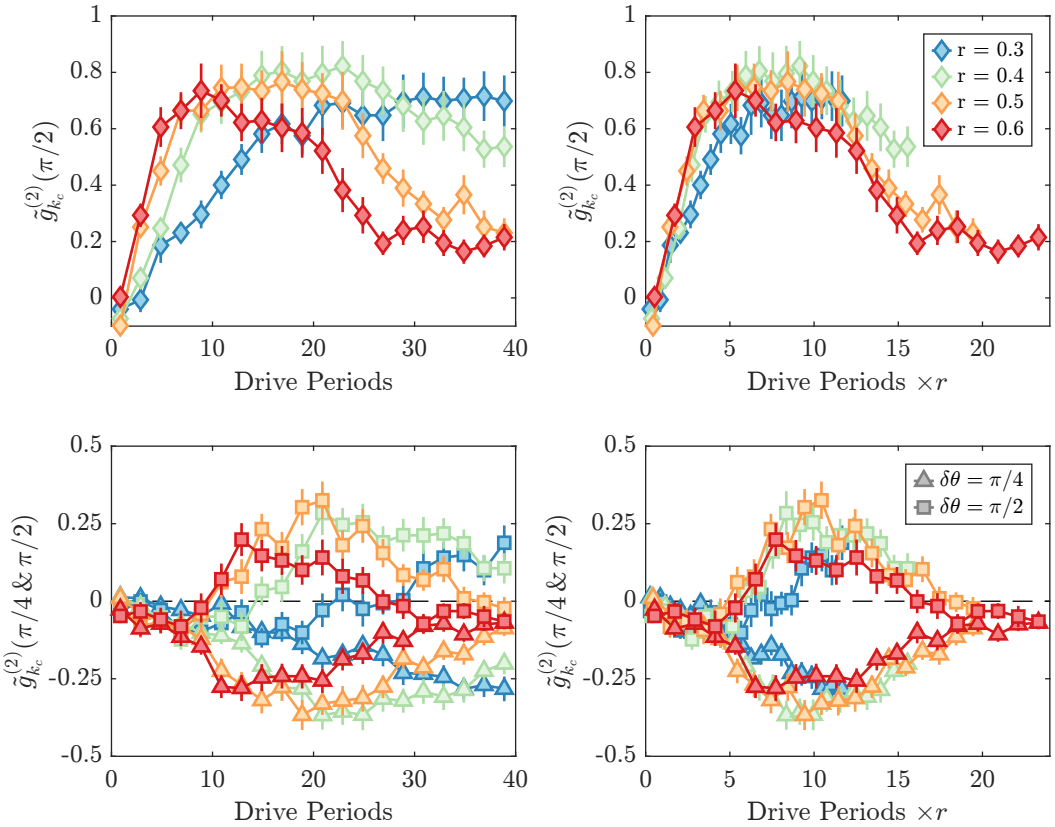

Figure 6.7: Scaling of Parameters. The normalized correlation values are plotted for $\delta\theta = \pi$ in the top row, and for $\delta\theta = \pi/2$ and $\pi/4$ in the bottom row. Each color indicates a different drive amplitude. The left column shows the data with a true time axis, whereas the right column's time axis is multiplied by the drive amplitude. The collapse of the scaled curves onto one generic shape indicates that the qualitative behavior is identical in each case.

of correlations. The square-lattice correlations emerge later and later in time, further supporting a genuine dependence on the occupations on the occupations in the ring.

The dependence on the amplitude is elucidated by scaling the drive time with the amplitude, $r \times t$, shown in the right column. The direct correlation of the decay of back-to-back correlations now becomes clear, as all curves in the top right plot collapse onto one universal functional form. Similarly, the square lattice correlations collapse onto one universal curve, showing an initial phase where stripes dominate, followed by the splitting of correlations at $\delta\theta = \pi/4$ and $\pi/2$. For the lowest drive amplitude, it appears that time scales are so slow (i.e. the growth rate is so close to the damping rate) that the values cannot be properly scaled. For the largest drive amplitude, on the other hand, the square lattice correlations are not as pronounced

as for lower drive strengths, and the back-to-back correlations are also systematically reduced.

These results indicate that regardless of the drive amplitude, the phenomenological behavior of the patterns is the same. This means that working at lower drive amplitudes extends the lifetime of patterns without affecting other qualitative characteristics.

6.5 Frequency Dependence

As was discussed theoretically in Section 4.1, periodically modulating the scattering length results in bands of unstable momentum modes. While the width of these bands is given by the drive amplitude, the central wavenumber of the primary unstable mode is determined by the chemical potential and the drive frequency. This relation is given by

$$\hbar\omega_d/2 = \sqrt{\epsilon(\epsilon + 2\mu)}. \tag{6.7}$$

Here, $\epsilon = \frac{\hbar^2 k_c^2}{2m}$ is the kinetic energy of the critical wavenumber, k_c. The factor $1/2$ on the LHS results from the pairwise creation of quasiparticles, and the RHS is simply the Bogoliubov dispersion relation.

Experimentally, we can tune the drive frequency to values on the order of around 1 kHz. The chemical potential is given by the product of the density and the interaction strength, which can both be tuned over a large range. At low chemical potentials, the density distribution is strongly affected by the residual curvature of the external magnetic field and roughness of the dipole traps, while at large chemical potentials the condensate is affected by strong three-body atom loss. We therefore typically use values around $\mu \in 2\pi\hbar \times [200, 400]$ Hz.

A systematic measurement of the frequency dependence of patterns is performed in real space, and we use the Fourier transform of the density contrast to quantify structure emergence,

$$\delta n_k = \langle |\mathcal{F}(\delta n(\mathbf{r}))|^2 \rangle / MTF(\mathbf{k}), \tag{6.8}$$

where $\delta n(\mathbf{r}) = n(\mathbf{r})/\bar{n}(\mathbf{r}) - 1$, and $MTF(\mathbf{k})$ is a modulation transfer function that accounts for k-dependent imaging resolution [89, 90].

The top row of Fig. 6.8 shows δn_k for three drive frequencies, $\omega_d = 2\pi \times 200, 600, 1000$ Hz, after 12.75 drive periods. As previously, a ring of occupied momenta is apparent, and the ring's position moves to larger wavenumbers with higher drive frequency. In the lower left panel, radial averages of the occupations in momentum space are shown for frequencies between 200 (blue) and 1000 (red) Hz, in 200 Hz steps. Extracting the peak positions of the excited band of momenta

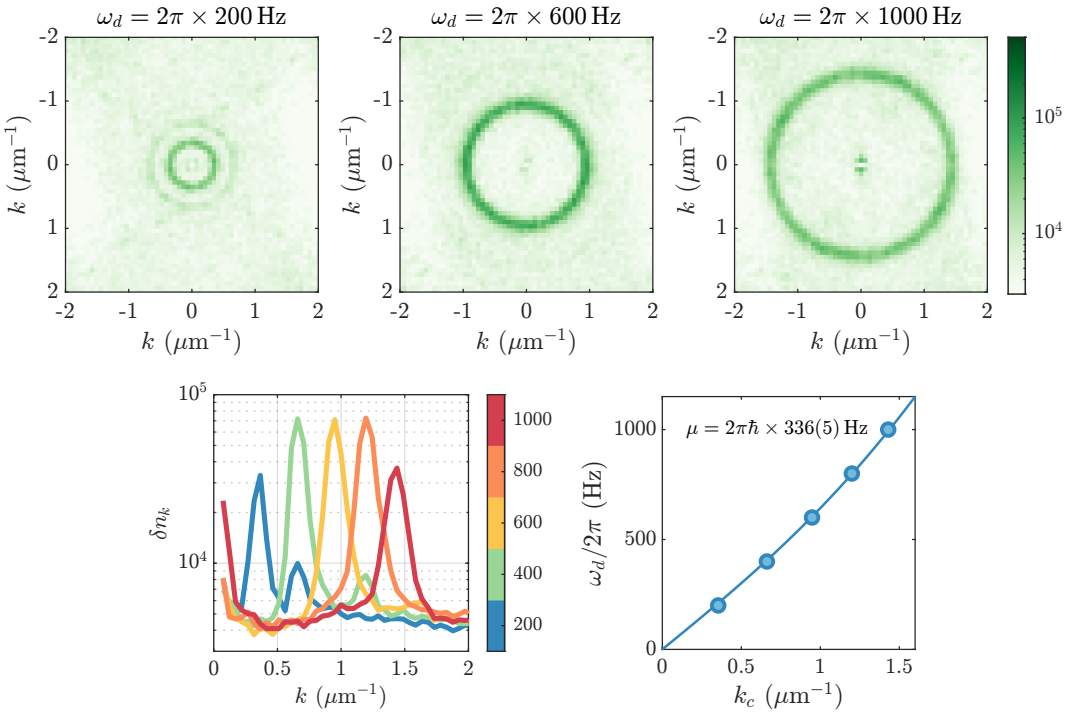

Figure 6.8: Frequency Dependence of Drive Frequency. Top row, mean Fourier transforms of densities after 12 drive periods for three drive frequencies, averaged over approximately 40 single realizations. The resonant ring shifts outward for higher drive frequency, but remains radially symmetric. Bottom row, left panel shows radial cuts of many frequencies, while the right panel shows the extracted peak positions vs. frequency. The solid line is a fit using $\omega_d = 2 \times E(k_c)$, with $E(k)$ the Bogoliubov dispersion relation parameterized by μ.

and plotting this against drive frequency (lower right), we recover the functional form $\omega_d = 2 \times E(k_c)$, using the chemical potential as a fitting parameter. In this measurement $\mu = 2\pi\hbar \times 336(5)\,\mathrm{Hz}$. This value is consistent with measurements using wavepacket propagation to determine the speed of sound, which is related to the chemical potential through $\mu = mc_s^2$.

Regarding the emergence of square lattices, we can define a similar $g^{(2)}_{k_c}(\delta\theta)$ correlation function, now using δn_k instead of the momentum distribution. Because the Fourier transform is symmetric in $\pm k$ by definition, this correlation function only yields unique information in the region $0 \leq \delta\theta \leq \pi/2$. The bin width in $\delta\theta$ is adjusted to the value of k_c.

Density distributions from four single shots at different frequencies are shown on the left half of Fig. 6.9, with $g^{(2)}_{k_c}(\delta\theta)$ plotted on the right. At $\omega_d = 2\pi \times 200\,\mathrm{Hz}$, the

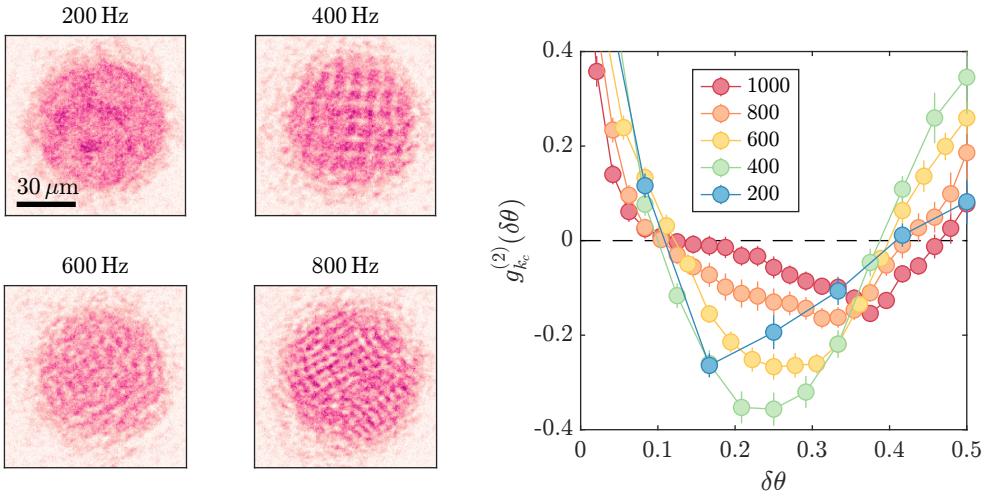

Figure 6.9: Patterns at Different Frequencies. Left, four single realizations at different drive frequencies. Right, $g^{(2)}_{k_c}(\delta\theta)$ correlation functions for the four cases. Each curve shows enhanced correlations at $\pi/2$, indicating the robustness of the emergence of square lattices.

structures are of the same order as the system size, with roughly two wavelengths apparent. The correlations (blue) still show the characteristic shape of anti-correlations at $\delta\theta \sim \pi/4$, with slightly elevated correlations at $\pi/2$, indicating that square lattices do tend to emerge.

At higher frequencies, the pattern wavelength is much smaller than the system size, and patches of patterns with different orientations are apparent (see density for 800 Hz). The presence of many patches affects the the shape of $g^{(2)}_{k_c}(\delta\theta)$, as a more homogeneous distribution throughout the resonant momentum ring results in reduced anti-correlations. Nevertheless, it is apparent that square lattices do emerge at large frequencies, as evidenced by the positive correlations at $\pi/2$ for all length scales, with a minimum that shifts to larger values of $\delta\theta$.

These results confirm the robustness of the pattern formation process to changes in the drive frequency. In particular, none of the $g^{(2)}_{k_c}(\delta\theta)$ functions show enhanced correlations at the critical angle θ_{crit}, which for these parameters ranges from $\delta\theta = 0.15\,\pi$ to $0.4\,\pi$. Having investigated the role of drive duration, amplitude, and frequency in the pattern formation process, we now turn to the final critical feature of the experiment, namely the boundary conditions.

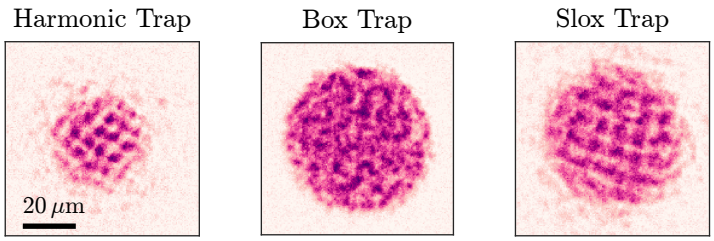

Figure 6.10: Pattern Dependence on Trap Geometry. Left panel, a single shot of a pattern in a harmonic trap. Center, a box trap, with seemingly disordered density structures. Right, the slox trap, showing square lattices as discussed until this point.

6.6 Effect of Boundary Conditions

As is generally the case in pattern formation, the spontaneous emergence of specific structures is critically affected by the boundaries of experiments. For example, in pattern formation experiments using classical fluids such as water, the meniscus at the edge of the system can result in additional excitations emanating from the boundary [2, 14].

In BECs, the geometry of the cloud is determined by the trapping potential in the Thomas-Fermi limit. The most experimentally accessible trapping geometry is a harmonic confinement, $V(r) = \frac{1}{2}m\omega_{\mathrm{ho}}r^2$, as this can be approximately realized with a single, red-detuned laser beam with a Gaussian profile. Historically, this was the trapping geometry originally implemented in the experiment. After performing preliminary experiments periodically driving the scattering length, we observed that in many single shots square lattices emerged, as can be seen in the left panel of Fig. 6.10. Later, the DMD was implemented, and the experiments were repeated using homogeneous clouds with a hard wall (box trap). Here, the patterns no longer seemed structured, but rather displayed significant disorder, as can be seen in the center panel. Adjusting the boundaries to be slightly slanted (the slox trap, right panel), patterns emerged, showing stable occupations. In the following, we will present a number of measurements highlighting the effects of boundary conditions on pattern growth and stability.

6.6.1 Occupations

The boundary conditions strongly influence the dynamics of the mode occupations. Figure 6.11 shows the growth of occupations at the resonant momentum (black points) as well as an adjacent region at lower momentum (red points) for harmonic, box, and slox traps. The experimental parameters for the measurements in the box and slox

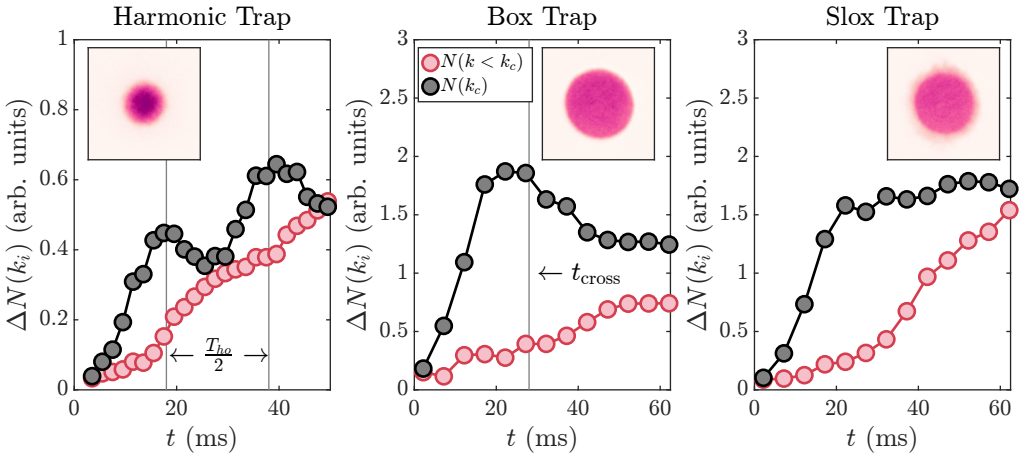

Figure 6.11: Effect Boundary Conditions on Occupations. Left panel, occupations at k_c in a harmonic trap (black) and an adjacent region at $k < k_c$. The inset shows a mean density distribution in real space. The vertical lines indicate half of the trap period, determined with an independent measurement. Center, occupations in the box, where the vertical line indicates the crossing time. Right, occupations in a slox trap. Occupations in the box and slox can be quantitatively compared, but only qualitatively to the harmonic trap due to significantly different experimental parameters.

traps shown here use $r = 0.6$, but are otherwise identical to those used in Section 6.2.2. For the harmonic trap, $r = 1.0$, $\omega_d = 2\pi \times 500\,\text{Hz}$, and $k_c = 1.1\mu\text{m}^{-1}$.

In each case, the occupations at the resonant momentum mode grow exponentially for early times. In the harmonic trap, after an initial period of growth, the occupations begin to oscillate at twice the harmonic trap frequency ($\omega_{\text{ho}} = 2\pi \times 20\,\text{Hz}$), which was determined using an independent measurement. This is because the harmonic trap constantly mixes space and momentum, meaning that quasiparticles that are initially produced at k_c begin to propagate in space, at the cost of their kinetic energy. Because the momentum space measurement is an instantaneous measurement of the kinetic energy, this is observed in the occupations at k_c. Interestingly, out-of-phase oscillations at lower momenta can be seen in the red dots. Therefore, though the harmonic trap's boundary conditions leads to clear patterns, its mixing of space and momentum makes it a suboptimal tool for studying pattern stability.

The box trap, on the other hand, shows an initial increase in occupations, which are then damped, reaching a steady state at a lower value. The time of the decrease in occupations corresponds to the crossing time in the system (vertical line in the central panel), defined as $t_{\text{cross}} = 2R_{\text{trap}}/v_g$, where v_g is the group velocity at k_c, which for these parameters is $2.0\,\mu\text{m/ms}$. This is indicative of the role of reflections at the boundaries, as this is the timescale in which patterns will have spread throughout the

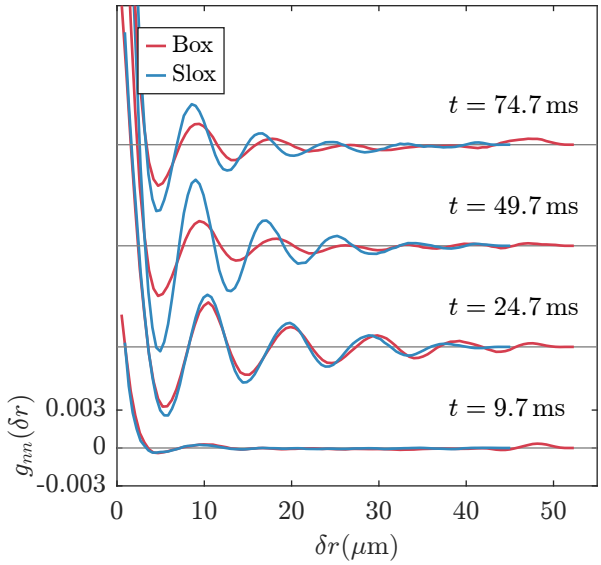

Figure 6.12: Density-Density Correlations. Correlations for four different periods, comparing box and slox traps. Each time is offset by a constant value for clarity. Positive correlations for large separations in the box trap indicate enhanced boundary effects.

system and been reflected. In the slox trap, occupations grow and then saturate at a relatively constant level[2]. In both cases, the off-resonant occupations grow after the occupations at the resonant momentum have either saturated or are damped, though these occupations grow to much larger values in the slox case.

6.6.2 Density-Density Correlations

In order to investigate the differences in the growth of patterns in the box and slox, we now consider the density-density correlation function, defined as

$$g_{nn}(|\delta\mathbf{r}|) = \left\langle \delta n(\mathbf{r}) \delta n(\mathbf{r} + \delta\mathbf{r}) \right\rangle, \tag{6.9}$$

where $\delta n(\mathbf{r}) = n(\mathbf{r})/\bar{n}(\mathbf{r}) - 1$ is the density contrast of a single shot relative to the mean. The averaging brackets in the correlation indicate the averaging over many shots. This correlator gives a measure of density fluctuations that is dependent on radially-symmetric displacements, and is evaluated roughly in the region where $V(\mathbf{r}) = 0$ (i.e. where the density is constant).

The density-density correlators are shown in Fig. 6.12, compared for four drive periods in the box and slox case, in red and blue, respectively. At short ranges,

[2]This is the same data as that presented in Fig. 6.3 for $r = 0.6$.

the emergence of one periodicity is clearly visible in the oscillatory behavior of the correlation, with slightly different wavelengths in the two cases owing to the different mean densities of the two trapping potentials. At roughly the time when occupations in momentum space are maximal (as shown in Fig. 6.11), patterns are correlated throughout the entire system. The contrast of the correlations is similar for the two cases initially, but at later times the box trap shows significantly reduced contrast.

Perhaps the most significant difference between the two cases is the dynamics at large displacements. While the slox correlations smoothly approach zero, the box shows positive correlations at approximately the trap diameter, indicating that collective modes of the trap are excited, or that the boundary condition has pinned specific spatial phases of patterns. This feature is persistent over many periods, and the continued influence of the boundaries will certainly have an effect on the emergence of the square patterns.

6.6.3 Pattern Emergence

Finally, we can look at the pattern correlation functions, $g^{(2)}_{k_c}(\delta\theta)$, to see if square lattices do emerge in the box, despite the apparent randomness of patterns in real space. The top row of Fig. 6.13 shows $g^{(2)}_{k_c}(\delta\theta)$ for the box and slox trap, in red and blue, respectively. While after 10 periods the two cases are roughly identical, a short time later the correlations are damped in the box trap. Extracting the values of $\tilde{g}^{(2)}_{k_c}(\delta\theta)$ for $\delta\theta = \pi/4$ and $\pi/2$ (bottom panel), it is apparent that while square lattices are stable in the slox trap, they are damped in the box trap.

The lack of stable square lattices in traps with hard walls is remarkably reproducible, and we have not observed any dependence on trap size or even geometry including a square shape. Though naively one could expect that a square box is a convenient trap shape to observe square lattices, the spontaneous nature of the pattern formation makes this untrue. Other than in the special cases of 0^o and 45^o orientations to the square trap, reflections of density waves will not be commensurate with the original pattern, which is detrimental to the stability of single square lattices.

A number of further measurements not shown here were performed to investigate the mechanism that leads to the differing behavior in the box and slox traps, detailed in [72]. First, it was shown that the emergence of patterns can be smoothly suppressed by increasing the steepness of the slox potential. Furthermore, smoothening the potential with an iterative optimization algorithm to remove any imperfections [91] also leads to the reduction of square-lattice correlations, indicating that the finite roughness of the slox contributes to its effect. These measurements support the notion that the suppression of reflections at the boundary of the trap play a significant role in pattern stability.

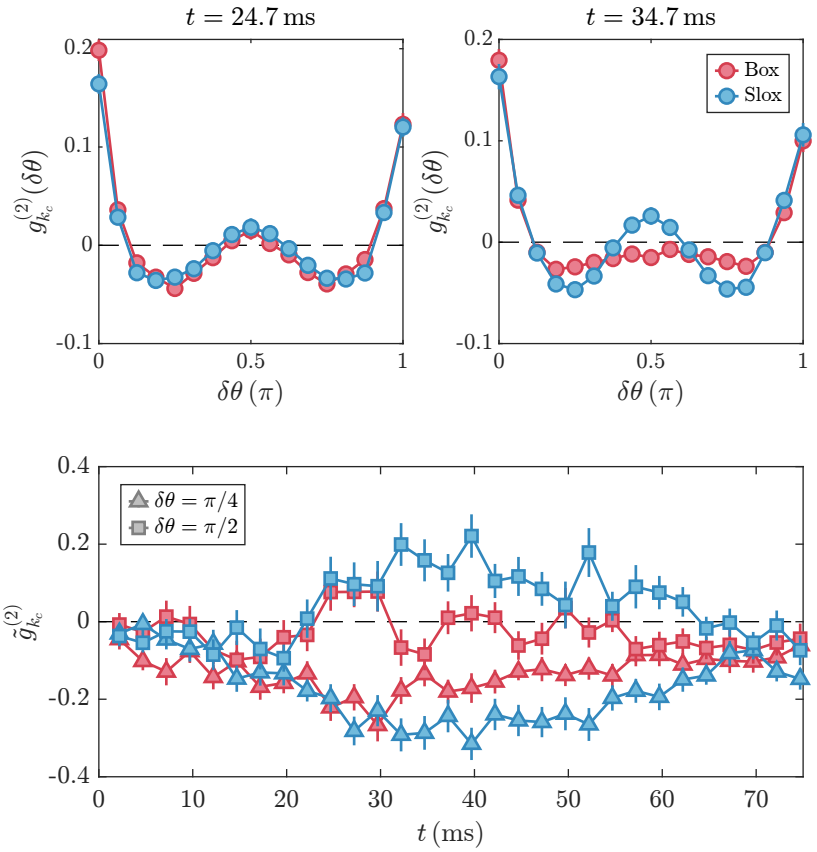

Figure 6.13: Square Lattice Correlations. The top row shows $g^{(2)}_{k_c}(\delta\theta)$ for two drive periods, showing that while the box and slox initially show the emergence of square lattices, the correlations are later damped in the box trap. Bottom row, extracted values for $\tilde{g}^{(2)}_{k_c}(\delta\theta)$. While square lattice correlations grow and are constant for about 30 ms in the slox case, they are damped in the box.

Chapter 7

Probing the Amplitude Equation

Having investigated the spontaneous emergence of patterns, we will now turn towards engineering specific lattice geometries, in order to investigate the nonlinear dynamics explicitly. In contrast to the spontaneous case, this will allow us to investigate unstable configurations, including phonons with phase lags relative to the drive and triangular lattices as opposed to square lattices. Additionally, we will attempt to initialize the system at the fixed-point solution, leading to square lattice patterns with long lifetimes.

We will first discuss how modulated superfluid densities can be prepared using periodically modulated potentials. We then use this technique to vary phonon occupations, as well as their relative phase to the drive, and compare this to the theoretical model. Finally, we discuss an alternative method to seed patterns using a phase imprint and discuss the optimization of lattice lifetime.

7.1 Phonon Preparation and Readout

The preparation of modulated clouds is described in Fig. 7.1. In the top left, the Thomas-Fermi approximation is schematically described [59]. We prepare a BEC, and then slowly ramp up a periodic modulation of a given contrast, such that the trapping potential is given by

$$V(\mathbf{r}) = \begin{cases} V_0[\sin(k_c x) + \sin(k_c y)] & |\mathbf{r}| < R_{\text{trap}} \\ V_0[\sin(k_c x) + \sin(k_c y)] + \beta(|\mathbf{r}| - R_{\text{trap}}) & |\mathbf{r}| \geq R_{\text{trap}}, \end{cases} \tag{7.1}$$

The value of V_0 sets the magnitude of the phonon amplitude, $|R|$. Then, we abruptly switch off the periodic modulation of the potential ($V_0 = 0$), and the modulated density immediately begins to show dynamics in the flat potential. Indeed in both

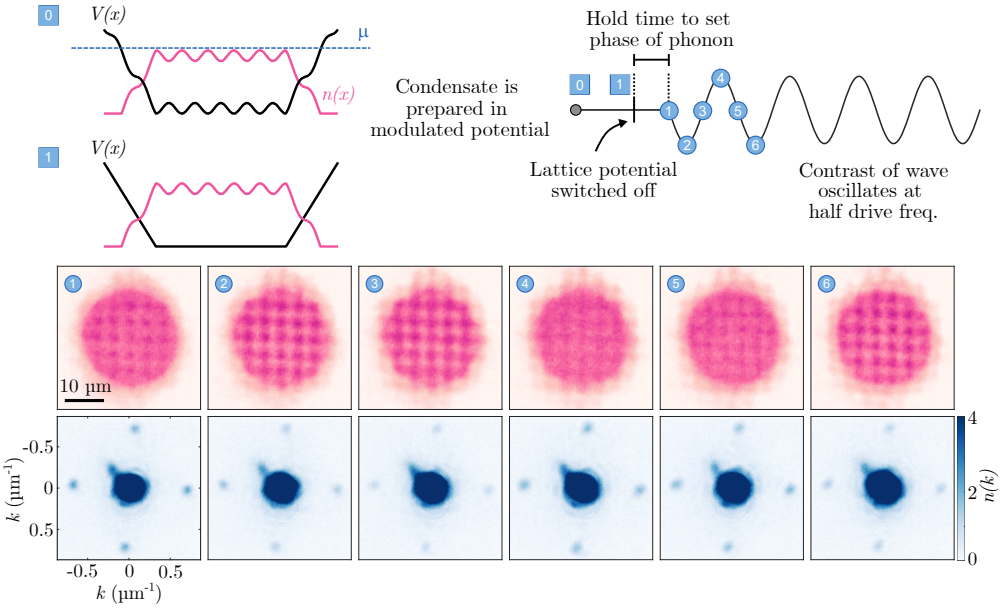

Figure 7.1: Density Imprint of Lattice. An overview of the experimental sequence for preparing lattices. Modulated potentials are loaded with atoms, leading to a modulated density (top left). The modulation of the potential is abruptly switched off, and then the periodic modulation of the scattering length is turned on after a certain hold time (right). In the bottom row, density and momentum distributions are shown after a hold time of 0.5 periods, showing an out-of-phase oscillation of the lattice contrast and diffraction peaks.

real and momentum space, the density of the cloud is observed to show the oscillations expected from Bogoliubov phonons, as described by Eq. (4.31) and Eq. (4.32).[1]

After the phonon has evolved for a certain hold time, the periodic modulation of the interaction is switched on. The frequency of the drive is adjusted to match the eigenfrequency of the imprinted phonon. The hold time between switching off the modulated potential and switching on the drive sets the phase of the phonons, $\varphi = \arg R$. With the full control over the parameters of the phonons, we can now probe phonon dynamics experimentally.

[1]Writing in a periodic modulation of the order parameter is of course not equivalent to spontaneously generating pairs of quasiparticles by driving the scattering length. At the very least, the two scenarios should be different in the correlations relating to the production of genuine quantum mechanical particle pairs. However, for the experiments performed here, we almost always work with large occupation numbers, and we have not observed any relevant differences in extracted observables between spontaneous and instigated patterns.

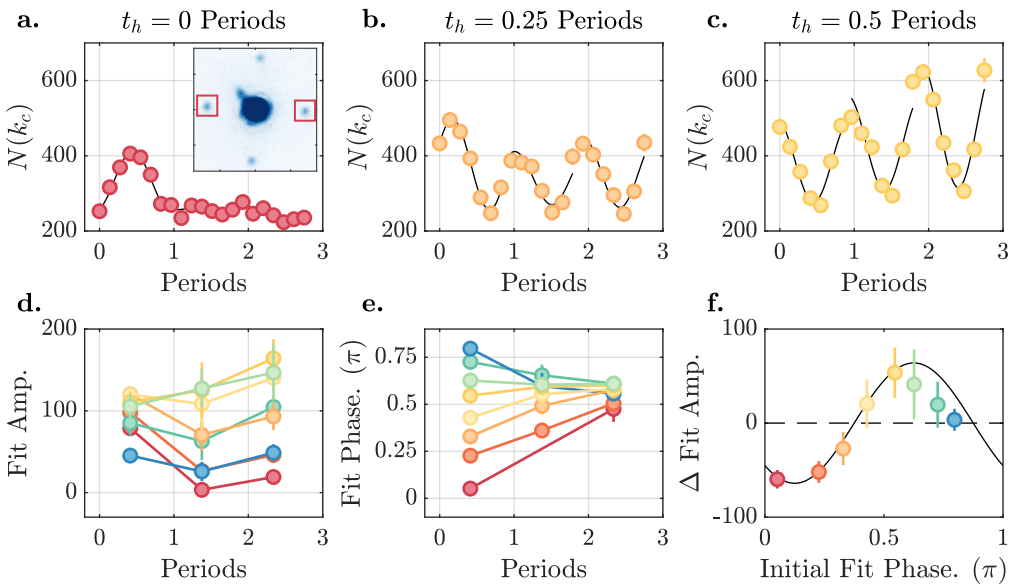

Figure 7.2: Varying Initial Phonon Phase. The top row (**a**-**c**) shows the average atom number in a summation box, as shown in the inset of **a**. In each case, a slightly longer hold time is implemented, as is evident by the initial phase of the oscillation in $N(k_c)$. The black lines show piece-wise fits to the oscillations. The fits are used to extract the time-dependent amplitude (shown in **d**) and phase (**e**). The difference in initial and final amplitude as a function of initial phase is plotted in **f**. The sinusoidal curve is a guide to the eye.

7.2 Variation of the Phonon Phase

A vital parameter in the amplitude equation is the phase between the phonon's oscillation and the drive, $\varphi = \arg(R)$, as can be seen in the dynamics of the contrast for one stripe,

$$\frac{d}{dt}|R(t)| = [-\alpha \cos(2\varphi(t)) - \Gamma]\,|R(t)|. \tag{7.2}$$

In order to experimentally probe the dependence of stripe dynamics on the phonon phase, we prepare square lattices with roughly identical contrast in the horizontal and vertical directions. Then, the modulation potential is switched off, and the drive is switched on after progressively longer hold times. After fractions of a drive cycle, we measure the momentum distribution, by abruptly performing a time-of-flight measurement. The parameters in this experiment are $r = 0.5$, $\omega_d = 2\pi \times 400\,\mathrm{Hz}$, $\mu = 2\pi\hbar \times 300\,\mathrm{Hz}$, and $k_c = 0.72\mu\mathrm{m}^{-1}$.

In order to quantify the dynamics, we integrate the signal in a region around the peaks in momentum space (shown in the inset of the upper left panel of Fig. 7.2). We then perform fits over an interval of roughly $\frac{3}{4}$ of a period, shown as the black lines in the top row of Fig. 7.2. The fitting function is given by

$$F = A[1 - \cos(2\pi t + 2B)] + C, \tag{7.3}$$

where t is the time in periods, A is proportional to $|R|^2$, $B = \varphi$ and C is an offset that accounts for the finite background. The value of $|R|$ is given by $|R| = \sqrt{\frac{A\epsilon}{N\mu}}$, where $N = 30 \times 10^3$ is the total atom number (see Eq. (4.32)). The factor two in front of the phase is because oscillations in momentum space are symmetric to changes of π, as this inverts the spatial phase of the phonon but otherwise has no effect. We therefore use fits to track both changes in amplitude as well as the slowly varying phase of the phonon oscillation.

The oscillations of occupations in momentum space are shown for three initial phases in the top row of the figure. The phase of the phonon can be tuned to either entirely damp the oscillation (**a**), remain at constant occupations (**b**), or increase phonon occupations (**c**). The lower row summarizes the results for all phases between 0 and π: phases close to zero (or π, due to the factor of two) result in the depletion of occupations, phases of $\pi/2$ lead to growth. Plotting the initial phase of the phonon relative to the change in amplitude over the three drive periods (**f**), a roughly sinusoidal behavior is apparent.

This confirms a fundamental feature of the amplitude equation, as the sinusoidal dependence of contrast on the phase of the phonon is apparent in the data, up to a phase shift. Indeed, this phase shift is crucial for understanding the stabilization mechanism, as nonlinearities slowly vary the phase until a stable configuration is reached. To investigate the interplay between the contrast and phase, we will now probe the dynamics of patterns with various initial contrasts.

7.3 Flow Diagrams

We can further probe the relationship between the amplitude and phase of the phonons by repeating the above experiment at a variety of initial contrasts. We always consider square lattices, with identical contrasts and phases in R_k and R_p. This significantly simplifies the theoretical prediction, which can now be completely captured by two parameters, the contrast $|R|$ and phase φ. While the contrast is governed by Eq. (7.2), the dynamics of the phase are

$$\frac{d}{dt}\varphi(t) = \alpha \sin(2\varphi(t)) - \lambda\left[1 + c_1(\theta) + c_2(\theta)\right]|R(t)|^2 . \tag{7.4}$$

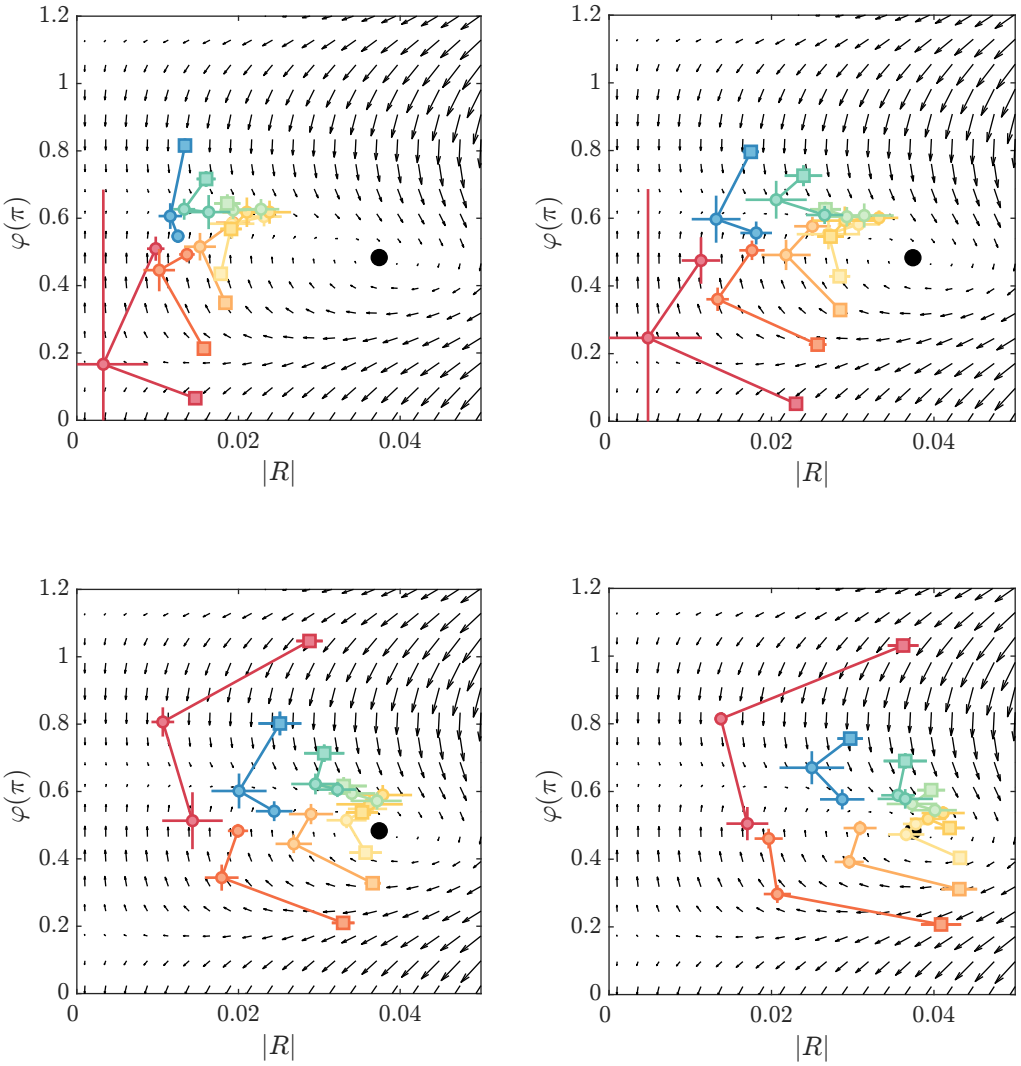

Figure 7.3: Experimentally Extracted Flow. Experimentally extracted amplitudes and phases (colorful markers) are compared to the first derivative of the amplitude equation (black arrows), for $R_k = R_p$ and $\theta = 90^o$. Each subplot shows different initial lattice imprint depths. The square point marks the first oscillation period, and the round circles the two following periods. The black point is the lattice fixed-point solution. The top right plot corresponds to the data shown in Fig. 7.2.

The results are shown in Fig. 7.3. The arrows show the direction and magnitude of the first derivative of the two-mode amplitude equation, using the effective λ (extracted in Section 6.2.3), damping $\Gamma = 0.4\alpha$ (determined in 6.2.2), and the theoretical values for α, c_1 and c_2. The black dot represents the fixed-point solution for $\theta = 90^{\circ}$. The colored markers are the extracted values of $|R|$, where the colors are different initial phases (as in Fig. 7.2). We experimentally observe a phase shift between the theory and experiment of roughly 0.15π, and flow diagrams are shifted by this value.

Each subsequent plot shows a different set of initial lattice contrasts. In each case, there is remarkable agreement between the experiment and the structure of the flows predicted by the amplitude equation. After a few periods, the stripes have mostly converged in amplitude and phase, except for the most extreme initial conditions. The phase to which stripes converge depends on the contrast, going from around 0.6π for small occupations to 0.5π at large occupations. At initial contrasts and phases that correspond to the fixed-point solution, the dynamics are significantly slowed. This provides experimental evidence for the existence of such a steady-state solution of the driven system, enabling the study of more exotic initial states.

7.4 Angle and Relative Phase

So far, the experiments have been effectively one-dimensional: we have imprinted lattices with identical initial phases and contrasts, $R_k = R_p$, at $\theta = 90^{\circ}$. In order to probe the angle-dependent interactions between the stripes, we will now prepare lattices with unstable configurations, where $\theta \neq 90^{\circ}$ and the initial phases of the stripes are different, $\varphi_k \neq \varphi_p$.

We are particularly interested in understanding how the contrast of stripes at certain angles evolves, and will therefore focus on the dynamics of $|R|$. In this section, we will consider the extended amplitude equation, where the magnitude evolves as

$$\begin{aligned}\frac{d}{dt}|R_k| = \Big[&-\alpha\cos(2\varphi_k) - \Gamma + \beta(\theta)\left|R_p\right||R_+|\sin\left(\varphi_p + \varphi_k - \varphi_+\right) \\ &+ \lambda c_2(\theta)\left|R_p\right|^2\sin\left(2\varphi_p - 2\varphi_k\right)\Big]|R_k|\,.\end{aligned} \tag{7.5}$$

Terms proportional to $c_2(\theta)$ are only nonzero if there is a phase difference between the stripes, i.e. $\varphi_k \neq \varphi_p$. Additionally, we will see that the dynamics in R_+ play a significant role in selecting the pattern geometry, and therefore the terms proportional to $\beta(\theta)$ must also be considered.

To perform the experiments, we seed lattices of both square and triangular geometries, i.e. once with $\theta = 90^{\circ}$ and once with $\theta = 30^{\circ}$. Then, the potentials that initialize the stripes are switched off separately at different times, such that their phases relative

to the drive are different, $\varphi_k \neq \varphi_p$. In order to simplify the dynamics somewhat, we will initialize the system such that $\varphi_k(t = 0) = \pi/2$, and vary $\varphi_p(t = 0)$, using $\varphi_p(t = 0) = \pi/4$ and $3\pi/4$. These values are selected such that the term proportional to $c_2(\theta)$ is maximized or minimized, using $\sin\left[2(\varphi_p - \varphi_k)\right] = \pm 1$.

The results are summarized in Fig. 7.4 and Fig. 7.5, which show data for $\varphi_p(t = 0) = 3\pi/4$ and $\varphi_p(t = 0) = \pi/4$, respectively. In each figure, the top row shows the initial momentum space density for the two angles, with the region used to extract R_k, R_p, and R_+ shown in red, green, and yellow, respectively. The left column of the lower plots shows the average atom number in one square box, with square markers for the square lattice and triangle markers for the triangular lattice. The right column shows the results of fits to the data, which are again used to extract $|R|$ and φ.

In each case, the initial magnitudes and phases of the phonons for $\theta = 90^o$ and 30^o are identical within error bounds. Initial magnitudes for $\left|R_{k/p}\right|$ are roughly equal, while $|R_+|$ grows steadily.[2] The later dynamics however, differ remarkably depending on the angle and initial phase. While the phases $\varphi_{k/p}$ stabilize very quickly to $\sim \frac{5}{8}\pi$ for all cases, the phase φ_+ for $\theta = 30^o$ does not stabilize to this value, drifting instead to a value of roughly π (which is equivalent to 0). The dynamics of the amplitudes $R_{k/p}$ are also very different: while in magnitudes for $\theta = 90^o$ grow regardless of initial conditions, for $\theta = 30^o$ one stripe always remains dominant over the other.

To piece apart how these results fit to the amplitude equation, we will consider two regimes: early times, where $|R_+|$ is very small, and later times, where R_+ has reached a steady state.

At early times, the dynamics are dominated by the $c_2(\theta)$ term, which is positive for $\theta = 30^o$ and negative for 90^o (see Fig. 4.7). To extract angle-dependent effects, we will consider the relative difference in stripe amplitude, $\Delta|R|_{\text{rel}} = |R_k| - |R_p|$, as plotted for the two pattern geometries in the top row of Fig. 7.6. In the case where $\varphi_p - \varphi_k > 0$, the c_2 term in the equation for $|R_k|$ is positive for the triangular lattice and negative for the square lattice. For the stripe $|R_p|$ this is inverted, due to the inversion of φ_p and φ_k. This means that for the triangular lattice, the two stripes' magnitudes should diverge, whereas they should converge for the square lattice. As is shown in the upper left panel, this expected behavior is confirmed, showing a roughly constant $\Delta|R|$ for $\theta = 90^o$, but diverging contrasts for 30^o.

In the case where $\varphi_p - \varphi_k < 0$, this behavior should invert. While the general tendency is present in the data, the differences are not as large. This is possibly because the initial value of $\varphi_p = \pi/4$ results in diminished occupations in R_p and therefore lower coupling between stripes. These results confirm that the relative phase between stripes can determine their dynamics depending on pattern geometry.

[2]The amplitude of the oscillation of occupations in momentum space is much larger the R_+ mode with $\theta = 90^o$ due to the nature of Bogoliubov quasiparticles. Using the prefactor ϵ_+/μ results in comparable values for R_+ for both geometries.

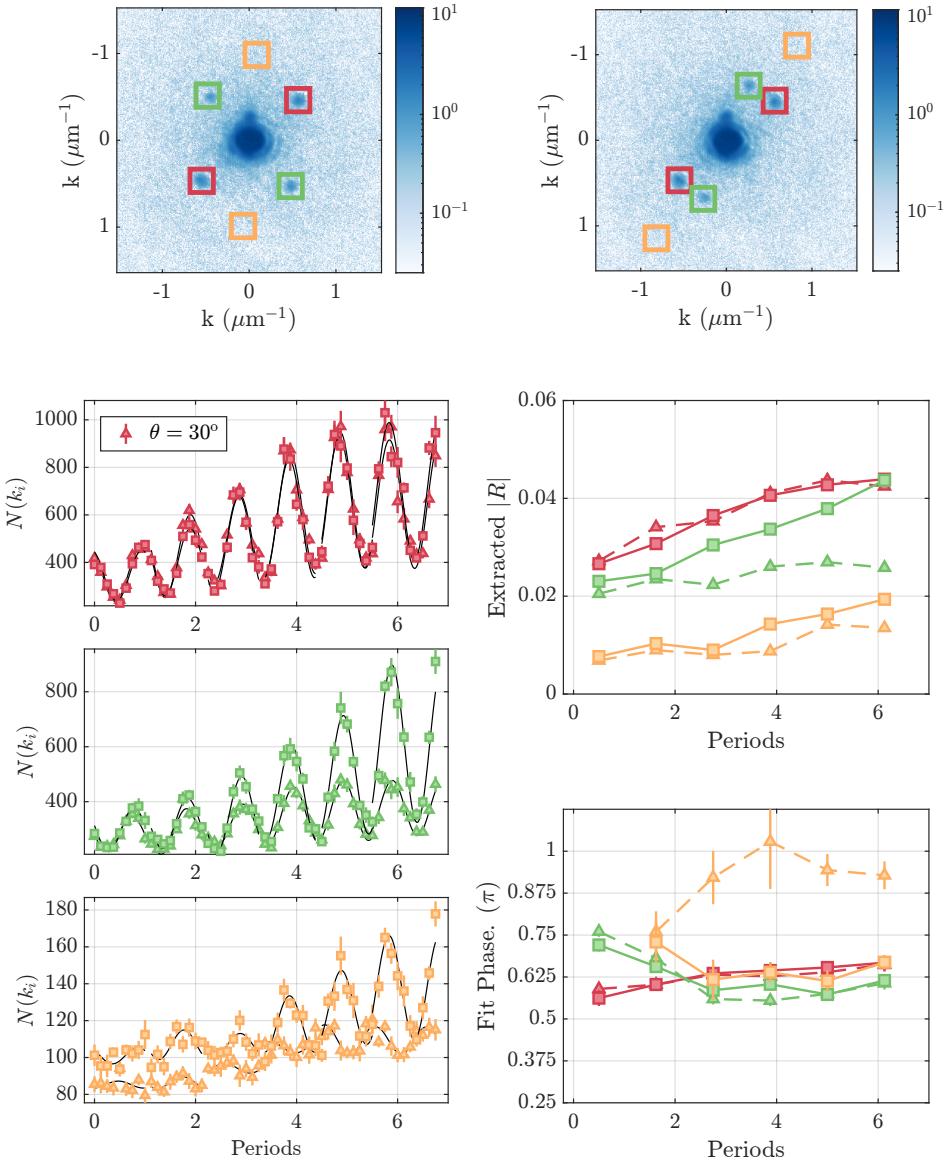

Figure 7.4: Different Initial Phases, $\varphi_\mathbf{p} - \varphi_\mathbf{k} > 0$. The top row shows initial density distributions for the two lattice geometries, and the region used to extract R_k (red), R_p (green), and R_+ (yellow). The lower left column shows average atom numbers in one square summation region, with square markers showing data for $\theta = 90^o$ and triangles 30^o. The lower right column shows extracted amplitudes and phases. The phase for the first period of the R_+ mode is not plotted, as amplitudes are very small and the phase cannot be extracted reliably.

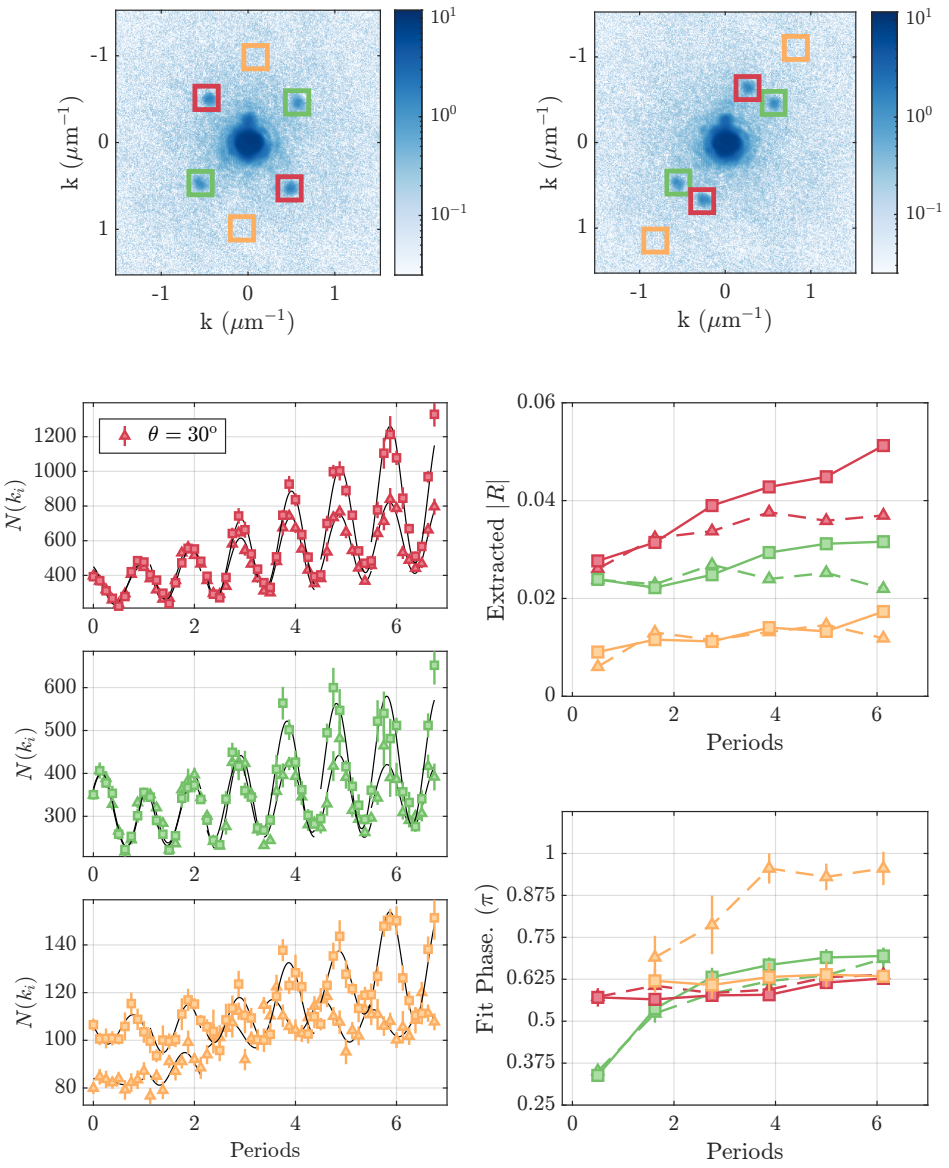

Figure 7.5: Different Initial Phases, $\varphi_\mathbf{p} - \varphi_\mathbf{k} < 0$. The figure is identical to the previous one, but the initial phase $\varphi_p(t = 0)$ has now been varied to be smaller than $\varphi_k(t = 0)$. In this configuration, the green stripe does not initially grow. However, at late times the 90^o pattern shows growth in both stripes, while the 30^o pattern saturates in amplitude after a short time. For the 30^o pattern, a large phase difference between the R_+ mode and $R_{k/p}$ modes is apparent.

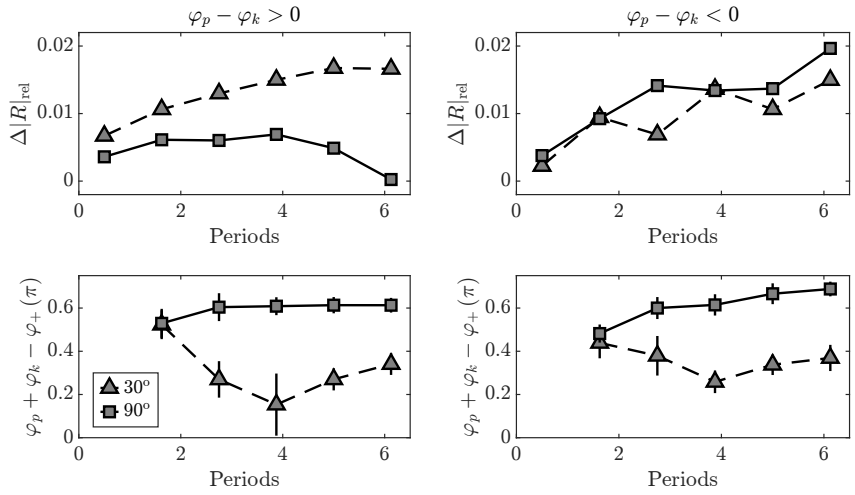

Figure 7.6: Effect of Couplings. The top row shows the difference in stripe contrast, whereas the bottom row shows the phase difference $\varphi_p + \varphi_k - \varphi_+$. The left column shows these extracted values for $\varphi_p - \varphi_k > 0$ and the right for $\varphi_p - \varphi_k < 0$. The change in relative contrast aligns to the expected angle dependence of the amplitude equation, and the change in the phase difference points to lower global occupations for $\theta = 30^{\mathrm{o}}$.

At late times, the emergence of R_+ indicates the relevance of the term proportional to $\beta(\theta)$. The magnitude of $\beta(\theta)$ changes slightly between 30° and 90° but is always positive, making the comparison between the geometries more straightforward. Here, the most significant difference between the square and triangular lattices is the phase of R_+, which affects the dynamics through the factor $\sin\left(\varphi_p + \varphi_k - \varphi_+\right)$. The phase difference $\varphi_p + \varphi_k - \varphi_+$ is plotted for the two initial phases, and a clear angle dependence is apparent. While the phase difference stays roughly constant at 0.6π for $\theta = 90^{\mathrm{o}}$, it approaches zero for 30°, indicating a significantly diminished growth rate. This corresponds to the globally lower occupations in the triangular lattice.

These results qualitatively confirm the structure of the amplitude equation: angle-dependent interactions between phonons indeed determine the dynamics of phonon magnitudes, and stripes at 90° separation are able to grow to larger values than those separated by 30°. Despite the agreement to the structure of the AE, a quantitative comparison is outstanding. The experimental results do not match neatly with either the two-mode or three-mode model, likely because assumptions made to construct the theoretical model are invalid. Problematic assumptions could be the lack of amplitude-dependent damping, not including the R_- mode, or the experimental reality of occupations at many other higher order modes.

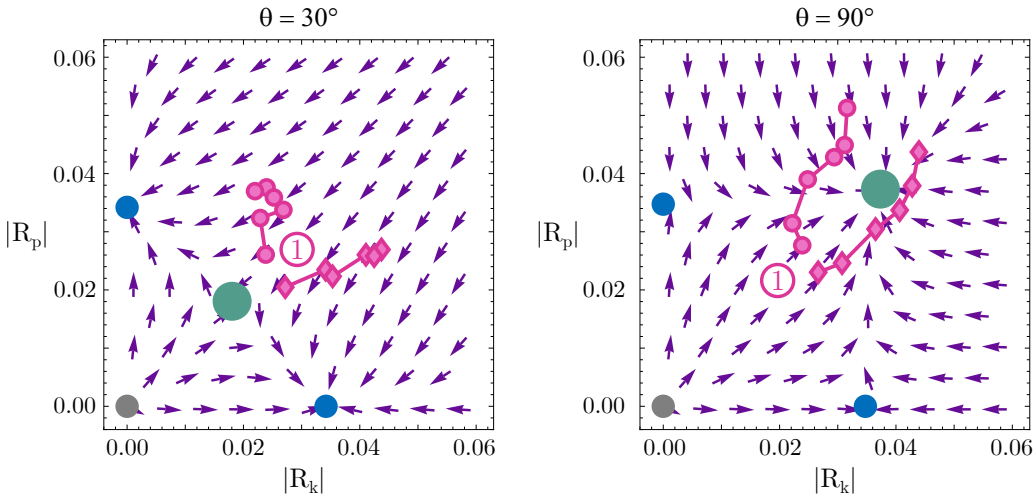

Figure 7.7: Force Fields And Stability. The plots show experimental data (pink markers) compared to the direction of the second derivative of the amplitude equation (purple arrows), in the plane where $\varphi_{k/p} = \varphi_{\mathrm{fp}}$. The gray, blue, and green points show the homogeneous, stripe, and lattice fixed-points, respectively. The left plot shows such a force field for $\theta = 30^{\mathrm{o}}$, right for 90^{o}. The pink diamonds and circles show different initial phases of R_k, corresponding to data from Fig. 7.4 and Fig. 7.5, respectively. The results show that the experiment indeed has a high degree of angle-selectivity, as is apparent in the dramatically different trajectories between the two angles.

7.5 Stability Diagram Representation

The dynamics discussed above attempt to capture the full information extracted from the experiment, effectively describing dynamics in a four-dimensional space. A somewhat simpler representation of the data is a projection onto a two-dimensional space, where the phonon phases are at the fixed-point values, $\varphi_k = \varphi_p = \varphi_{\mathrm{fp}}$. This is motivated by the fast phase-locking of the phonons to the phase of the fixed-point after only a few drive periods. In this plane, one can construct a "force field" representation of the amplitude equation, plotting only the second derivative in this now two-dimensional plane. The second derivative is given by

$$\frac{d^2}{dt^2}|R_k|\Big|_{\varphi_{\mathrm{fp}}} = 2\lambda\left[\bar{R}^2 - c_2(\theta)|R_p|^2\right]\left[\bar{R}^2 - \left(|R_k|^2 + (c_1(\theta)+c_2(\theta))|R_p|^2\right)\right]|R_k|, \tag{7.6}$$

where $\bar{R} = \sqrt{\frac{\sqrt{\alpha^2-\Gamma^2}}{\lambda}}$ is the amplitude of the stripe fixed-point. The second derivative can be thought of like a force to which the amplitudes respond in the plane where

the phases have locked to the driving. We will now compare the dynamics to the expected force fields, using the extracted λ_{eff} and $\Gamma = 0.4\alpha$.

Figure 7.7 shows these force field diagrams for the two experimentally implemented angles. The purple arrows show the direction of the force field, and the four solid points show the fixed-point solutions for the homogeneous, stripe, and lattice cases (gray, blue, and green, respectively). In pink, we show the extracted stripe magnitudes from the measurements in Fig. 7.4 and Fig. 7.5, corresponding to the diamonds and circles, respectively. The encircled 1 demarcates the initial conditions.

The differences between $\theta = 30^{\text{o}}$ and 90^{o} are now obvious–while the trajectories of the amplitudes at $\theta = 30^{\text{o}}$ tend towards stripes and are dramatically slowed at low values of $|R|$, for $\theta = 90^{\text{o}}$ amplitudes grow significantly, and trajectories are curved inwards towards the fixed-point. This further verifies that under experimental conditions, the structure of the AE captures the dynamics.

7.6 Optimizing Pattern Stability

Having probed the fixed-point description of the amplitude equation, we now turn to optimization of pattern lifetimes. We will effectively attempt to initialize patterns at the fixed-point solution, such that it is as stationary in time as possible. This will be useful for later experiments, where we will quantitatively describe the excitations of the patterns.

So far, we have prepared patterned states by initializing modulated density distributions. A similar method of preparing phononic coherent states is by imprinting a modulated phase on the condensate order parameter. This is also done using an external potential, but the external potential is only flashed on very briefly. Experimentally, this method was found to lead to longer lifetimes of the lattice, as well as improved stability of lattice parameters.

7.6.1 Optimizing Drive Frequency

The first parameter to scan is the drive frequency. Because the imprinted lattice now defines the length scale, the frequency of the drive must be tuned to match the resonance condition, roughly set by the dispersion relation (and therefore the chemical potential). To do so, we flash on a periodically modulated light field, with lattice wavelength $8\,\mu$m. First, the intensity is chosen such that the resulting lattice contrast is roughly tuned to correspond to the fixed-point value for the given drive amplitude. Then, after a fixed hold time ($t_h = 0.5$ ms), we begin modulating the scattering length with different drive frequencies, ranging from 400 to 450 Hz.

In Fig. 7.8, the contrast and wavenumber of the lattice in the horizontal direction are plotted. These are extracted by integrating the density in the vertical direction, and

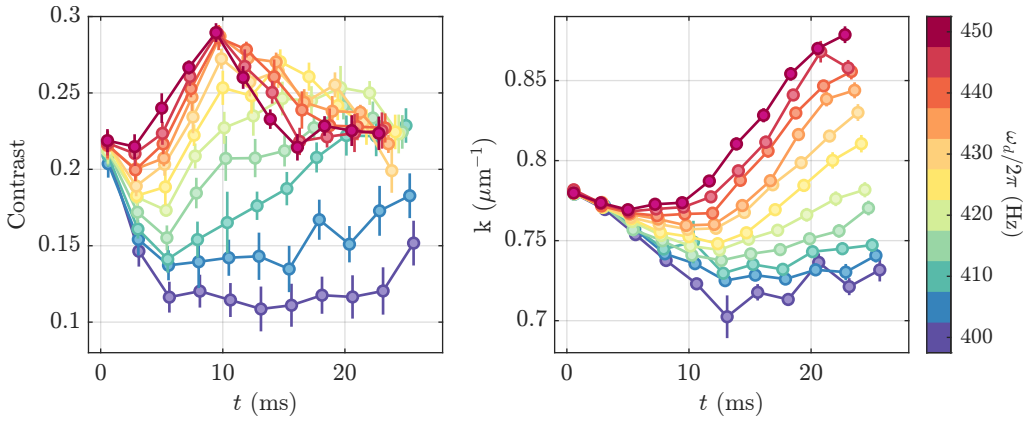

Figure 7.8: Varying Drive Frequency. Left, the contrast of the lattice in the x-direction throughout the drive, where each color represents one drive frequency. The contrast is extracted using a sine fit. Changes in contrast are minimal at around 420 Hz. Right, the wavenumber of the stripe, extracted using a sine fit. The wavenumber drifts throughout the drive, and variations are also minimized at around 420 Hz. Parameters for this measurement are $r = 0.4$, and $t_h = 0.5$ ms.

performing a sinusoidal fit to the lattice in a central region of the cloud. Interestingly, the frequency plays a role similar to the initial phase of the phonons–it can be tuned to lead to decreasing, roughly constant, or increasing lattice contrasts. The wavenumber typically decreases slightly initially, or begins to increase after a short period of time. In this measurement, the drive amplitude does not match the seeded lattice contrast, and therefore there is no situation where the contrast is clearly stabilized throughout the dynamics.

7.6.2 Optimizing Drive Amplitude

The external imprint sets not only the length scale of the pattern, but also its contrast, and the drive amplitude must be calibrated to ensure that this contrast is stable over time. To do so, we fix the drive frequency to $\omega_d = 2\pi \times 420$ Hz and the initial hold time to $t_h = 0.2\frac{2\pi}{\omega_d} = 0.47$ ms. We then vary the drive amplitude, from $r = 0.25$ to $r = 0.35$, as shown in Fig. 7.9. While an initial dip is present for all drive amplitudes, $r = 0.3$ results in the most stable contrasts over time at roughly the value that was initially imprinted. Lower amplitudes also lead to stable contrasts, but at a reduced value. Regardless of drive amplitude, the initial decrease in contrast is remarkably reproducible, and further experiments (not shown here) determined that changes in the initial phase of the imprinted phonon also do not improve the stability. We therefore turn to a further degree of freedom, namely the occupation of the R_+ mode.

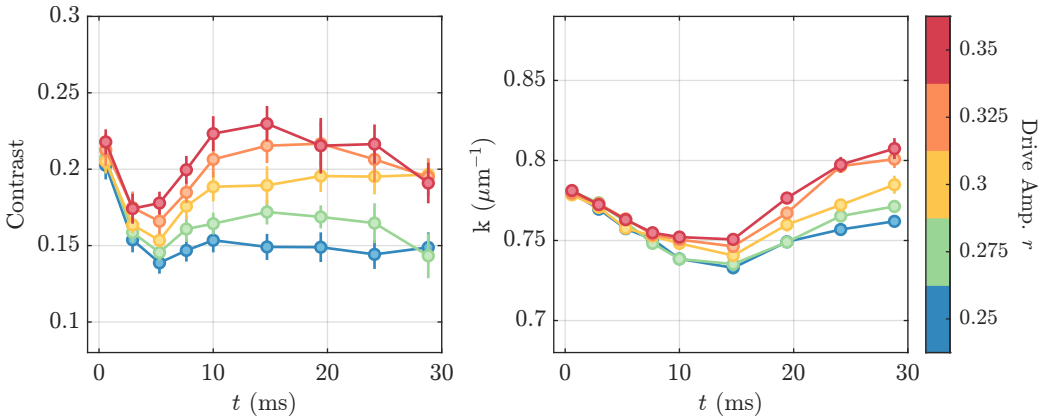

Figure 7.9: Varying Drive Amplitude. Left, contrast of lattice, extracted identically to the previous figure. Variations in contrast are minimized at drive amplitude $r = 0.3$. Left, changes in lattice wavenumber. Parameters for this measurement are $\omega_d = 2\pi \times 420\,\text{Hz}$, and $t_h = 0.2\frac{2\pi}{\omega_d} = 0.47\,\text{ms}$.

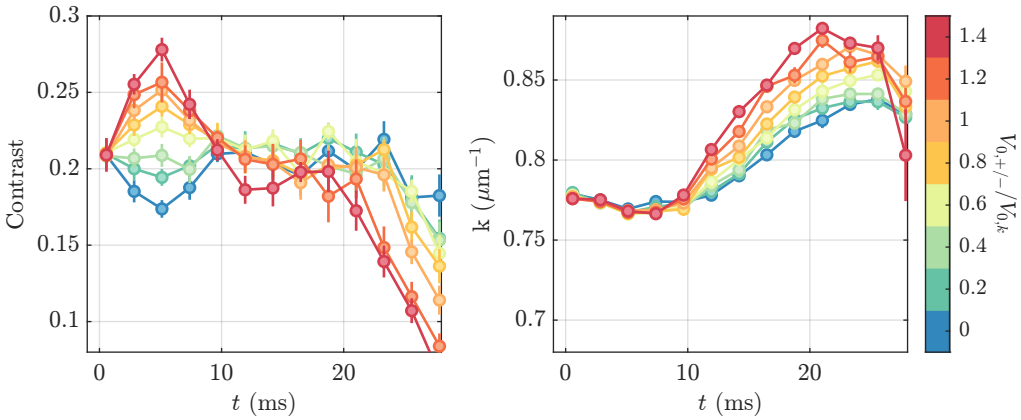

Figure 7.10: Varying Initial Occupation in $R_{+/-}$. Left, contrast of lattice in x-direction at k, for varying imprint intensities of the $R_{+/-}$ mode. Not only can the initial dip in lattice contrast be minimized, at large imprint depths the initial contrast increases. Right, the wavenumber of the lattice. The drift in wavenumber is likely a result of imperfect frequency calibration. Here, the parameters used are $r = 0.3$, $\omega_d = 2\pi \times 440\,\text{Hz}$, and $t_h = 0.15\frac{2\pi}{\omega_d} = 0.34\,\text{ms}$. The different frequency and hold time as compared to the previous figures reflect a higher atom number and chemical potential.

7.6.3 Optimizing Occupations in R_+

Having exhausted parameters of $R_{k/p}$ that can explain the initial decrease in contrast, we now separately imprint $R_{+/-}$ modes.[3] This is motivated by the experimental observation that at the time where the contrast of R decreases, occupations at $R_{+/-}$ become large. In order to seed the higher momentum modes, we first imprint a normal square lattice, and then after a quarter period hold time imprint two modes, with a potential of the form

$$V(\mathbf{r}) = V_{0,+/-}[\cos([\mathbf{k}+\mathbf{p}]\cdot\mathbf{r}) + \cos([\mathbf{k}-\mathbf{p}]\cdot\mathbf{r})], \tag{7.7}$$

which is a square lattice with 45° orientation to the base lattice and has a wavelength of $\sqrt{2}k$. As a basic first check, we scan $V_{0,+/-}$, varying it from 0 (which is therefore identical to the imprints as shown in Fig. 7.8 and Fig. 7.9) to 140%.

The results, shown in Fig. 7.10, show that the initial decrease in lattice contrast can indeed be minimized by the additional imprint. Not only can the initial dip in lattice contrast be removed (as is the case for $V_{0,+/-}/V_{0,k} = 0.4$), if the secondary lattice is too large in magnitude, the stripe contrast increases dramatically. It should be noted that in these measurements, the frequency calibration was likely not optimal, and therefore the lattice wavenumber is not as constant as in the other measurements, likely leading to a more rapidly decreasing contrast at late times.

This method for eliminating the initial decrease in contrast was discovered after the measurements on pattern excitations (detailed in the following chapter) were performed. Therefore, the role of $R_{+/-}$ in lattice rigidities and excitations is an outstanding experimental question.

[3] At 90°, the modes R_+ and R_- are identical, because of the geometry of the square lattice.

CHAPTER 8

Supersolid Sound Modes

In the previous chapters, we have established how square lattice patterns emerge spontaneously in the driven superfluid. We have also probed the patterns' stability, demonstrating that we are able to imprint lattices of specific contrasts and wavelengths. As a superfluid state with stable periodic density modulations, these patterns are reminiscent of a seemingly different physical system, namely supersolids.

Supersolids are a state of matter defined by two spontaneously broken symmetries: U(1) symmetry and translational symmetry. These systems show spontaneously emerging periodic density modulations (related to translational symmetry breaking), but are also phase coherent (connected to symmetry breaking), and thus demonstrate an interesting interplay of delocalized particles in localized density structures. A key feature of supersolids is the emergence of two Goldstone modes corresponding to the two broken symmetries, which are each influenced by characteristics of the lattice and superfluid. In this chapter, we will show that similar dynamics can be observed in the driven superfluid.

The chapter is organized as follows. We first provide a brief overview of the most important concepts for understanding supersolids. In particular, we discuss a hydrodynamic description of superfluid smectics (i.e. a superfluid with a density modulation in one direction), which is derived based only on spontaneously broken symmetries and conserved quantities. We then motivate the application of such a framework to the driven system, and experimentally demonstrate the propagation of two distinct Goldstone modes in a stripe pattern. Moving to two dimensions, we probe transverse sound excitations in the square lattice, showing that in the current regime, the pattern can be described as two independent superfluid smectics. Finally, we investigate localized phase defects, showing that the dynamics of wavepackets are consistent with those of the collective modes.

8.1 Supersolidity

The question of whether a solid can be superfluid goes back to the 1960s and early 1970s, when a number of works investigated the interplay of periodic density modulations and frictionless superfluid flow. As early as 1960, Gross noted that bosons with attractive interactions can have groundstates that are periodically modulated in space, while still showing occupations in the $k = 0$ mode [24]. Andreev and Liftshitz considered defects flowing through a crystal lattice [25], finding that these could have superfluid properties. In the context of discussions on whether BECs are superfluids, Chester postulated that while BECs could indeed show crystalline ordering, this solid-like behavior would "presumably prevent the appearance of any normal superfluid properties" [26]. The notion of superfluid solids was further investigated by Leggett [27], who defined the concept of the superfluid fraction, which quantifies the superfluid response of a spatially modulated superfluid order parameter.

In recent years, the study of supersolidity has flourished due to the definitive observation of supersolids in three different platforms. In contrast to the historical notion of solids with superfluid properties, these platforms instead showed how solid-like properties can emerge in superfluid systems.

The first of the three platforms was a BEC in a set of two external cavities, which is optically pumped with a standing wave from a third direction [28]. Randomly scattered light has a chance of coupling into either one cavity or the other, which leads to the growth of a standing wave along one cavity axis. While the random selection of one cavity or the other motivated the spontaneous breaking of translational symmetry, measurements in momentum space showing macroscopic occupations at $k = 0$ were taken as a sign of superfluidity. A later work showed that transverse lattice sound waves can propagate through such systems when using a multimode cavity [92].

Parallel experiments demonstrated signatures of spontaneously arising periodic density modulations in a superfluid with spin-orbit coupling (SOC) [29]. SOC emerges due to a coupling of internal (spin) and external (momentum) states through a two-photon Raman process between two spin states. The emergent dispersion relation has two minima at finite momenta and can result in stationary standing wave solutions [93]. The periodic density modulation was measured using Bragg scattering, and superfluidity was again determined by observing macroscopic occupations at $k = 0$. Recently, Goldstone modes have been observed in SOC supersolids [44], which show finite rigidity of the lattice and superfluid modes.

In the late 2010s, a series of publications showed the emergence of periodic density modulations in ultracold gases with large dipolar moments [30–32]. Dipolar atoms have a large magnetic moment, which leads to anisotropic dipole-dipole interactions that can be of the same order as contact interactions. A combination of anisotropic interactions and harmonic trapping leads to spatially modulated densities, with phase

coherence between individual lattice sites. Tuning the trap geometry was also shown to result in two-dimensional supersolids [94].

After these initial demonstrations, many experiments were conducted definitively showing the superfluidity of dipolar supersolids [33, 36, 38, 39, 42, 43]. Further experiments also demonstrated dual-frequency response, indicating that the two broken symmetries indeed lead to multiple branches of the dispersion [34, 35]. Finally, dipolar gases have been shown to have a diminished superfluid fraction, by observing Josephson oscillations between neighboring density peaks [42].[1]

8.2 Supersolid Hydrodynamics

A minimal ansatz to describe a supersolid order parameter in one dimension is

$$\psi = \psi_0 \mathrm{e}^{i\theta_s} \left[1 + \phi \cos\left(k_c x + \theta_l\right)\right], \tag{8.1}$$

where ψ_0 is a real constant, θ_s is the phase of the superfluid, ϕ is the contrast of a periodic modulation, k_c is a length scale set by the underlying Hamiltonian, and θ_l is the spatial phase of the periodic modulation. If symmetries are spontaneously broken, the Hamiltonian determines finite values for $|\psi|$ and $|\phi|$, while phases are free to vary, $\theta_{s/l} \in (-\pi, \pi]$. Although global variations to either phase come at no energy cost, spatial variations of these phases $\theta \to \theta(x)$ generically have an associated rigidity (or compressibility).

A key feature of supersolids is the emergence of two sound modes, which are determined by the compressiblities of the lattice and superfluid. Indeed, this is a universal feature of systems that spontaneously break U(1) and translational symmetries, as long-wavelength (i.e. low-energy) excitations of thermodynamic phases can be described entirely in terms of conserved variables and broken symmetries [48, 49, 96]. As discussed previously, supersolidity arises in a wealth of different systems, and while the quantitative characteristics of excitations will depend on the microscopic description in each case, the generic long-wavelength behavior is common to all systems.

One case that is of interest is the description of excitations in a two-dimensional superfluid that is modulated along only one direction. Such states have a number of interesting properties, such as anisotropic superfluid fraction. Because the system is purely fluid in one direction but has crystalline order in another, these configurations

[1] While vortex lattices and bright soliton trains were both shown to support collective lattice oscillations [8, 95], these systems are not considered supersolids. In a vortex lattice, vortex positions are rigidly coupled to the superfluid phase, and therefore no additional Goldstone mode for translational symmetry breaking emerges. In soliton trains, the stability of the periodic density modulation is supported by π phase jumps between solitons, likely precluding the presence of long-wavelength phase modes.

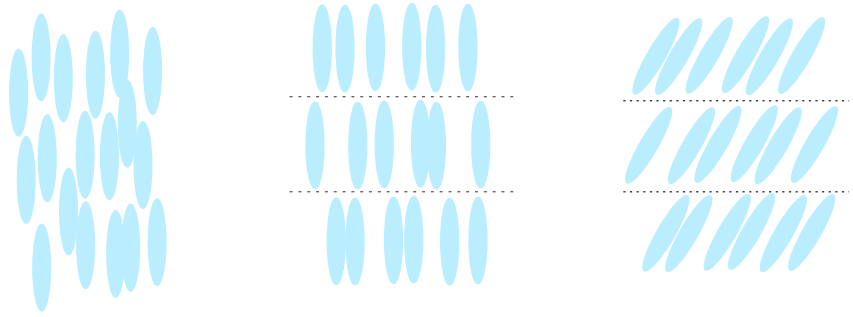

Figure 8.1: Classical Smectics. Left, the pnematic phase, in which elongated molecules are oriented to a common axis but show no other ordering. Center, the smectic A phase, where molecules organize into two dimensional layers, but can flow freely within the layers. Right, smectic C phase, where molecules tilt relative to the ordered axis. Phase transitions between these three orderings are controlled by temperature, from pnematic at high temperatures to smectic C at low temperatures [97]. The system we consider is most similar to the smectic A phase, where each layer consists of superfluid.

are similar to smectic liquid crystals (see Fig. 8.1), where long molecules are aligned such that they have liquid properties as well as crystalline structure [97].

In order to determine the generic characteristics of sound in a superfluid smectic, one considers the differential of the entropy, as well as a series of continuity equations based on the conserved quantities of momentum, energy, and particle number [48, 49]. Then, one can derive the dynamics for deformation fields of the phase,

$$\theta_{s/l}(x, y) = \bar{\theta}_{s/l} + \delta\theta_{s/l}(x, y), \tag{8.2}$$

where $\bar{\theta}_{s/l}$ is the mean phase defined by the bulk and $\delta\theta_{s/l}(x, y)$ are spatially dependent perturbations. Specifically, one can calculate the slope of the dispersion relation where the perturbation length scale q approaches zero. This characterizes the Goldstone modes of the system.

Here, we will consider a density wave in the x direction, i.e. $\psi = \psi_0 e^{i\theta_s(x,y)}\left[1 + \phi\cos\left(k_c x + \theta_l[x, y]\right)\right]$, and thus excitations along the x axis are longitudinal, while those along y are transverse.[2]

[2]Transverse modes can be generically defined as perturbations at all angles other than 0^o, i.e. any angle not parallel to the wavevector of the density modulation. However, such excitations have not been studied in detail in this work, and therefore we define transverse excitations as perpendicular to the standing wave.

As is shown in Refs. [48, 49], superfluid smectics support two longitudinal propagating sound modes:

$$c_{\pm}^2 = \frac{K}{2\rho} + \frac{B}{2\rho_n} \pm \frac{1}{2}\left[\left(\frac{K}{\rho} + \frac{B}{\rho_n}\right)^2 - 4f_s\frac{KB}{\rho\rho_n}\right]^{\frac{1}{2}}, \tag{8.3}$$

where K is the bulk compression modulus, B is the layer compression modulus, f_s is the superfluid fraction, and ρ is the mass density defined as $\rho = \rho_n + \rho_s$ with ρ_n and ρ_s the normal and superfluid density tensors, respectively. In the transverse direction (at $T \sim 0$), there is one propagating sound mode,

$$c_{\perp}^2 = \frac{K}{\rho}. \tag{8.4}$$

Thus, sound in the perpendicular direction is unmodified by the presence of the modulation in x, and the speed of sound is simply the root of the bulk compressibility.

The speeds in the longitudinal direction split around the superfluid speed of sound of the unmodulated system and are parameterized by two characteristics of the modulated state: the layer compression modulus, and the superfluid fraction. While the superfluid fraction is indicative of a diminished superfluid response due to a modulated density, the layer compression modulus determines how stiff the lattice is to spatial deformations. It should be noted that the slow and fast branches cannot be uniquely traced back to either superfluid or lattice modulations, and that the underlying modes generically have contributions of density and lattice modulations. This is also reflected in the speeds of sound, e.g. the slow mode is only uniquely determined by superfluid parameters in the limit of an infinitely stiff lattice [98, 99]:

$$B \to \infty,\ c_- \to \sqrt{f_s}c_{\perp} \tag{8.5}$$

8.3 Application of Hydrodynamics to Driven System

The hydrodynamic model is derived for systems that show spontaneous U(1) and translational symmetry breaking, and fulfill momentum, energy, and particle number conservation. Its applicability to the driven system is not given, as steady states of driven systems do not in general conserve energy. In this section, we will therefore go through each relevant parameter and motivate the application of the hydrodynamic model to the patterned state.

The pattern has already been shown to have self-stabilizing, spontaneously arising periodic density modulations, indicating spontaneous translational symmetry breaking. As the emergence of the pattern relies on the superfluidity of the state, it is also a good assumption that the state maintains some superfluid phase rigidity.

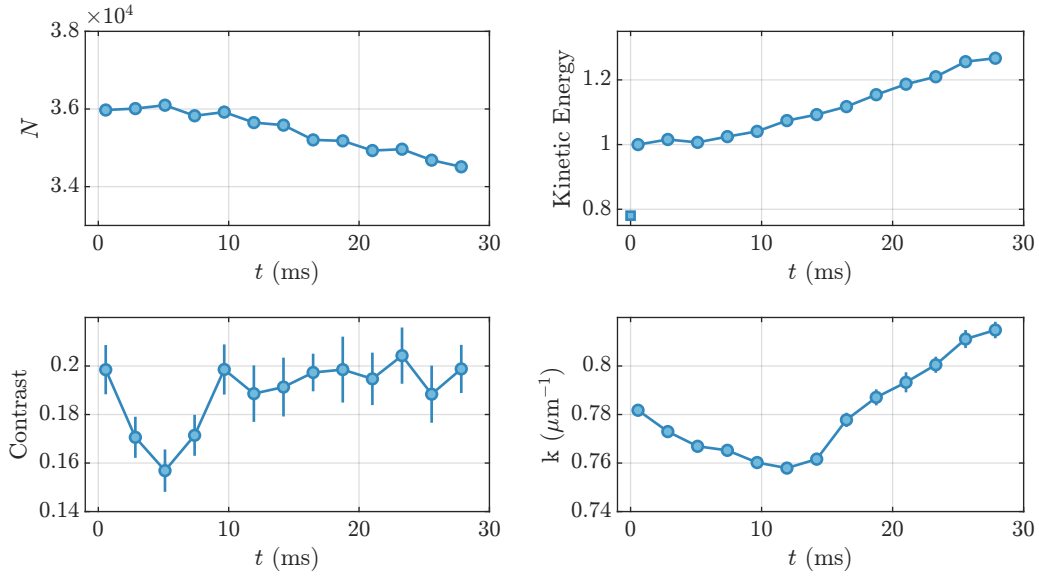

Figure 8.2: Relevant Experimental Quantities Over Time. Top left, the total atom number in the trap. Top right, the maximal kinetic energy for each drive period, relative to the first time after the lattice is imprinted. The square shows the kinetic energy without the imprint. Bottom left, the contrast of the stripe. The initial decrease is discussed in Section 7.6.3. Bottom right, the wavenumber of the stripe. Standard error of the mean is either shown or is smaller than the markers.

Regarding conserved quantities, the lack of an external potential (other than at the boundaries) means that momentum is conserved. Particle number and energy conservation are determined by measuring the density distributions after $n_P + 0.25$ drive periods in real space and $n_P + 0.75$ in momentum space. We extract the atom number, total kinetic energy, stripe contrast, and stripe wavenumber throughout the dynamics. The results are summarized in Fig. 8.2. The atom number is given by the integral over the whole cloud, while the contrast and wavenumber are extracted using a sinusoidal fit to the average density $n(x)$ in a central region with a width of $\sim 40\,\mu$m. The energy is given by integrating the kinetic energy distribution, $N(k) \times k^2$, up to a cutoff slightly above $2k_c$ (the specific value does not make a qualitative difference).

The particle number changes by less than 5%, and the energy changes by less than 10% in the first 15 ms of driving (corresponding to the first 8 drive periods). It is therefore a reasonable assumption that the quantities relevant for the hydrodynamic framework are sufficiently conserved.

Finally, the hydrodynamic model considers groundstates with lattices of a static contrast. The pattern is not static, but is rather a stable, rotating state, where the stripe amplitude ϕ rotates in the complex plane with half the drive frequency. As

discussed in the previous section, this means that the contrast of the stripe varies within a drive period. While a full description of the dynamics throughout a drive period are certainly worthy of further study, in this work we will stroboscopically measure the cloud, considering only the time when the density (phase) is maximally (minimally) modulated, $n_P + 0.25$.

8.4 Probing Lattice Phase Defects

In order to probe the hydrodynamic framework of superfluid smectics, we first perform measurements on a stripe pattern, where the density is modulated in only one direction. Though stripes are unstable towards becoming square lattices for late times, the growth of modulations in the vertical direction is negligible in the times considered here (with growth rates shown in Fig. 6.3, only a 10% increase in contrast in the vertical direction is expected). We can prepare stripes that correspond to the commensurate contrast and wavenumber for the drive, stabilized using the same mechanism demonstrated in the previous chapter.

In order to probe lattice Goldstone modes, we can prepare stripes with slow lattice phase deformations $\delta_l(x, y) = 0.2\pi \cos(qx)$, where $q < k_c/2$. We then measure the dynamics of the perturbation by extracting the positions of lattice maxima and minima after subsequent drive periods. The deformation is simply given by the difference in the fitted positions between a perturbed and unperturbed stripe.

The procedure for one perturbation wavelength is shown in Fig. 8.3. The top row shows two density distributions of stripes, one perturbed (left) and one unperturbed (right). Because the stripe phase shifts are small, it is difficult to see in the density distribution, but the perturbations become clearer in the average density contrast, plotted in the second row. The solid lines show the perturbed (red) and unperturbed (black) density contrasts, while the dashed lines show the extracted maxima and minima. Three periods later, the deformations have inverted (third row). The differences in position relative to the wavelength of the lattice are plotted in gray and purple in the fourth panel, and here the inversion of the initial modulation is clear. Error bars are given by the 1σ fit uncertainty when extracting lattice positions.

In order to quantify the time dynamics, we define a time-time correlator

$$\eta_l(t) = \sum_i \delta\theta_l(x_i, t)\delta\theta_l(x_i, t_0), \tag{8.6}$$

where i is the lattice site, and t_0 is the deformation vector immediately after the imprint. This correlator is plotted in the lowest panel of Fig. 8.3, and is fitted with a damped sine. This process can be repeated for many perturbation wavelengths to extract the dispersion relation.

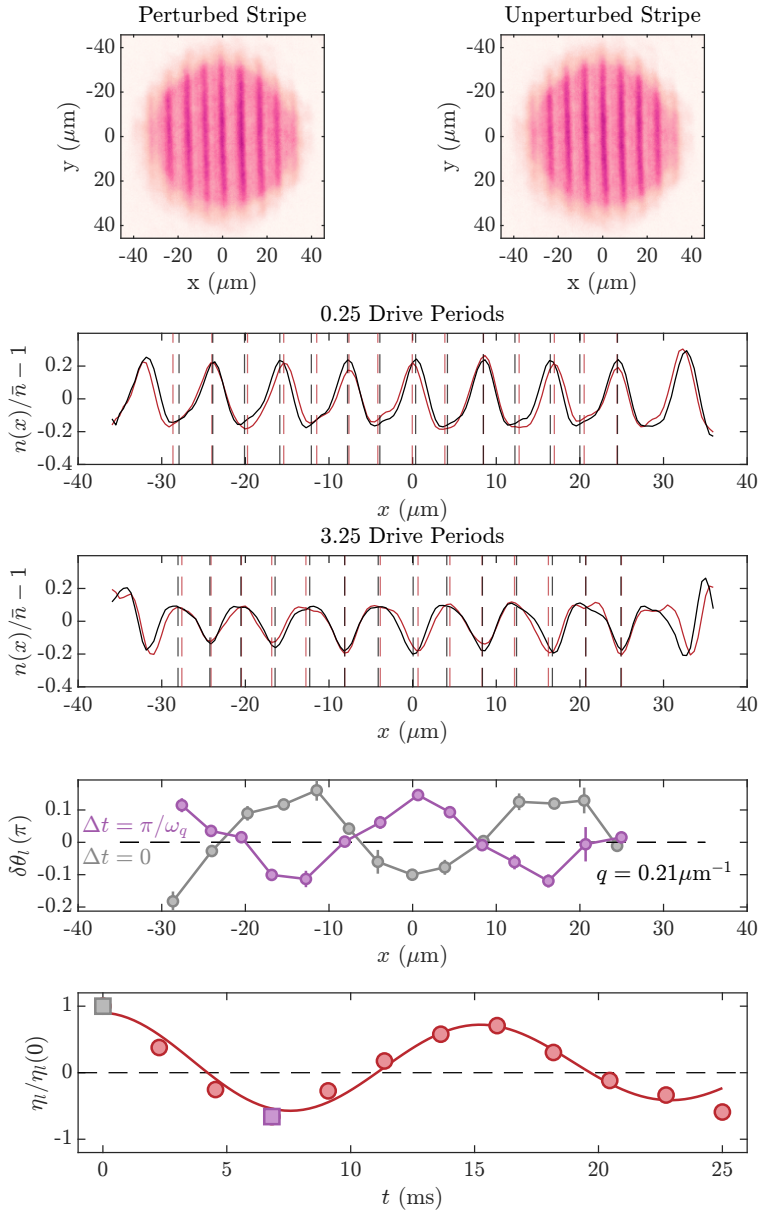

Figure 8.3: Extraction of Lattice Response. The top row shows the mean density distribution of a perturbed (left) and unperturbed (right) stripe. The perturbation is visible as a slight stretching and compression of the density wave. Second and third row, the extracted 1D density contrast, with lattice maxima and minima marked with dashed lines for perturbed (red) and unperturbed (black) lattices. Fourth row, the displacements between the perturbed and unperturbed peak positions, plotted as a function of space. Bottom row, the correlator η_l, showing the oscillatory response of the perturbation. In the lower two plots, error bars are either shown or are smaller than the markers.

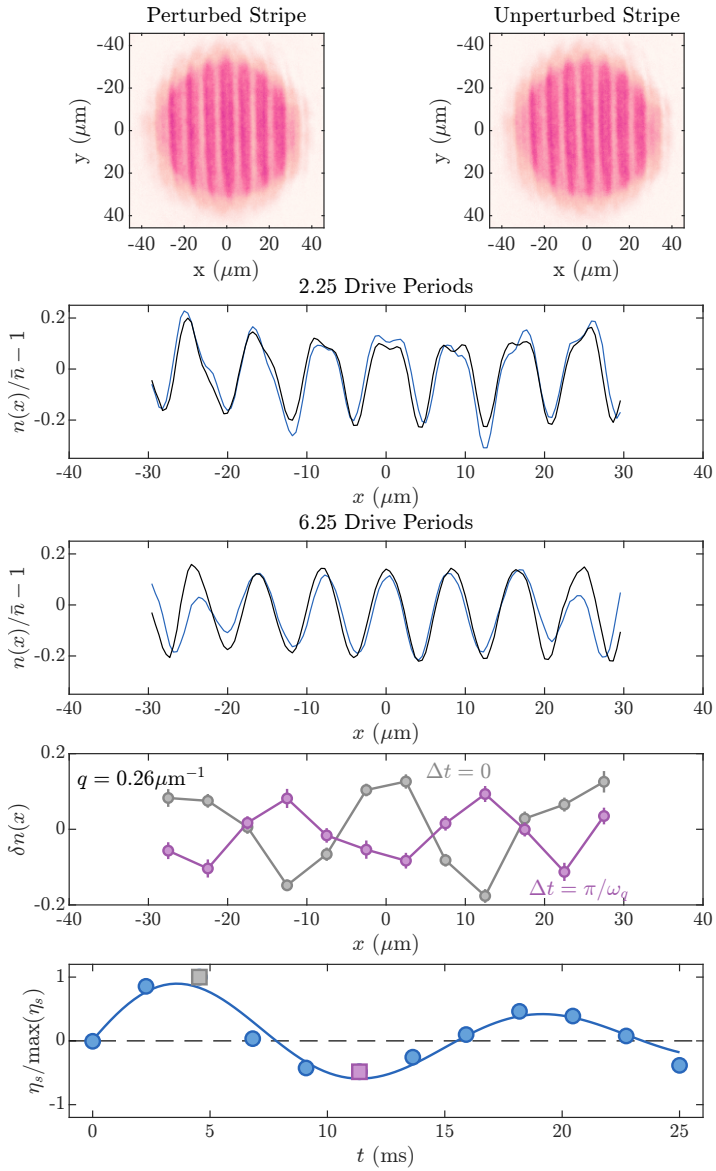

Figure 8.4: Extraction of Superfluid Response. The top row shows density distributions after a superfluid phase mode has been excited in the horizontal and vertical directions. The second and third rows show integrated density differences of the stripe for the horizontal phase mode. The over- and under-densities can be seen in the perturbed case (blue) relative to the unperturbed case (black). The fourth panel shows the binned difference between the perturbed and unperturbed cases at the reference time (gray) and inverted time (purple). The bottom panel shows the oscillatory response of the correlator, η_s. Error bars on the bottom two plots are either shown or smaller than the markers.

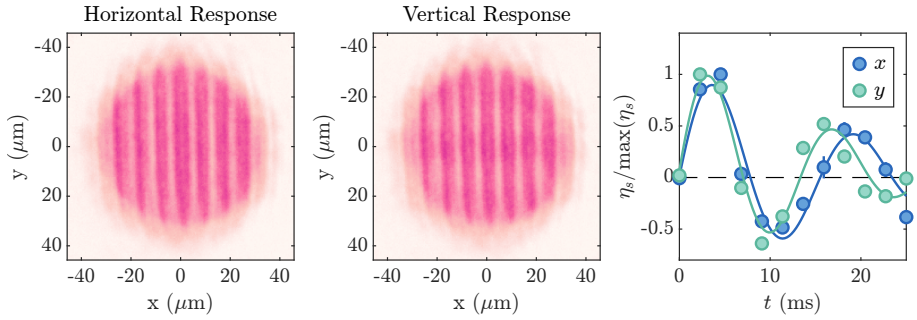

Figure 8.5: Anisotropic Superfluid Response. The left and central panel show maximally modulated density distributions after superfluid perturbations oriented horizontally and perpendicularly to the stripe. The right shows the correlator η_s over time for the two cases, showing a faster response in y than in x.

8.5 Probing Superfluid Phase Defects

Alternatively, deformations can be written into the superfluid phase, θ_s. Here, phase gradients lead to currents [58],

$$\vec{v} = \frac{\hbar}{m}\nabla\theta_s(x, y), \tag{8.7}$$

and thus slow phase gradients induce slow "sloshing" of the background density.

For superfluid phase modes, we do not immediately imprint the defects simultaneously with the lattice, but rather after half a period of driving using a second phase imprint. This ensures that the lattice is established before the background density is perturbed. These defects can be written in the longitudinal and transverse directions, probing the superfluid response perpendicular and parallel to the lattice.

The extraction of the dynamics is detailed in Fig. 8.4. The top row shows the first maximally modulated density distribution after a superfluid phase perturbation (left), as well as the unperturbed stripe at the same time (right). The perturbation is visible as slow variations of the density in the x direction (most noticeable around $\pm 10\,\mu$m). The second and third rows show the perturbed (red) and unperturbed (black) density contrasts at the first maximally modulated time (i.e. the reference time) and the inversion time. The deformation vectors, shown in the fourth row in gray and purple, are calculated by subtracting the perturbed and unperturbed densities and then binning the difference in 5 μm intervals. Error bars are generated using a jack-knife algorithm, which takes shot-to-shot fluctuations of the density into account. We again calculate the time-time correlator of these deformations,

$$\eta_s(t) = \sum_i \delta n_i(t)\delta n_i(t_0), \tag{8.8}$$

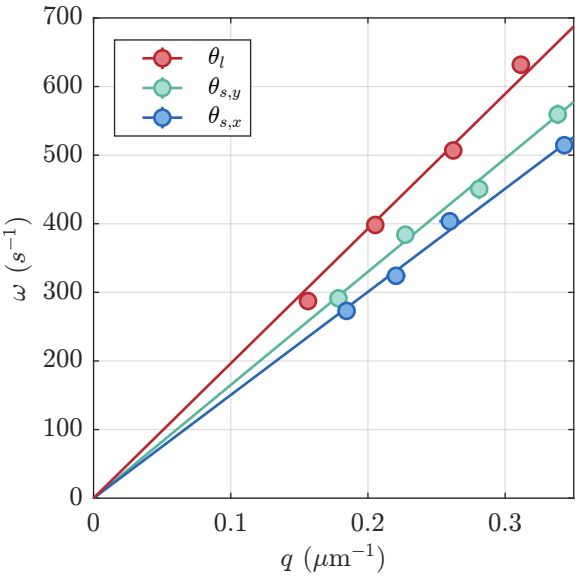

Figure 8.6: Measured Dispersion for Propagating Modes. The extracted wavenumbers and frequencies for collective modes instigated in the stripe. The red dots show stripe phase perturbations, the blue dots the horizontal superfluid phase, and teal dots the vertical superfluid response. The solid lines are fits, with slopes $c_+ = 1.96(4)\mu$m/ms, $c_- = 1.50(2)\mu$m/ms, and $c_\perp = 1.65(2)\mu$m/ms.

where t_0 is selected by finding the first time where the density is maximally modulated. The correlator is shown in the lowest panel of Fig. 8.4.

This process is repeated for excitations in the vertical direction, to extract the difference in superfluid response parallel and perpendicular to the lattice. As shown in Fig. 8.5, we instigate identical excitations in x and y, and calculate the correlators $\eta_{s,x}$ and $\eta_{s,y}$. For the mode shown in the plot ($q = 0.26\mu\text{m}^{-1}$), the oscillation in time is notably faster in y than in x, indicating an anisotropic superfluid response.

8.6 Measuring Dispersion Relation

Repeating the procedure described above for superfluid and lattice deformations for a number of wavelengths, we can experimentally determine the slopes of the dispersion relation for the different modes. To extract the wavenumber q we fit a sine to the reference deformation (either $\delta n(t_0)$ or $\delta\theta_l(t_0)$ to extract its wavelength. Using the frequency extracted from the sine fits to the correlators $\eta(t)$, we can extract a dispersion relation. The results are shown in Fig. 8.6. The red and blue points show the extracted frequencies of the longitudinal modes, while the teal points show

the transverse superfluid response. In order to extract the speeds of sound from the data, we perform a simple linear fit of the form $\omega = c_i q$. The extracted slopes are $c_+ = 1.96(4)\mu$m/ms, $c_- = 1.50(2)\mu$m/ms, and $c_\perp = 1.65(2)\mu$m/ms. While the lattice mode is faster (i.e. has a larger slope) than the transverse superfluid mode, the longitudinal superfluid response is diminished. This is remarkable, as the probed excitations and readout are identical, and the only difference is the orientation relative to the stripe. The difference in speeds between the lattice and superfluid modes indicates that these degrees of freedom are distinguishable, and that the presence of the lattice gives rise to new excitation modes.

These speeds can be used to extract the hydrodynamic variables, which can be found by rewriting Eq. (8.3) to find

$$\begin{aligned} \frac{B}{\rho_n} &= c_+^2 + c_-^2 - c_\perp^2 \\ f_s &= \frac{c_+^2 c_-^2}{c_\perp^2 (c_+^2 + c_-^2 - c_\perp^2)}. \end{aligned} \tag{8.9}$$

In this experiment, the parameters are: $\frac{B}{\rho_n} = 3.4(2)\mu\text{m}^2/\text{ms}^2$, and $f_s = 0.94(1)$. Errors are estimated using Monte Carlo error propagation. Here, the benefit of the stripe pattern over the square lattice is apparent: only because we are able to experimentally determine $c_\perp$ can we extract the hydrodynamic parameters.

8.7 Dependence on Stripe Contrast

We can repeat the experiment shown above for different stripe contrasts. By changing the drive amplitude, we can stabilize stripes of different contrasts, slightly adjusting the drive frequency in each case to ensure that drifts in wavenumber are minimized. We use drive amplitudes $r = 0.22, 0.3, 0.4$, and the stripes have a resulting average maximal contrast of $\frac{\max(n)-\min(n)}{\max(n)+\min(n)} = 0.23, 0.25, 0.31$. Frequencies used are $\omega_d/2\pi =$ 425, 440, and 450 Hz.

The extracted hydrodynamic parameters for the three contrasts are shown in Fig. 8.7. The extracted superfluid fraction is roughly constant over the three contrasts. The data points are compared to the Legget superfluid fraction of a density modulated with a sine wave (dashed line)[3] [27]

$$f_{s,x} \leq \frac{1}{\langle \rho(x) \rangle \langle \frac{1}{\rho(x)} \rangle}. \tag{8.10}$$

[3] If the density distribution is separable in spatial coordinates (i.e. $\psi(x, y) = \Psi(x)\Phi(y)$), this limit becomes an equality. In the trapping configuration we consider here, this is true to a good approximation.

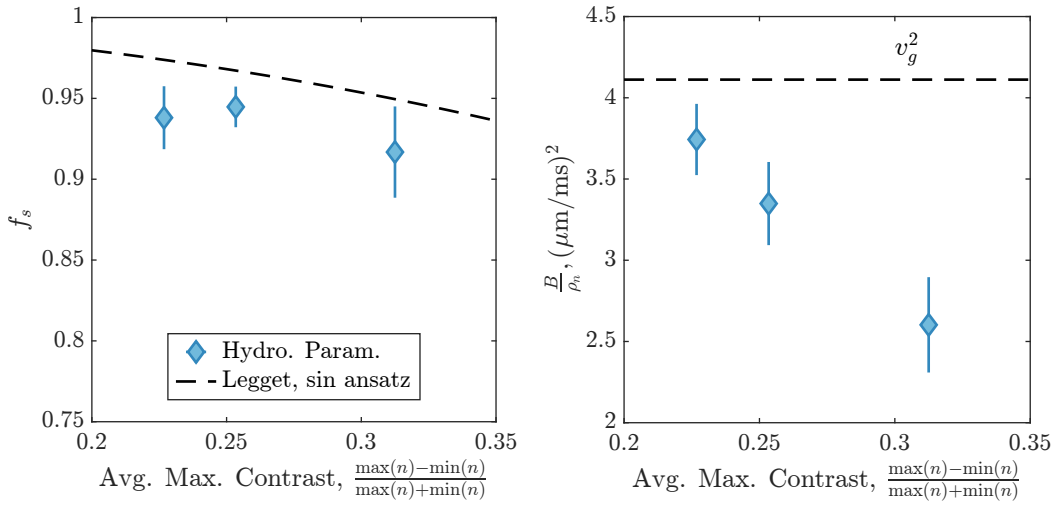

Figure 8.7: Dependence on Stripe Contrast. Extracted hydrodynamic parameters using measured dispersions for three stripe contrasts. While the extracted superfluid fraction remains constant within error bars (left), the lattice compression modulus decreases (right). In the left plot, the dashed line is the Leggett prediction for the superfluid fraction for a sine wave *ansatz*. On the right, the dashed line shows the squared group velocity at k_c, which is the natural response of a homogeneous superfluid perturbed at a given wavelength.

The deviations between the value extracted using the hydrodynamic framework and this prediction are remarkably small; indeed, one would not *a priori* expect the prediction to be applicable in the time-dependent, far-from-equilibrium state.

The lattice rigidity, however, decreases significantly between the three cases. This corresponds to both a slower lattice and longitudinal superfluid mode, as the larger contrast results in a less rigid system. The horizontal dashed line on the right shows the squared group velocity of the superfluid at k_c, using the speed of sound in the transverse direction, $c_\perp$, to parameterize the dispersion relation. This is given as a reference because it is the natural response of a superfluid perturbed at a given wavelength for a vanishing lattice contrast.

8.8 Transverse Sound

The experiments described so far have looked at one-dimensional dynamics of a stripe, using the transverse direction as a reference for extracting the bulk compressibility. As was described in the previous sections, however, the natural steady state of the experiment is characterized by square lattices, indicating the stabilization of

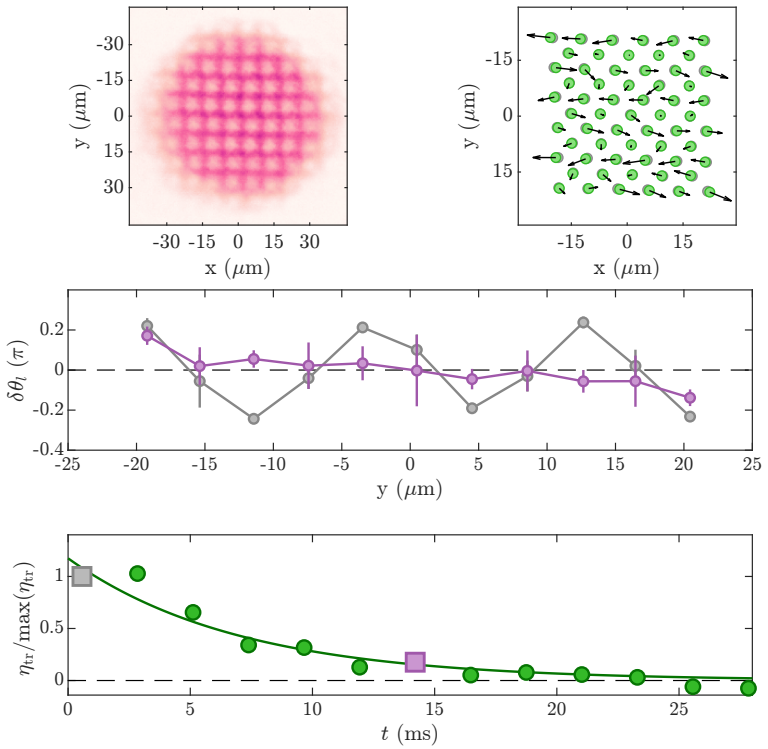

Figure 8.8: Extraction of Transverse Lattice Response. Top left, the initial density distribution of a lattice with a transverse phase perturbation. Top right, the extracted lattice maxima and minima of the perturbed lattice (green) and the unperturbed lattice (gray), with vectors indicating the displacement between the two. Center, the extracted phase deformation at the first time (gray) and 6 periods later (purple). Bottom, the correlator, fitted with an exponential decay.

two-dimensional structures. Indeed, the presence of transverse sound is the defining characteristic of a solid; deformations of the lattice perpendicular to the crystalline axis should yield a different response than the compression mode. In liquids, transverse excitations are defined via shear viscosity and are not propagating modes. Therefore, the observation of transverse sound would distinguish whether the pattern we observe is a solid, or rather two superimposed superfluid smectics.

In order to probe transverse sound, we prepare square lattices with the same procedure described previously. However, we now write defects into the vertical axis, i.e.

$$\delta\theta_{\mathrm{tr}} = 0.4\pi \cos qy. \tag{8.11}$$

An exemplary initial distribution is shown in the top left panel of Fig. 8.8, where

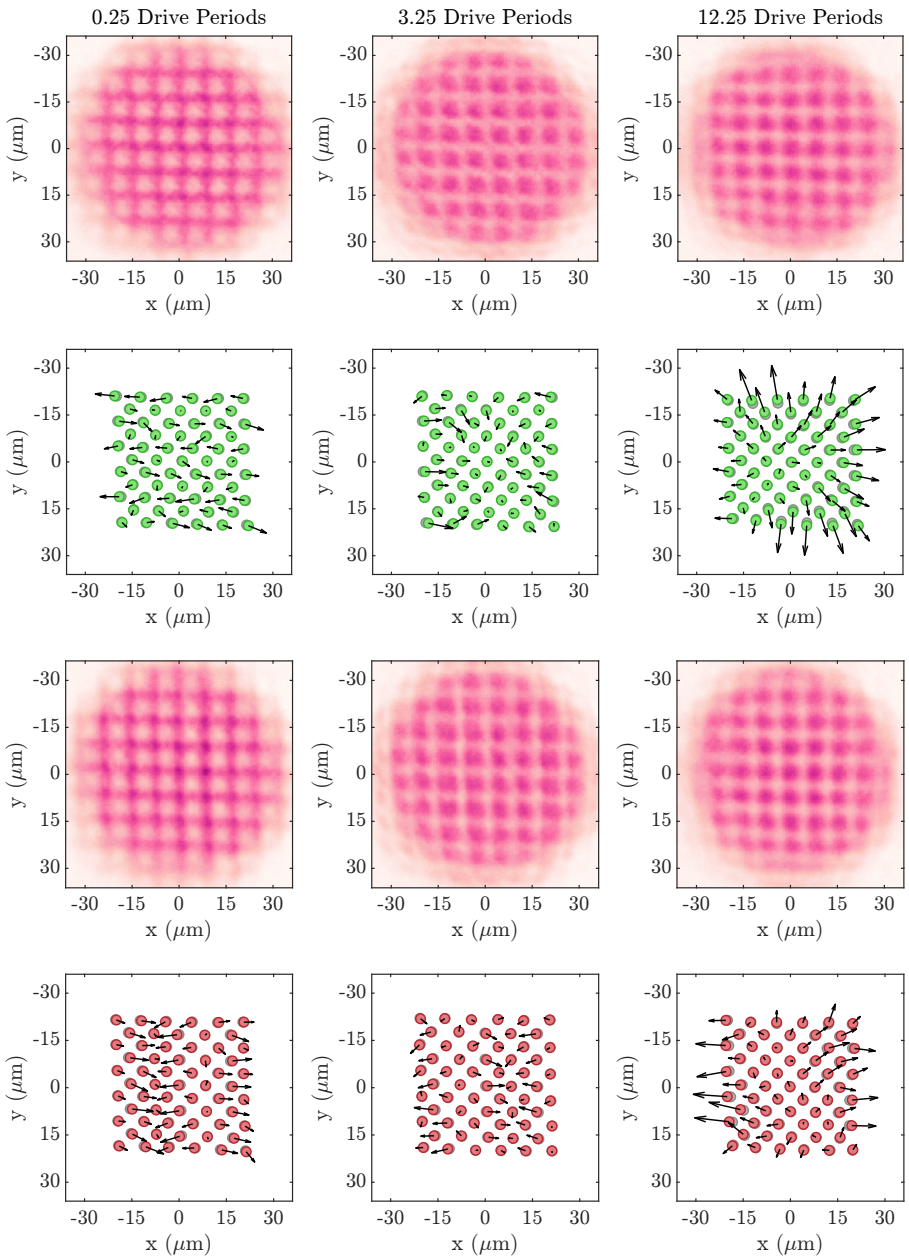

Figure 8.9: Extracted Lattice Positions. The top row shows densities at three times, with a transverse lattice deformation. The extracted lattice positions (green and gray points) are plotted in the second row, showing the decay of the initially structured mode into large-scale distortions. The third row shows density distributions for a compression mode of the square lattice, and the fourth row the extracted lattice positions. Here, displacements largely stay in the horizontal axis.

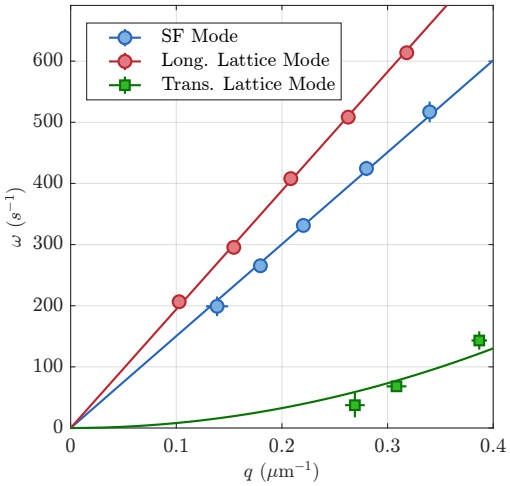

Figure 8.10: Collective Modes in Square Lattice. The three branches of the dispersion relation in the square lattice system. The superfluid and lattice modes (blue and red, respectively) are extracted as in the stripe pattern, with speeds $c_+ = 1.94(4)\mu$m/ms and $c_- = 1.50(2)\mu$m/ms. The transverse mode is fitted with a parabola, with coefficient $\omega_{\text{tr}} = -i\zeta k_n^2$, where $\zeta = 800(130)\,\frac{\mu\text{m}^2}{\text{s}} = 0.5(1)\,\frac{\hbar}{m}$.

the horizontal shift in the lattice phase is visible as a zig-zag perturbing the square lattice. The top right shows the extraction of individual lattice maxima and minima, determined using a Gaussian fit to the individual sites. The green points show the perturbed positions, and the gray points behind them are the reference lattice positions, with the black arrows marking the difference in position between the two. The central panel shows the extracted lattice deformation for the initial time in gray, where each point is an average deformation in x along a row. The purple curve shows these positions six periods later. Unlike in the previous cases, the initial deformation does not invert, and indeed when plotting η_{tr}, it is apparent that the dynamics are critically damped.

In order to visualize this damping, we plot the lattice positions after 0, 3, and 12 drive periods, shown in Fig. 8.9. We compare the differences between the transverse (top two rows) and longitudinal deformations (bottom two rows). In the transverse case, the highly structured initial state has almost entirely lost its ordering, and seems to result instead in large-scale lattice deformations, as is evident at 12 periods. In particular, deformations that were originally in the x direction have now coupled to the y axis. The longitudinal deformations, on the other hand, show remarkable stability throughout the cloud, not only in their sinusoidal mode structure but also in that deformations stay largely horizontal. This points to some fundamental difference between the transverse and longitudinal perturbations.

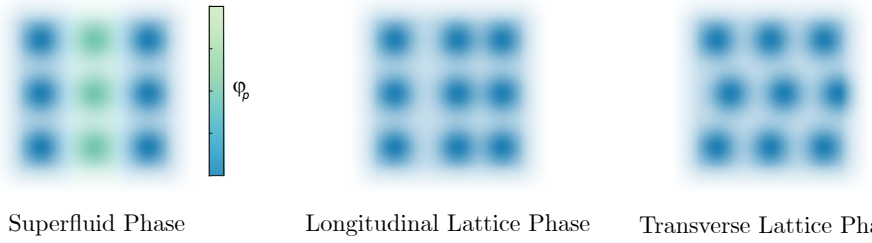

Figure 8.11: Types of Local Phase Defects. A schematic representation of the three wavepackets we will investigate. Left shows a superfluid phase kink, where a central region has an elevated phase relative to the bulk. Center, a lattice phase kink is shown, evident by the shifted column. Right, a transverse wavepacket, where the central row is shifted to the right.

8.9 Two-Dimensional Collective Modes

Finally, we can probe the dispersion relations of the three types of modes, i.e. longitudinal superfluid and lattice modes, as well as transverse lattice modes, by repeating the above procedure for various wavenumbers. The results, shown in Fig. 8.10, show that superfluid and longitudinal lattice modes are effectively identical to the stripe case, showing that the dynamics are unchanged by the presence of a second stripe. The extracted speeds of sound for the fast and slow modes are $c_+ = 1.94(4)\mu$m/ms, $c_- = 1.50(2)\mu$m/ms. The transverse mode shows critically damped behavior on all length scales, but this damping is length-scale dependent. Its frequency is therefore imaginary, and, due to the damped characteristic, is likely a diffusive mode, having the form $\omega_{tr} = -i\zeta k_n^2$, where ζ is a kinematic viscosity. The parabolic fit, shown as the solid green line in the figure, results in $\zeta = 0.80(13)\,\mu\text{m}^2/\text{ms} = 0.5(1)\,\hbar/m$.

8.10 Localized Phase Defects

The identification of two linear branches of the dispersion relation indicates that localized excitations in these modes should propagate through the system. Such wavepackets are localized in real space and therefore populate many momentum modes. Additionally, a wavepacket of the transverse sound mode can provide further insight if the excitation is truly diffusive.

Figure 8.11 shows the three types of wavepackets that we will consider in this work. The first is a superfluid phase kink, where a central region has an elevated phase relative to the rest of the superfluid. The rapid phase evolution will instigate two sets of over- and underdensities, which each propagate outwards. Alternatively,

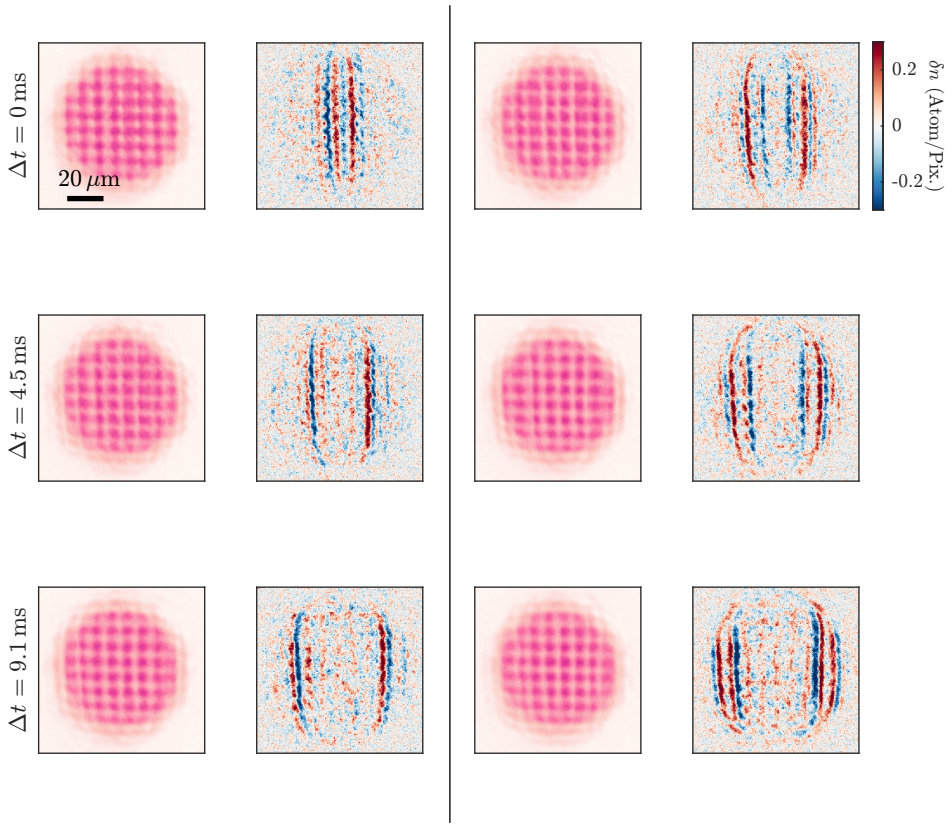

Figure 8.12: Propagating Wavepackets. The left half of the plot shows average densities and density differences for a propagating lattice wavepacket. The lattice is remarkably unperturbed after the wavepacket has passed through the system. The right half shows the superfluid wavepacket, where two over- and underdensities propagate outwards.

we can write in a lattice where either one column (or row) is shifted horizontally. These correspond to longitudinal and transverse lattice wavepackets, respectively.

8.11 Propagating Wavepackets

The lattice phase kink is easily prepared, in that we seed a lattice with a localized phase defect. This is done by locally shifting the lattice phase, with an approximate form $\delta\theta_l(|x| < 4\,\mu\text{m}) \sim 0.4\pi$. The dynamics for three times are shown on the left side of Fig. 8.12. In the density plots, lattice perturbations are slightly visible, which propagate outwards. This becomes more clearly visible in the density difference plots, which show a localized overdensity running to the right and an underdensity to the left. Notably, when the wavepacket has passed through the system, the lattice is

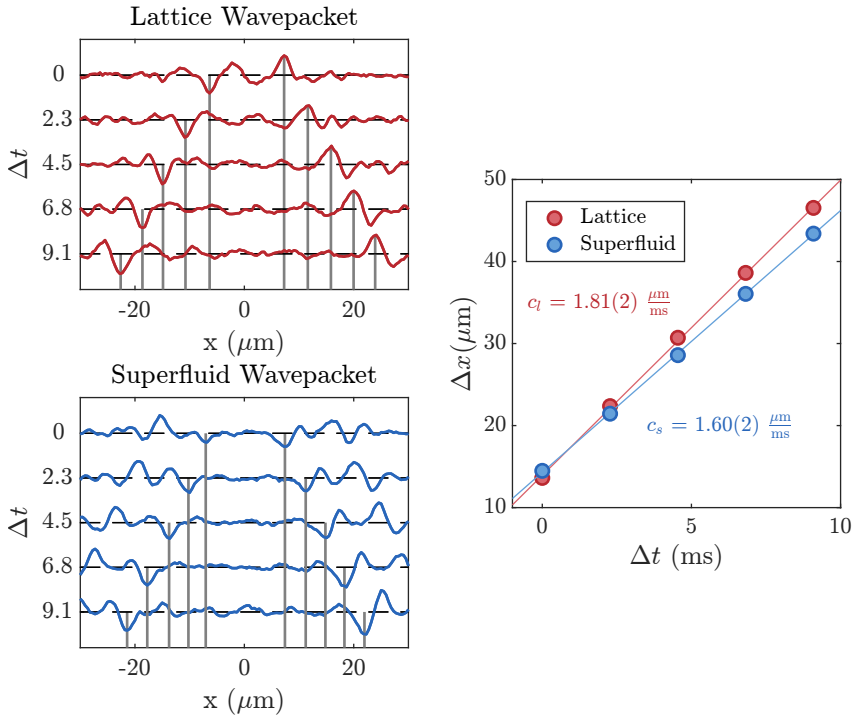

Figure 8.13: Extraction of Speed of Sound. Left, integrated density differences for the lattice and superfluid phase defects. Each curve is offset for clarity, with vertical lines plotted to show the extracted wavepacket positions. Right, the separation of the wavepacket with a linear fit. The extracted speed is half of the slope shown here.

restored to its bulk phase, visible through the homogeneity of the density difference at late times.

The superfluid wavepacket is prepared similarly to the superfluid phase modes discussed previously: First, the lattice is prepared using the calibrated phase imprint and hold time. Then the driving starts, and half a period later a stripe of light is flashed on for 100 μs in the central region of the condensate. This induces local density flow and therefore a localized wavepacket.

The right half of Fig. 8.12 shows the dynamics for the superfluid phase defect. The two phase kinks create over- and underdensities that propagate outwards, as is clearly visible in the density difference plots. In general, it seems that the imprints create large perturbations of both the lattice phase and the density, and we will therefore use the two underdensities to track the dynamics.

The two cases are considered at two different lab times, such that $\Delta t = 0$ corresponds to 2.8 ms in lab time for the lattice defect and 7.4 ms for the superfluid mode. The times are selected such that wavepackets are in the same physical position in the

cloud, in order to minimize effects of varying background density. The lab times are different due to the difference in preparation of the two wavepackets.

8.12 Extraction of Speeds

A careful, quantitative analysis of the perturbations shows that the two defects propagate with different speeds. In Fig. 8.13, integrated density differences at various times are plotted on the left. Each curve is shifted with a constant offset for clarity, and horizontal gray lines mark the determined wavepacket center, extracted using a parabolic fit. On the right, the wavepacket displacements are plotted together, with the lattice positions in red and the superfluid positions in blue. A linear fit is used to extract the speeds of sound of the two wavefronts, c_s and c_l, which are given by half of the slope fitted here. We find that $c_l = 1.81(2)\ \mu$m/ms, and $c_s = 1.60(2)\ \mu$m/ms.

Comparing these values to the slopes of the dispersion relation, $c_+ = 1.94(4)\ \mu\text{m/ms}$ and $c_- = 1.50(2)\ \mu\text{m/ms}$, we see the same tendency of a slow and fast branch, but no quantitative agreement. *A priori*, one does not typically expect that wavepackets propagate with the slope of the dispersion relation, because they are delocalized in momentum space. Furthermore, it is possible that the wavepackets seeded here are hybridizations of the two branches, because of imperfect instigation of the defects.

8.13 Diffusive Wavepacket

To seed transverse wavepackets, we shift the horizontal lattice phase as a function of the vertical coordinate, as shown in the left half of Fig. 8.14. The initially sharp dislocation in the lattice phase is smeared out after a time, but dynamics are very slow. Quantitatively, we extract the deformation by calculating the root-mean-squared average of the density difference signal in a central region $|x| < 8\ \mu$m. These profiles are plotted on the top right of Fig. 8.14 and show that the initially localized wavepacket spreads immediately, increasing in width.

In order to compare these dynamics to those extracted from the dispersion relation, we fit Gaussians to these profiles, and extract the width. A dispersion relation of the form $\omega = -i\zeta k^2$ will result in an initially Gaussian wavepacket $\psi = e^{-y^2/\sigma(t)^2}$ to broaden, such that

$$\sigma(t)^2 = 4\left(\sigma_0^2 + \zeta t\right). \tag{8.12}$$

The extracted squared widths are plotted in the bottom right of Fig. 8.14. After an initial sharp jump, the squared widths indeed increase linearly, with $\zeta_{\text{fit}} = 0.71(4)\mu\text{m}^2/\text{ms}$. The initial jump could be an artifact because the Gaussian fit does

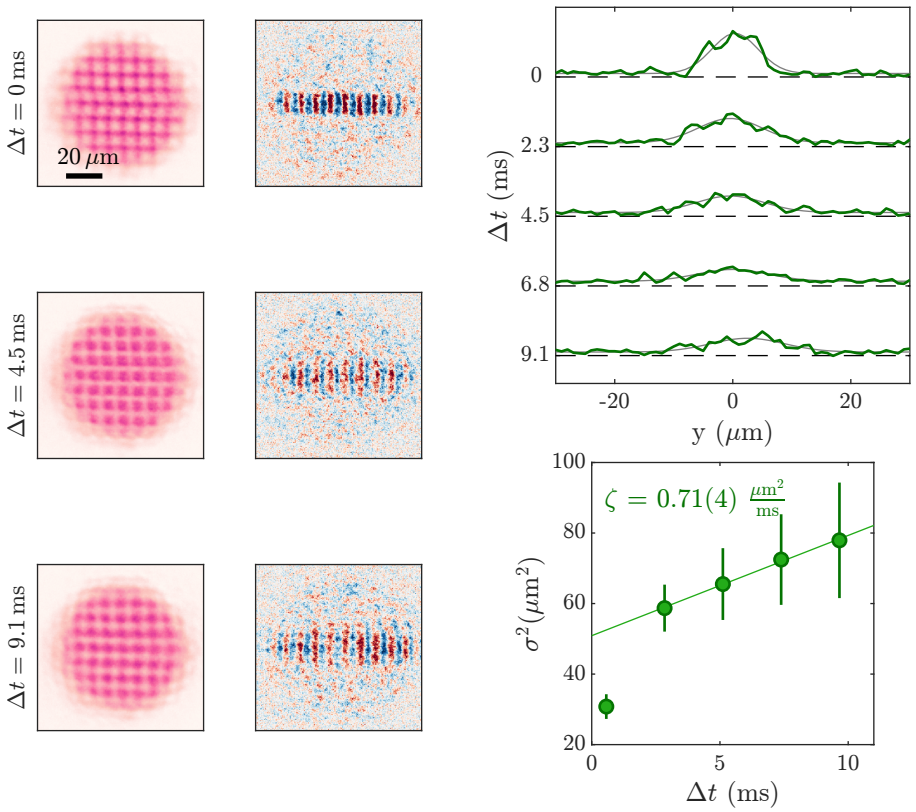

Figure 8.14: Transverse Wavepacket. Left, density and density difference plots for the transverse wavepacket. The dynamics are significantly slower than for the propagating modes, and the initially localized wavepacket spreads slowly. Right, the RMS density difference (black), with Gaussian fits (gray), which are used to extract the wavepacket width.

not accurately capture the width of the wavepacket, and the first point is therefore not used for the fit. The extracted slope consistent with the decays of the transverse collective modes, where $\zeta = 0.80(13)\frac{\mu m^2}{ms}$. At later times, the RMS signal of the transverse packet is on the same order as other fluctuations, and, as was shown in Fig. 8.9, the transverse excitation couples to many other degrees of freedom. We therefore confirm the behavior expected from the collective modes, showing that transverse wavepackets do not propagate but rather show diffusive behavior.

CHAPTER 9

Conclusion and Outlook

This thesis presents work on the emergence and excitations of two-dimensional patterns in a driven superfluid. We investigate how density waves grow, saturate, and arrange into square lattices. We then use tailored light fields to explicitly write these patterns into the superfluid, testing the theoretical model that describes phonon-phonon interactions. Finally, we probe the excitations of the driven steady-state, by writing defects into the phases of the superfluid and lattice. These modes are identical to those of a superfluid smectic (a supersolid in one dimension), and a hydrodynamic model can be used to extract relevant compressibilities of the system.

The results presented in this thesis introduce a new framework for understanding patterns in superfluids. By applying concepts of spontaneous symmetry breaking and supersolidity, we have established a link between equilibrium descriptions of periodically modulated superfluids to those in driven systems. This framework enables a multitude of further research avenues, as it reformulates standard pattern formation dynamics in terms of quantum phase transitions.

One direction of further research is a deepened study of the spontaneous emergence of patterns. So far, the description of the dynamics in this work has been classical. However, the production of quasiparticles from driving is in general a quantum process, and it will be interesting to investigate entanglement of particle pairs [20, 90, 100]. Additionally, particle production in the driven system is analogous to the production of particles in an oscillating spacetime, where the background density of the superfluid defines an effective metric [78, 101]. When occupations become large, however, perturbations cannot be separated from the background, and excitations instead turn into an emergent metric with an altered excitation spectrum. Finally, probing dynamics at the critical driving amplitude where the growth rate is equivalent to the damping $\alpha = \Gamma$ could be interesting to study driven-damped phase transitions [102].

The fixed-point description of the pattern also opens a number of avenues for

future work. For example, periodically driving the interactions while evaporatively cooling could show if it is possible to cool directly into the patterned state [103]. Additionally, multiple drive frequencies could be implemented to stabilize different pattern geometries, which could have higher-order symmetries and show new dynamics [18]. Finally, a detailed study of patch sizes, crystal boundaries, and the spread of correlations could be an interesting tool for describing dynamical crystallization in the driven superfluid.

In terms of supersolid sound modes, further investigation of the emergence of multiple branches of the dispersion relation could be performed by using Bragg scattering, to experimentally determine modes and their energies [104]. In far-from-equilibrium settings, new quasiparticles can arise that do not exist in equilibrium [105], and the connection of such excitations to the supersolid sound modes observed here could provide new insights.

The diffusive nature of the transverse mode observed in this work is also worth further investigation. For the square lattice, a first study will be into the influence of the R_+ mode on longitudinal and transverse modes. So far, the occupations in R_+ have been neglected when studying lattice excitations, but it is possible that transverse lattice deformations are particularly sensitive to occupations in higher modes, as evidenced by the data presented in Section 7.4. Additionally, it is possible that square lattices cannot support transverse sound because of redundant symmetry breaking [106]. If hexagonal structures can be stabilized with additional driving frequencies, however, it is possible that these geometries can have different sound modes from square lattices.

In the late-time dynamics of the pattern, heating and redistribution play a role not only in the quantitative description of pattern emergence, but could also have interesting parallels to cosmological phenomena like reheating [107]. The disintegration of Faraday patterns is a long-standing topic of research, and amplitude-dependent effects and phase defects could be studied to quantify pattern (in)stability [15, 57].

List of Publications

1. N Liebster, M Sparn, E Kath, J Duchene, H Strobel, MK Oberthaler. "Observation of supersolid-like sound modes in a driven quantum gas". arXiv:2503.10519, accepted in Nature Physics. (2025)

2. N Liebster, M Sparn, E Kath, J Duchene, K Fujii, SL Görlitz, T Enss, H Strobel, MK Oberthaler. "Observation of Pattern Stabilization in a Driven Superfluid". PRX **15**, 011026 (2025)

3. M Sparn, E Kath, N Liebster, J Duchene, K Fujii, SL Görlitz, T Enss, H Strobel, MK Oberthaler. "Experimental Particle Production in Time-Dependent Spacetimes: A One-Dimensional Scattering Problem". PRL **133**, 260201 (2024)

4. C Schmidt, Á. Parra-López, M Tolosa-Simeón, M Sparn, E Kath, N Liebster, J Duchene, H Strobel, MK Oberthaler, S Flörchinger. "Cosmological particle production in a quantum field simulator as a quantum mechanical scattering problem". PRD **110**, 123523 (2024)

5. K Fujii, SL Görlitz, N Liebster, M Sparn, E Kath, H Strobel, MK Oberthaler, T Enss. "Stable-fixed-point description of square-pattern formation in driven two-dimensional Bose-Einstein condensates". PRA **109**, L051301 (2024)

6. M Hans, E Kath, M Sparn, N Liebster, F Draxler, C Schnörr, H Strobel, MK Oberthaler, "Bose-Einstein condensate experiment as a nonlinear block of a machine learning pipeline". PRR **6**, 013122 (2024)

7. C Viermann, M Sparn, N Liebster, M Hans, E Kath, Á. Parra-López, M Tolosa-Simeón, N Sánchez-Kuntz, T Haas, H Strobel, S Flörchinger, MK Oberthaler. "Quantum Field Simulator for Dynamics in Curved Spacetime". Nature **611**, 260 (2022)

8. M Tolosa-Simeón, Á Parra-López, N Sánchez-Kuntz, T Haas, C Viermann, M Sparn, N Liebster, M Hans, E Kath, H Strobel, MK Oberthaler, S Flörchinger. "Curved and expanding spacetime geometries in Bose-Einstein condensates". PRA **106**, 033313 (2022)

9. M Hans, F Schmutte, C Viermann, N Liebster, M Sparn, MK Oberthaler, H Strobel. "High signal to noise absorption imaging of alkali atoms at moderate magnetic fields". Rev. Sci. Instrum. **92**, 023203 (2021)

Large parts of this thesis are based on the data presented in (1) and (2). In some cases, slightly different analyses of the data have resulted in quantitative differences to the values presented in the publications; all interpretations and qualitative results remain unchanged.

Bibliography

[1] A. M. Turing, "The chemical basis of morphogenesis", Philos. Trans. R. Soc. Lond. **237**, 37–72 (1952).

[2] M. C. Cross and P. C. Hohenberg, "Pattern formation outside of equilibrium", Rev. Mod. Phys. **65**, 851–1112 (1993).

[3] M. C. Cross and H. Greenside, *Pattern formation and dynamics in nonequilibrium systems* (Cambridge University Press, 2009).

[4] F. Arecchi, S. Boccaletti, and P. Ramazza, "Pattern formation and competition in nonlinear optics", Physics Reports **318**, 1–83 (1999).

[5] A. J. Koch and H. Meinhardt, "Biological pattern formation: from basic mechanisms to complex structures", Rev. Mod. Phys. **66**, 1481–1507 (1994).

[6] P. K. Maini, K. J. Painter, and H. Nguyen Phong Chau, "Spatial pattern formation in chemical and biological systems", J. Chem. Soc., Faraday Trans. **93**, 3601–3610 (1997).

[7] J. R. Abo-Shaeer, C. Raman, J. M. Vogels, and W. Ketterle, "Observation of vortex lattices in Bose-Einstein condensates", Science **292**, 476–479 (2001).

[8] I. Coddington, P. Engels, V. Schweikhard, and E. A. Cornell, "Observation of Tkachenko oscillations in rapidly rotating Bose-Einstein condensates", Phys. Rev. Lett. **91**, 100402 (2003).

[9] K. E. Strecker, G. B. Partridge, A. G. Truscott, and R. G. Hulet, "Formation and propagation of matter-wave soliton trains", Nature **417**, 150–153 (2002).

[10] P. Engels, C. Atherton, and M. A. Hoefer, "Observation of Faraday waves in a Bose-Einstein condensate", Phys. Rev. Lett. **98**, 095301 (2007).

[11] M. Faraday, "On a peculiar class of acoustical figures; and on certain forms assumed by groups of particles upon vibrating elastic surfaces", Phil. Trans. R. Soc. Lond. **3**, 49–51 (1837).

[12] S. T. Milner, "Square patterns and secondary instabilities in driven capillary waves", Journal of Fluid Mechanics **225**, 81–100 (1991).

[13] W. Zhang and J. Viñals, "Pattern formation in weakly damped parametric surface waves", Journal of Fluid Mechanics **336**, 301–330 (1997).

[14] S. Ciliberto and J. P. Gollub, "Chaotic mode competition in parametrically forced surface waves", Journal of Fluid Mechanics **158**, 381–398 (1985).

[15] J. H. V. Nguyen, M. C. Tsatsos, D. Luo, A. U. J. Lode, G. D. Telles, V. S. Bagnato, and R. G. Hulet, "Parametric excitation of a Bose-Einstein condensate: from Faraday waves to granulation", Phys. Rev. X **9**, 011052 (2019).

[16] J. Smits, L. Liao, H. T. C. Stoof, and P. van der Straten, "Observation of a space-time crystal in a superfluid quantum gas", Phys. Rev. Lett. **121**, 185301 (2018).

[17] J Smits, H. T. C. Stoof, and P van der Straten, "On the long-term stability of space-time crystals", New Journal of Physics **22**, 105001 (2020).

[18] Z. Zhang, K. X. Yao, L. Feng, J. Hu, and C. Chin, "Pattern formation in a driven Bose–Einstein condensate", Nature Physics **16**, 652–656 (2020).

[19] P. J. Everitt, M. A. Sooriyabandara, M. Guasoni, P. B. Wigley, C. H. Wei, G. D. McDonald, K. S. Hardman, P. Manju, J. D. Close, C. C. N. Kuhn, S. S. Szigeti, Y. S. Kivshar, and N. P. Robins, "Observation of a modulational instability in Bose-Einstein condensates", Phys. Rev. A **96**, 041601 (2017).

[20] C.-A. Chen, S. Khlebnikov, and C.-L. Hung, "Observation of quasiparticle pair production and quantum entanglement in atomic quantum gases quenched to an attractive interaction", Phys. Rev. Lett. **127**, 060404 (2021).

[21] D. Hernández-Rajkov, J. E. Padilla-Castillo, A. d. Río-Lima, A. Gutiérrez-Valdés, F. J. Poveda-Cuevas, and J. A. Seman, "Faraday waves in strongly interacting superfluids", New Journal of Physics **23**, 103038 (2021).

[22] N. Dupont, L. Gabardos, F. Arrouas, G. Chatelain, M. Arnal, J. Billy, P. Schlagheck, B. Peaudecerf, and D. Guéry-Odelin, "Emergence of tunable periodic density correlations in a Floquet–Bloch system", Proceedings of the National Academy of Sciences **120**, e2300980120 (2023).

[23] L. Chomaz, I. Ferrier-Barbut, F. Ferlaino, B. Laburthe-Tolra, B. L. Lev, and T. Pfau, "Dipolar physics: a review of experiments with magnetic quantum gases", Reports on Progress in Physics **86**, 026401 (2022).

[24] E. P. Gross, "Quantum theory of interacting bosons", Annals of Physics **9**, 292–324 (1960).

[25] A. F. Andreev and I. M. Lifshitz, "Quantum theory of defects in crystals", Soviet Physics JETP **29**, 1107–1113 (1969).

[26] G. V. Chester, "Speculations on Bose-Einstein condensation and quantum crystals", Phys. Rev. A **2**, 256–258 (1970).

[27] A. J. Leggett, "Can a solid be "superfluid"?", Phys. Rev. Lett. **25**, 1543–1546 (1970).

[28] J. Léonard, A. Morales, P. Zupancic, T. Esslinger, and T. Donner, "Supersolid formation in a quantum gas breaking a continuous translational symmetry", Nature **543**, 87–90 (2017).

[29] J.-R. Li, J. Lee, W. Huang, S. Burchesky, B. Shteynas, F. Çağrı Top, A. O. Jamison, and W. Ketterle, "A stripe phase with supersolid properties in spin–orbit-coupled Bose–Einstein condensates", Nature **543**, 91–94 (2017).

[30] L. Chomaz, D. Petter, P. Ilzhöfer, G. Natale, A. Trautmann, C. Politi, G. Durastante, R. M. W. van Bijnen, A. Patscheider, M. Sohmen, M. J. Mark, and F. Ferlaino, "Long-lived and transient supersolid behaviors in dipolar quantum gases", Phys. Rev. X **9**, 021012 (2019).

[31] L. Tanzi, E. Lucioni, F. Famà, J. Catani, A. Fioretti, C. Gabbanini, R. N. Bisset, L. Santos, and G. Modugno, "Observation of a dipolar quantum gas with metastable supersolid properties", Phys. Rev. Lett. **122**, 130405 (2019).

[32] F. Böttcher, J.-N. Schmidt, M. Wenzel, J. Hertkorn, M. Guo, T. Langen, and T. Pfau, "Transient supersolid properties in an array of dipolar quantum droplets", Phys. Rev. X **9**, 011051 (2019).

[33] M. Guo, F. Böttcher, J. Hertkorn, J.-N. Schmidt, M. Wenzel, H. P. Büchler, T. Langen, and T. Pfau, "The low-energy Goldstone mode in a trapped dipolar supersolid", Nature **574**, 386–389 (2019).

[34] G. Natale, R. M. W. van Bijnen, A. Patscheider, D. Petter, M. J. Mark, L. Chomaz, and F. Ferlaino, "Excitation spectrum of a trapped dipolar supersolid and its experimental evidence", Phys. Rev. Lett. **123**, 050402 (2019).

[35] L Tanzi, S. M. Roccuzzo, E Lucioni, F Famà, A Fioretti, C Gabbanini, G Modugno, A Recati, and S Stringari, "Supersolid symmetry breaking from compressional oscillations in a dipolar quantum gas", Nature **574**, 382–385 (2019).

[36] P Ilzhöfer, M Sohmen, G Durastante, C Politi, A Trautmann, G Natale, G Morpurgo, T Giamarchi, L Chomaz, M. J. Mark, and F Ferlaino, "Phase coherence in out-of-equilibrium supersolid states of ultracold dipolar atoms", Nature Physics **17**, 356–361 (2021).

[37] J. Hertkorn, J.-N. Schmidt, M. Guo, F. Böttcher, K. S. H. Ng, S. D. Graham, P. Uerlings, T. Langen, M. Zwierlein, and T. Pfau, "Pattern formation in quantum ferrofluids: from supersolids to superglasses", Phys. Rev. Res. **3**, 033125 (2021).

[38] L. Tanzi, J. G. Maloberti, G. Biagioni, A. Fioretti, C. Gabbanini, and G. Modugno, "Evidence of superfluidity in a dipolar supersolid from nonclassical rotational inertia", Science **371**, 1162–1165 (2021).

[39] M. A. Norcia, E. Poli, C. Politi, L. Klaus, T. Bland, M. J. Mark, L. Santos, R. N. Bisset, and F. Ferlaino, "Can angular oscillations probe superfluidity in dipolar supersolids?", Phys. Rev. Lett. **129**, 040403 (2022).

[40] P. B. Blakie, L. Chomaz, D. Baillie, and F. Ferlaino, "Compressibility and speeds of sound across the superfluid-to-supersolid phase transition of an elongated dipolar gas", Phys. Rev. Res. **5**, 033161 (2023).

[41] A. Recati and S. Stringari, "Supersolidity in ultracold dipolar gases", Nature Reviews Physics **5**, 735–743 (2023).

[42] G Biagioni, N Antolini, B Donelli, L Pezzè, A Smerzi, M Fattori, A Fioretti, C Gabbanini, M Inguscio, L Tanzi, and G Modugno, "Measurement of the superfluid fraction of a supersolid by Josephson effect", Nature **629**, 773–777 (2024).

[43] E. Casotti, E. Poli, L. Klaus, A. Litvinov, C. Ulm, C. Politi, M. J. Mark, T. Bland, and F. Ferlaino, "Observation of vortices in a dipolar supersolid", Nature **635**, 327–331 (2024).

[44] C. S. Chisholm, S. Hirthe, V. B. Makhalov, R. Ramos, R. Vatré, J. Cabedo, A. Celi, and L. Tarruell, "Probing supersolidity through excitations in a spin-orbit-coupled Bose-Einstein condensate", (2024), arXiv:2412.13861 [cond-mat.quant-gas].

[45] E. Poli, D. Baillie, F. Ferlaino, and P. B. Blakie, "Excitations of a two-dimensional supersolid", Phys. Rev. A **110**, 053301 (2024).

[46] P. S. Yapa and T. Bland, "Supersonic shear waves in dipolar supersolids", (2024), arXiv:2410.16060 [cond-mat.quant-gas].

[47] K. Fujii, S. L. Görlitz, N. Liebster, M. Sparn, E. Kath, H. Strobel, M. K. Oberthaler, and T. Enss, "Stable-fixed-point description of square-pattern formation in driven two-dimensional Bose-Einstein condensates", Phys. Rev. A **109**, L051301 (2024).

[48] C.-D. Yoo and A. T. Dorsey, "Hydrodynamic theory of supersolids: variational principle, effective lagrangian, and density-density correlation function", Phys. Rev. B **81**, 134518 (2010).

[49] J. Hofmann and W. Zwerger, "Hydrodynamics of a superfluid smectic", Journal of Statistical Mechanics: Theory and Experiment **2021**, 033104 (2021).

[50] N. Liebster, M. Sparn, E. Kath, J. Duchene, K. Fujii, S. L. Görlitz, T. Enss, H. Strobel, and M. K. Oberthaler, "Observation of pattern stabilization in a driven superfluid", Phys. Rev. X **15**, 011026 (2025).

[51] N. Liebster, M. Sparn, E. Kath, J. Duchene, H. Strobel, and M. K. Oberthaler, "Observation of supersolid-like sound modes in a driven quantum gas", (2025), arXiv:2503.10519 [cond-mat.quant-gas].

[52] A. J. Beekman, L. Rademaker, and J. van Wezel, "An introduction to spontaneous symmetry breaking", SciPost Phys. Lect. Notes, 11 (2019).

[53] P. Hohenberg and A. Krekhov, "An introduction to the Ginzburg–Landau theory of phase transitions and nonequilibrium patterns", Physics Reports **572**, An introduction to the Ginzburg–Landau theory of phase transitions and nonequilibrium patterns, 1–42 (2015).

[54] S. Elitzur, "Impossibility of spontaneously breaking local symmetries", Phys. Rev. D **12**, 3978–3982 (1975).

[55] I. Low and A. V. Manohar, "Spontaneously broken spacetime symmetries and Goldstone's theorem", Phys. Rev. Lett. **88**, 101602 (2002).

[56] H. Watanabe and H. Murayama, "Unified description of Nambu-Goldstone bosons without Lorentz invariance", Phys. Rev. Lett. **108**, 251602 (2012).

[57] I. Shani, G. Cohen, and J. Fineberg, "Localized instability on the route to disorder in Faraday waves", Phys. Rev. Lett. **104**, 184507 (2010).

[58] C. J. Pethick and H. Smith, *Bose–Einstein condensation in dilute gases*, 2nd ed. (Cambridge University Press, 2008).

[59] L. P. Pitaevskii and S. Stringari, *Bose-Einstein condensation*, Oxford Science Publications 116 (Clarendon Press, Oxford, 2003), 382 pp.

[60] G. Burdman, *Lecture notes quantum field theory 2*, 2020.

[61] K. Staliunas, S. Longhi, and G. J. de Valcárcel, "Faraday patterns in Bose-Einstein condensates", Phys. Rev. Lett. **89**, 210406 (2002).

[62] G. J. de Valcarcel, "Faraday patterns in Bose-Einstein condensates. Amplitude equation for rolls in the parametrically driven, damped Gross-Pitaevskii equation", (2002), arXiv:cond-mat/0204406 [cond-mat.soft].

[63] N. McLachlan, *Theory and applications of Mathieu functions* (Clarendon Press, Oxford, 1951).

[64] C. Brimacombe, R. M. Corless, and M. Zamir, "Computation and applications of Mathieu functions: a historical perspective", (2021), arXiv:2008.01812 [math-ph].

[65] Wolfram Research, "MathieuCharacteristicExponent", Accessed: 20-January-2025 (1996).

[66] J. Kevorkian and J. D. Cole, "The method of multiple scales for ordinary differential equations", in *Multiple scale and singular perturbation methods* (Springer New York, New York, NY, 1996), pp. 267–409.

[67] A. Nayfeh, *Perturbation methods* (Wiley, 2008).

[68] J. K. Hunter, *Asymptotic analysis and singular perturbation theory*, (2004) eprint: https://www.math.ucdavis.edu/~hunter/notes/asy.pdf.

[69] M. Hans, "Physical computing on a versatile setup for ultra-cold potassium", PhD thesis (Universität Heidelberg, 2022).

[70] C. Viermann, "Cosmological particle production and curced spaces in an ultracold quantum gas", PhD thesis (Universität Heidelberg, 2022).

[71] M. Sparn, "A setup for creating arbitrary potentials in a two-dimensional ^{39}K BEC with a digital micromirror device", Master's thesis (University of Heidelberg, Germany, 2020).

[72] J. Duchêne, "Designed boundaries for phonon-based quantum simulations", Master's thesis (University of Heidelberg, Germany, 2024).

[73] J. c. v. Etrych, G. Martirosyan, A. Cao, J. A. P. Glidden, L. H. Dogra, J. M. Hutson, Z. Hadzibabic, and C. Eigen, "Pinpointing Feshbach resonances and testing Efimov universalities in ^{39}K", Phys. Rev. Res. **5**, 013174 (2023).

[74] R. Grimm, M. Weidemüller, and Y. B. Ovchinnikov, "Optical dipole traps for neutral atoms", in , Vol. 42, edited by B. Bederson and H. Walther, Advances In Atomic, Molecular, and Optical Physics (Academic Press, 2000), pp. 95–170.

[75] B. Lee, "Introduction to ±12 degree orthogonal digital micromirror devices (DMDs)", Texas Instruments (2008).

[76] A. L. Gaunt, T. F. Schmidutz, I. Gotlibovych, R. P. Smith, and Z. Hadzibabic, "Bose-Einstein condensation of atoms in a uniform potential", Phys. Rev. Lett. **110**, 200406 (2013).

[77] G. Gauthier, I. Lenton, N. M. Parry, M. Baker, M. J. Davis, H. Rubinsztein-Dunlop, and T. W. Neely, "Direct imaging of a digital-micromirror device for configurable microscopic optical potentials", Optica **3**, 1136–1143 (2016).

[78] C. Viermann, M. Sparn, N. Liebster, M. Hans, E. Kath, A. Parra-López, M. Tolosa-Simeón, N. Sánchez-Kuntz, T. Haas, H. Strobel, S. Floerchinger, and M. K. Oberthaler, "Quantum field simulator for dynamics in curved spacetime", Nature **611**, 260–264 (2022).

[79] S. Tung, G. Lamporesi, D. Lobser, L. Xia, and E. A. Cornell, "Observation of the presuperfluid regime in a two-dimensional Bose gas", Phys. Rev. Lett. **105**, 230408 (2010).

[80] P. A. Murthy, D. Kedar, T. Lompe, M. Neidig, M. G. Ries, A. N. Wenz, G. Zürn, and S. Jochim, "Matter-wave Fourier optics with a strongly interacting two-dimensional Fermi gas", Phys. Rev. A **90**, 043611 (2014).

[81] L. Asteria, H. P. Zahn, M. N. Kosch, K. Sengstock, and C. Weitenberg, "Quantum gas magnifier for sub-lattice-resolved imaging of 3D quantum systems", Nature **599**, 571–575 (2021).

[82] S. Brandstetter, C. Heintze, K. Subramanian, P. Hill, P. M. Preiss, M. Ga lka, and S. Jochim, "Magnifying the wave function of interacting fermionic atoms", (2024), arXiv:2409.18954 [cond-mat.quant-gas].

[83] G. Salomon, L. Fouché, P. Wang, A. Aspect, P. Bouyer, and T. Bourdel, "Gray-molasses cooling of 39K to a high phase-space density", Europhysics Letters **104**, 63002 (2014).

[84] M. Hans, F. Schmutte, C. Viermann, N. Liebster, M. Sparn, M. K. Oberthaler, and H. Strobel, "High signal to noise absorption imaging of alkali atoms at moderate magnetic fields", Review of Scientific Instruments **92**, 023203 (2021).

[85] G. Reinaudi, T. Lahaye, Z. Wang, and D. Guéry-Odelin, "Strong saturation absorption imaging of dense clouds of ultracold atoms", Opt. Lett. **32**, 3143–3145 (2007).

[86] N. Navon, R. P. Smith, and Z. Hadzibabic, "Quantum gases in optical boxes", Nature Physics **17**, 1334–1341 (2021).

[87] M. Tajik, M. Gluza, N. Sebe, P. Schüttelkopf, F. Cataldini, J. Sabino, F. Møller, S.-C. Ji, S. Erne, G. Guarnieri, S. Sotiriadis, J. Eisert, and J. Schmiedmayer, "Experimental observation of curved light-cones in a quantum field simulator", Proceedings of the National Academy of Sciences **120**, e2301287120 (2023).

[88] M. Sparn, "Magnetic fields for cooling and trapping of potassium atoms", Bachelor's thesis (University of Heidelberg, Germany, 2017).

[89] C.-L. Hung, X. Zhang, L.-C. Ha, S.-K. Tung, N. Gemelke, and C. Chin, "Extracting density–density correlations from in situ images of atomic quantum gases", New Journal of Physics **13**, 075019 (2011).

[90] M. Sparn, E. Kath, N. Liebster, J. Duchene, C. F. Schmidt, M. Tolosa-Simeón, A. Parra-López, S. Floerchinger, H. Strobel, and M. K. Oberthaler, "Experimental particle production in time-dependent spacetimes: a one-dimensional scattering problem", Phys. Rev. Lett. **133**, 260201 (2024).

[91] M. Kern, "Enhanced local control of two-dimensional ultracold atomic clouds", Masterarbeit (Universität Heidelberg, 2024).

[92] Y. Guo, R. M. Kroeze, B. P. Marsh, S. Gopalakrishnan, J. Keeling, and B. L. Lev, "An optical lattice with sound", Nature **599**, 211–215 (2021).

[93] J. Higbie and D. M. Stamper-Kurn, "Generating macroscopic-quantum-superposition states in momentum and internal-state space from Bose-Einstein condensates with repulsive interactions", Phys. Rev. A **69**, 053605 (2004).

[94] M. A. Norcia, C. Politi, L. Klaus, E. Poli, M. Sohmen, M. J. Mark, R. N. Bisset, L. Santos, and F. Ferlaino, "Two-dimensional supersolidity in a dipolar quantum gas", Nature **596**, 357–361 (2021).

[95] J. H. V. Nguyen, D. Luo, and R. G. Hulet, "Formation of matter-wave soliton trains by modulational instability", Science **356**, 422–426 (2017).

[96] P. C. Martin, O. Parodi, and P. S. Pershan, "Unified hydrodynamic theory for crystals, liquid crystals, and normal fluids", Phys. Rev. A **6**, 2401–2420 (1972).

[97] P. G. D. Gennes and J Prost, *The physics of liquid crystals* (Oxford University Press, 1993).

[98] G. Chauveau, C. Maury, F. Rabec, C. Heintze, G. Brochier, S. Nascimbene, J. Dalibard, J. Beugnon, S. M. Roccuzzo, and S. Stringari, "Superfluid fraction in an interacting spatially modulated Bose-Einstein condensate", Phys. Rev. Lett. **130**, 226003 (2023).

[99] J. Tao, M. Zhao, and I. B. Spielman, "Observation of anisotropic superfluid density in an artificial crystal", Phys. Rev. Lett. **131**, 163401 (2023).

[100] S. Robertson, F. Michel, and R. Parentani, "Assessing degrees of entanglement of phonon states in atomic Bose gases through the measurement of commuting observables", Phys. Rev. D **96**, 045012 (2017).

[101] M. Tolosa-Simeón, A. Parra-López, N. Sánchez-Kuntz, T. Haas, C. Viermann, M. Sparn, N. Liebster, M. Hans, E. Kath, H. Strobel, M. K. Oberthaler, and S. Floerchinger, "Curved and expanding spacetime geometries in Bose-Einstein condensates", Phys. Rev. A **106**, 033313 (2022).

[102] M. Fruchart, R. Hanai, P. B. Littlewood, and V. Vitelli, "Non-reciprocal phase transitions", Nature **592**, 363–369 (2021).

[103] J Sánchez-Baena, C Politi, F Maucher, F Ferlaino, and T Pohl, "Heating a dipolar quantum fluid into a solid", Nature Communications **14**, 1868 (2023).

[104] D. Petter, G. Natale, R. M. W. van Bijnen, A. Patscheider, M. J. Mark, L. Chomaz, and F. Ferlaino, "Probing the roton excitation spectrum of a stable dipolar Bose gas", Phys. Rev. Lett. **122**, 183401 (2019).

[105] T. Preis, M. P. Heller, and J. Berges, "Stable and unstable perturbations in universal scaling phenomena far from equilibrium", Phys. Rev. Lett. **130**, 031602 (2023).

[106] H. Watanabe and H. Murayama, "Redundancies in Nambu-Goldstone bosons", Phys. Rev. Lett. **110**, 181601 (2013).

[107] A. Chatrchyan, K. T. Geier, M. K. Oberthaler, J. Berges, and P. Hauke, "Analog cosmological reheating in an ultracold Bose gas", Phys. Rev. A **104**, 023302 (2021).

Acknowledgements

This thesis would not have been possible without the support of my friends and family. I am forever indebted to you for your patience and love, even when I felt like I did not deserve it. I am particularly grateful to:

Markus, for his support, endless energy, and brilliance. I cannot think of a better place to have done my PhD, and I will always be grateful to the knowledge and opportunities you have offered me. To Helmut, who has been an infinite source of wisdom, and is always there for you, no matter how many other fires he is putting out. To Celia, with whom I spent the COVID lockdown locked in the lab; I will always cherish the shared feeling of endless exploration when we first began performing measurements at the BECK–how clueless, excited, and bright eyed we were. To Maurus, who taught me so much when I first started, and whose genius for design and engineering never ceases to amaze me. To Elinor, whose humor, creativity, and energy brightens every room she enters, and who always knew how to make my day better, no matter my mood. To Marius, for his incredible attention to detail and ability to push me to think deeper about a problem I thought I had already understood. To Jelte, whose dedication and quick thinking has brought an excellent energy to the team. To Philipp, for his seemingly constant good mood, which made the process of writing this thesis much more enjoyable. To Christiane, Petra, Dagmar, and the rest of the administration at the Kirchhoff-Institut, who work tirelessly to make our research possible. To all other Matterwavers, who made being in the group an absolute pleasure, even when I feared for our lives when kayaking down the Ardèche.

To Keisuke, for his incredible theoretical calculations that turned a funny-looking experimental signal into a fully-fledged scientific result. To Tilman, for answering any question I had, and for always taking time out of his day to sit down and chat with me. To Nicolò, who believed in our supersolid from the start. To Lauriane, not only for reading my thesis, but also for providing early and helpful input on supersolid excitations. To Henry Luo, whose dedication when mentoring me as a bachelor

student was instrumental to my success as a PhD.

To my pub quiz friends, specifically Mira, Daniel, Josef, Elinor and Laurin, who made Thursday evenings at the Dubliner's the absolute highlight of the week. To Alice and Daniela, who taught me to be more thoughtful, caring, and better at cooking; I will always cherish the memories we made in the Jakobsgasse. To Dennis, who has pushed me to be more creative, outgoing, and quirky in a way no other person could. Kwa Leticia, aliyenifungulia fursa mpya kujenga daraja kati ya wazungu na waswahili. Nguvu yako haina mwisho, na ninajivunia sana kujua mtu mwema kama wewe, mungu akubariki. To all members of Tia Moyo e.V., whose dedication (and donations) have made such an unbelievable impact in peoples' lives.

To Meta and Melle, for accepting me into your beautiful family from the very beginning. To Augi, for his unwavering love and for showing me the value of family. To Franz, the best conversation partner I could wish for, and with whom I love sharing the experience of living in Germany. To my parents, for their support in all of my life's endeavors.

And most of all to Lisa, who has enriched my life in ways I cannot describe in words.